UNIVERSITÉ CATHOLIQUE DE LOUVAIN
École Polytechnique de Louvain
ICTEAM Institute
Louvain-la-Neuve, Belgium

Inhomogeneous plane-wave spectrum based Physical Optics for the simulation of urban radio propagation

Quentin GUEUNING

Thesis presented for the Ph.D. degree in Engineering Sciences

Examining Committee

Advisors:	Christophe CRAEYE, UCLouvain, Belgium
	Claude OESTGES, UCLouvain, Belgium
Jury:	Conor BRENNAN, Dublin City University, Ireland
	Ovidio Mario BUCCI, University of Naples, Italy
	Philippe DE DONCKER, ULB, Belgium
Secretary:	Isabelle HUYNEN, UCLouvain, Belgium
President:	Jean-Pierre RASKIN, UCLouvain, Belgium

February 6, 2019

Acknowledgements

I would like to express here my gratitude to those who helped me in the realization of this thesis.

First, I greatly appreciate the effort and time devoted to this thesis by the members of my doctoral examination committee, Prof. Conor Brennan, Prof. Ovidio Mario Bucci, Prof. De Doncker, Prof. Isabelle Huynen and Prof. Jean-Pierre Raskin. Their careful reviews and suggestions have substantially improved this manuscript.

It is also a pleasure to thank my colleagues and friends from the antenna and the propagation groups for our fruitful (non-)scientific discussions and collaborations : Jean Cavillot, Nicolas Goreux, Gauthier Hennaux, Husnain A. Kayani, Inès Adouani, Donia Oueslati, Denis Tihon, Sumit Karki, Modeste Boudehou, Simon Hubert, Bui Van Ha, Maxime Drouguet, Christopher Raucy, Rajkumar Jaiswar, Valentina Sozio, Thomas Pairon, Simon Demey, Charles Wiame, Julian Villegas and Evgenii Vinogradov. I am also grateful to Brigitte Dupont for the computer assistance and to Marie-Christine Vandingenen, Isabelle Dargent and Christel Derzelle for the administrative support. I am also thinking of Basile, Virginie and my friends everywhere.

I sincerely thank my co-supervisors, Prof. Claude Oestges and Prof. Christophe Craeye, for the guidance and encouragement. Their accurate, creative and enlightened scientific mind have shaped my interest in research. I also would like to thank them for their effort to find the financial supports that made this doctoral work possible.

Finally, I dedicate this achievement to my sisters, Ariane and Candice, and to my parents, Ann and Dimitri, for their endless love and support.

Abstract

Characterizing the radio propagation in urban environment has become essential to the design, assessment and installation of future wireless communication systems. Benefiting from the progress in the fields of computer graphics and computational electromagnetics, the deterministic simulations have gain significant interest in the last decade since they offer the advantage of providing accurate results, thereby replacing the need for costly and complicated measurement campaigns. Ray-tracing methods implementing the high-frequency theories of diffraction are commonly preferred owing to their intuitiveness and low computation time. However, their accuracy rapidly degrades when the geometrical complexity of the buildings increases and when all the field contributions are not properly taken into account.

As a bottom-up approach, we started from a more accurate method, the Physical Optics (PO), and tried to reduce its computational cost. The PO radiation integral is known to accurately capture the truncation effect due to the finite dimension of scatterers. However, at Ultra High Frequencies (UHF), the numerical integration of highly-oscillating currents is extremely time-consuming. To overcome this critical issue, we have developed a fast algorithm which combines the efficiency of a Fast Fourier Transform (FFT) and the simplicity of an inhomogeneous plane-wave representation of the scattered fields. This substantially accelerates the computation of the radiation integrals over quasi-planar building walls at UHF down to seconds. This is a step forward towards a more accurate prediction of radio channels at cm-waves in large and complex urban environments.

Contents

Acknowledgements iii

Abstract v

Table of contents vi

List of figures x

List of tables xvi

Notations and Acronyms xix

1 Introduction 1
- 1.1 The channel in modern wireless communication systems . . 1
- 1.2 Geometrical database 4
- 1.3 Computational electromagnetics 5
- 1.4 Contributions 8
- 1.5 Outline 9

2 Sampling rules for an IPW representation of scattered fields 13
- 2.1 Introduction 13
- 2.2 Spectral-domain formulation 16
  - 2.2.1 Plane-wave representation of free-space Green's functions 16
  - 2.2.2 Decomposition of vector fields 19
- 2.3 Numerical errors 23
  - 2.3.1 Intermediate- to far-field distances 24

2.3.2 Near-field distances 33
2.4 Conclusion 38
2.5 Appendices 39
2.5.1 Derivation of steepest descent paths (SDP) 39
2.5.2 Truncation error 40
2.5.3 Discretization error 41
2.5.4 Error of the dyadic Green's function 41
2.5.5 Round-off error 42
2.5.6 Optimal integration scheme 43
2.5.7 Optimal contour slope 44
2.5.8 Inversion of the truncation error in the near-field . . 44
2.5.9 Inversion of the discretization error in the near-field . 45

3 Spectral-domain Physical Optics 47
3.1 Introduction 47
3.2 Spectral-domain Physical Optics 48
3.2.1 Mathematical formulation for a PEC plate 48
3.2.2 Extension to imperfectly conducting structures 50
3.3 Uniform asymptotic evaluation 52
3.4 Numerical results 56
3.4.1 Example 1 : Varying the relative distance 57
3.4.2 Example 2 : Forward scattering 58
3.4.3 Example 3 : Asymptotic evaluation of PO fields . . . 60
3.5 Conclusion 62
3.6 Appendices 65
3.6.1 Fourier transform over a polygonal domain 65
3.6.2 Sign and sense of the step functions 66
3.6.3 Rotation matrix 67

4 On the error of PO for the scattering analysis of flat surfaces 71
4.1 Introduction 71
4.2 Overview of high-frequency theories 73
4.3 Analytical study of the PEC wedge 75
4.3.1 Statement of the problem 75
4.3.2 Exact expression of the induced current 76
4.3.3 Plane-wave spectrum of the scattered field 78

4.3.4 Plane-wave spectrum of the Physical Optics field . . 78
4.3.5 Plane-wave spectrum of the fringe-wave field 79
4.3.6 Uniform asymptotic evaluation 80
4.3.7 Example : fringe-wave vs. PO fields 84
4.4 Numerical study of the PEC plate 85
4.4.1 Example 1 : Near-field scan experiment 88
4.4.2 Example 2 : Diffraction as function of distance 89
4.5 Conclusion 91
4.6 Appendices 93
4.6.1 Analytical expression of induced current on a wedge 93
4.6.2 Plane-wave spectrum of the scattered field 94
4.6.3 Plane-wave spectrum of the Physical Optics field . . 95
4.6.4 Rotation of the shadow boundaries for an inhomogeneous incident plane wave 96
4.6.5 Uniform asymptotic expression of the PO magnetic field 97

5 Simulating urban radio propagation with SPO 99
5.1 Introduction 99
5.2 Physical Shadowing 101
5.3 Fast visibility method 103
5.3.1 Step 1 : Binary Space Partitioning 103
5.3.2 Step 2 : Determination of the lit polygons 104
5.3.3 Step 3 : Last interactions 108
5.3.4 Numerical results 110
5.4 Multiple scattering interactions 115
5.4.1 Discussions 118
5.5 Conclusion 119

6 NFFT-based computation of radiation integrals 121
6.1 Introduction 121
6.2 Statement of the scalar problem 124
6.3 NFFT-based acceleration 126
6.3.1 The nonequispaced fast Fourier transform 126
6.3.2 The unequally-spaced fast Laplace transform 128
6.4 Other FFT-based methods 132

6.4.1 The chirp z-transform 132
6.4.2 The contour-FFT algorithm 134
6.4.3 Discussions 138
6.5 Extension to the vectorial problem 139
6.5.1 Mathematical formulation 140
6.5.2 Arbitrarily oriented source and observation plates . . 142
6.5.3 Small-scale height variation 143
6.6 Numerical results 144
6.6.1 Example 1 : Parallel plates 145
6.6.2 Example 2 : Tilted plates 146
6.6.3 Example 3 : Random rough plates 147
6.6.4 Example 4 : Radio propagation in a canyon 149
6.7 Conclusion 151
6.8 Appendices 153
6.8.1 Implementation of the classical FFT algorithm 153
6.8.2 The inverse unequally-spaced fast Laplace transform 154
6.8.3 Locus of the rotated spectral variables 155

7 Conclusion **157**

List of Publications **163**

Bibliography **164**

List of Figures

1.1 Some exposure limits to radio-frequency fields at 1800 MHz in V/m adopted by some European countries in sensitive area [7]. 2
1.2 Block diagram of a wireless communication system. 3
1.3 Illustration of available geometry in Brussels from CIRB [12]. 5

2.1 Illustration of several contours in Cartesian coordinates (top) and in polar coordinates for $\phi \in [-\pi/2, \pi/2]$ (bottom). 20
2.2 Cut view of the problem geometry with a local system of coordinates 22
2.3 Upper bound (solid) and exact value (dotted) of the truncation error for $(a, z, k_{mr}) = \{(0.7, 20\lambda, 0.7k); (0.5, 50\lambda, 0.37k); (1, 100\lambda, 0.15k)\}$. 26
2.4 Model (solid) and exact value (dotted) of the discretization error for $(a, z, dk) = \{(0.7, 20\lambda, 0.063k); (0.5, 50\lambda, 0.055k); (1, 100\lambda, 0.023k)\}$. 28
2.5 Upper bound (solid) and exact value (dotted) of the round-off error for $(a, z) = \{(0.75, 50\lambda); (0.75, 100\lambda); (0.5, 150\lambda)\}$. . 29
2.6 Optimal and empirical contour slope a as function of $-C/\ln|\epsilon|$ 31
2.7 Required number of plane waves vs. the near-field parameter C for three relative errors. 31
2.8 Model (dots) and exact value (solid lines) of the truncation error for three different values of a, k_{mr} and z. Case 1: $(a, z, k_{mr}) = (0.05, 0.5, 2.5)$, Case 2 : $(a, z, k_{mr}) = (0.03, , 0.2, 5.5)$ and Case 3 = $(a, z, k_{mr}) = (0.01, 0.2, 3.5)$. . . . 35

2.9 First and second order term of (2.51) (dots) and exact value (solid line) of the truncation error for $k_{mr} = 6k$ and $z = 0$. . . 36
2.10 Model (2.53) (dashed), first replicas of (2.32) at $z = 0$ (solid) and exact discretization errors using a parabolic (dotted with circles) and a linear contour (dotted with cross) for $z = \lambda$, $\Delta k/k = 0.012$ and $a = 0.01$. 37
2.11 Model (2.53) (dashed), first replicas of (2.32) at $z = 0$ (solid) and exact discretization errors using a parabolic (dotted with squares) and an exponentially-decaying contour (dotted with cross) for $z = 0$, $\Delta k/k = 0.02$ and $a = 0.01$. 37

3.1 Geometrical quantities associated to a polygon. 48
3.2 Cut view of a dielectric slab of polygonal faces and of impedance η_1 surrounded by free-space. 50
3.3 Geometry of a sector and related geometrical quantities. . . 55
3.4 Scattering scenario 1: a vertical dipole (dot) illuminates a square plate (solid) of side $L = 10\lambda$. The observation domain lies on a second plate (dashed) separated by a distance d. 57
3.5 Maximum relative error $\epsilon_{\max}$ (solid), target relative error ϵ_{tar} (dashed) and ratio P/N of number of plane waves to number of spatial samples (dotted). 58
3.6 Computation times (in sec) of the spatial-domain (dashed) and the spectral-domain (solid) methods. 59
3.7 Scattering scenario 2: a vertical dipole (dotted) illuminates a square plate (solid) of side $L = 20\lambda$. The observation domain lies on a horizontal second plate (grid). 60
3.8 Magnitude of the total electrical field, in configuration of Fig. 3.7. 61
3.9 Relative error of the IPW decomposition of the total electrical field for $\epsilon_{tar} = 10^{-3}$, in configuration of Fig. 3.7. 61
3.10 Scattering scenario 3: a plane wave illuminates a square plate of side 10λ at normal incidence. The observation path are three semi-circles with elevation $\theta = \{\pi/2, \pi/4, \pi/8\}$. . 62

3.11 Comparison of of the magnitude (in V/m) of the corner-diffracted PO field (3.28) (dots) vs. the exact PO field (solid) on a observation path of radius $R = 10000\lambda$, of elevation angles $\theta = \pi/8$ (top) and $\theta = \pi/4$ (bottom) for a plate of width 10λ at normal incidence. 63

3.12 Comparison of of the magnitude (in V/m) of the corner-diffracted PO field (3.28) (dashed), the edge-diffracted field (3.27) (dashed-dotted), the GO field (3.26) (circles), their sum (dots) and the exact PO field (solid) on a observation paths of radius $R = 20\lambda$ of elevation angles $\theta = \pi/8$ (top), $\theta = \pi/4$ (center) and $\theta = \pi/2$ (bottom) for a plate of width 10λ at normal incidence. 64

3.13 Contour deformation used to evaluate the integral (3.36). . . 66

3.14 Illustration of the interferences between sectors defined by (3.37) and (3.38) to produce the GO and edge-diffracted fields of a concave pentagon. Dashed lines correspond to the diffracting part of the edges and grey domains correspond to the reflecting part of the surface. 69

4.1 Cut view of the wedge geometry with a reference cylindrical CS. 76

4.2 Magnitude of the z-component of the exact (solid) and physical optics (dashed) currents for $\Phi = 1.8\pi$, $\phi^i = \pi/2$, $\theta^i = 0$, $E^i_{0z} = 1$, $H^i_{0z} = 1$. 77

4.3 Illustration of the incident (ISB) and the reflection (RSB) shadow boundaries. 81

4.4 Magnitude (in V/m) of z-component of the PO total field (solid), GO fields (dotted) and PO diffracted field (dashed) under complex incidence $\phi^i = \pi/4 + j\,0.1$ and $\theta^i = \pi/2 + j\,0.2$. 84

4.5 Magnitude (in V/m) of total and diffracted fields for a wedge ($\Phi = 7\pi/4$) illuminated at normal incidence ($\phi^i = \pi/2$). 86

4.6 Magnitude (in V/m) of total and diffracted fields for a wedge ($\Phi = 7\pi/4$) illuminated at grazing incidence ($\phi^i = \pi/10$). 87
4.7 Near-field scan experiment above a plate of side 3.9λ with $R = 9\lambda$ and a point source at $(0, 3\lambda, 3\lambda)$. 89
4.8 Magnitude (in V/m) of the back-scattered electrical field in H-plane (top) and E-plane (bottom) for the scenario depicted in Fig. 4.7. 90
4.9 A plane-wave illuminating a plate of side 7λ at normal incidence. 91
4.10 Magnitude (in V/m) of the back-scattered electrical field as function of the distance R for the scenario depicted in Fig. 4.9. 92

5.1 Shadowing scenario : a point source illuminates *plate*1. The back-scattered field from *plate*1 is evaluated on *plate*3 after being partially occluded by *plate*2. 101
5.2 Magnitude of the magnetic field $\mathbf{H}^{s13}$ (top left), $\mathbf{H}^{s23}$ (top right) and $\mathbf{H}^{s}$ (bottom) for the scenario sketched in Fig. 5.1. . 102
5.3 Illustration of the lit surfaces (grey) seen by a view point (black dot) through a source polygon (black). 105
5.4 Two-dimensional illustration of the perspective projection of a PV polygon onto the image plane for a given source point. 107
5.5 Clipping operations used for the determination of the lit surfaces. The intersection polygon (grey), the clipped source polygons (grey+white) and the projected polygons (black+white) are shown at each iteration starting from top left and ending at bottom right. 109
5.6 Mesh (top) and associated BSP tree (bottom) of Koekelberg region in Brussels. 111
5.7 Mesh (top) and associated BSP tree (bottom) of Flagey place in Brussels. 112
5.8 First-order (top) and second-order (bottom) lit polygons for a given Tx position (black dot) in Koekelberg region in Brussels. 113

5.9 Receivers seen by LoS (top) and after a single reflection (bottom) for Koekelberg region in Brussels. 114
5.10 Two-dimensional illustration of the computation of multiple interactions with SPO. 115
5.11 Double scattering scenario with $\mathbf{r}^i = (-L, 2L, 0)$, $\mathbf{r}^1 = (0, 0, 0)$, $\mathbf{r}^2 = (4L, 4L, 0)$. The observation path is a semicircle of radius $R = 2L$ centred on $\mathbf{r}^2$. 117
5.12 Comparison of the magnitude of the scattered magnetic field $\mathbf{H}^s$ for the scenario depicted in Fig. 5.9 obtained with SPO (solid) and with a brute-force spatial-domain integration (circles). 117

6.1 Spectral (left) and spatial (right) grids. 125
6.2 Unidimensional illustration of three efficient convolutions between the spectral Green function $\tilde{G}$ (circle) and the window function $\tilde{\psi}$ (solid). 128
6.3 Real (left) and imaginary (right) parts of $\tilde{\psi}(k'_x - k_x, k'_y - k_y)$ with $k_x = k_y = 0.3kj$. 129
6.4 Green's function and relative error of USFLT for $z = 0.25\lambda$, $a = 0.03$, $L = 40\lambda$, $\epsilon_{tar} = 10^{-2}$, $M = 4$ and a parabolic contour. 131
6.5 Illustration of a straight path (dashed) for the estimation of the Taylor series error when evaluating the two-dimensional Green's function. 136
6.6 Model (solid) and exact value (dotted) of the CFFT error for $z = \lambda$, $(a, T) = \{(0.01, 4), (0.01, 6), (1, 10)\}$. 137
6.7 Green's function and relative error of CFFT for $z = 0.25\lambda$, $a = 0.03$, $L = 40\lambda$, $\epsilon_{tar} = 10^{-2}$, $T = 7$ and a parabolic contour. 137
6.8 Optimal values of $(2M + 1)^2 P$ (solid) and of $4c_1 N \log_2 N$ (dashed) for $\epsilon = 10^{-2}$, $k_{mr} = 2k$ and $z = 0.5\lambda$. 140
6.9 Geometry and local CS used for the computation of fields scattered from a source plate over a virtual observation plate when illuminated by a point source. 141
6.10 Illustration of the rotation of IPW samples due to the change of CS from $(\hat{\mathbf{x}}, \hat{\mathbf{y}}, \hat{\mathbf{z}})$ to $(\hat{\mathbf{x}}^o, \hat{\mathbf{y}}^o, \hat{\mathbf{z}}^o)$. 143

6.11 Magnitude of the scattered field (left) and relative error (right) using CZT for $\mathbf{r}_i = 5\lambda\hat{\mathbf{z}}^s$, $d = 10\lambda$, $L = 10$, $nk = 52$, $N = 40$ and $a = 0.2$ (top) and for $\mathbf{r}_i = \lambda\hat{\mathbf{z}}^s$, $d = 2\lambda$, $L = 10$, $nk = 56$, $N = 40$ and $a = 0.1$ (bottom). 146
6.12 Scattering scenario: fields are computed from a source plate (solid) over perpendicular observation plates (dashed). . . . 147
6.13 Magnitude of the scattered field (left) and relative error (right) using USFLT for the observation plate 1 (top) and 2 (bottom). 148
6.14 Computation times of the convolutions (dashed) and of the FFT's (dashed) required by the USFLT-based method and of the brute-force spatial domain integration (solid-dot) for the scenario in Fig. 6.12. 148
6.15 Height profiles $z^s = h^s(x^s, y^s)$ and $z^o = h^o(x^o, y^o)$ of the source (left) and the observation (left) rough surfaces. 150
6.16 Magnitude of scattered field (top) and relative error (bottom) considering the scenario and the rough surfaces sketched in Fig.6.15 and in Fig. 6.15, respectively. 150
6.17 Double-scattering scenario in a narrow street for plates of size $L = 40\lambda$. 151
6.18 Magnitude of the electric field for the scenario shown in Fig. 6.17 when computed with the USFLT-based method (solid) and with the brute-force integration (dots) for flat (top) or rough (bottom) surfaces. 152

List of Tables

2.1 Number of plane-wave P for three error levels $|\epsilon|$ and distances z. 33

4.1 Summary of HF theories. 74

5.1 Computation times for each step of the fast visibility. 110

6.1 Number of operations of the fast methods. 138

Notations and Acronyms

Mathematical Notations

j	$\sqrt{-1}$
k	free-space wavenumber
λ	free-space wavelength
η	free-space impedance
G	Green's function
$\tilde{G}$	spectral Green's function
$\mathbf{k}$	wavevector
k_x, k_y, k_z	cartesian components of $\mathbf{k}$
k_ρ	radial component of $\mathbf{k}$
$\mathbf{k}_r$	real part of $\mathbf{k}$
$\mathbf{k}_i$	imaginary part of $\mathbf{k}$
k_{xr}	real part of k_x
k_{xi}	imaginary part of k_x
ϵ	relative error
ϵ_m	machine error level
$\mathbf{E}$	electric field
$\mathbf{H}$	magnetic field
$\mathbf{r}$	position of an observation point
x, y, z	cartesian components of $\mathbf{r}$
ρ	radial component of $\mathbf{r}$
ϕ	polar angle of $\mathbf{r}$
θ	elevation angle of $\mathbf{r}$
r	norm of $\mathbf{r}$

$\mathbf{r}'$	position of a source point
R	distance between $\mathbf{r}'$ and $\mathbf{r}$
$\tilde{\mathbf{E}}$	PWS of $\mathbf{E}$
$\tilde{\mathbf{H}}$	PWS of $\mathbf{H}$
$\mathbf{J}$	surface electric current
$\tilde{\mathbf{J}}$	Fourier transform of $\mathbf{J}$
w_p	spectral weight
Δk	spectral sampling step
P	number of plane waves
Δx	spatial sampling step
N	number of spatial samples
$k_{x,pq}$	sample of indices pq of k_x
$k_{xr,pq}$	real part of $k_{x,pq}$
C	near-field coefficient
F	Fresnel number
z_f	Fraunhoffer distance
k_m	truncation limit
a	contour slope
(p,q)	spectral indices
(m,n)	spatial indices
W	window function
U	step function
F	Fresnel's transition function
N_{op}	number of operations
$\mathbf{E}^s$	scattered electric field
$\mathbf{E}^i$	incident electric field
$\mathbf{E}^{go}$	GO electric field
$\mathbf{E}^{po}$	PO electric field
$\mathbf{E}^d$	diffracted field
$\mathbf{E}^{dpo}$	PO diffracted field
$\mathbf{H}^c$	corner-diffracted field
$\mathbf{H}^e$	edge-diffracted field
$\mathbf{p}$	polarization of a point source
$\mathbf{R}$	rotation matrix

$\mathbf{J}^{fw}$	fringe-wave current
$\mathbf{J}^{po}$	PO current
$\mathbf{E}^{fw}$	fringe-wave field
$(\hat{\mathbf{x}}, \hat{\mathbf{y}}, \hat{\mathbf{z}})$	CS basis vectors
$\mathbf{r}^{i}$	position of an excitation source
$\approx$	approximately equal to
$\gg$	is much greater than
$\ll$	is much lower than
$\lesssim$	is approximately lower than
$\sim$	is asymptotically equal to

Acronyms

AIM	Adaptive Integral Method
CS	Coordinate system
CFFT	Contour Fast Fourier Transform
CZT	Chirp Z-Transform
DFT	Discrete Fourier Transform
DoF	Degrees of Freedom
DTM	Digital Terrain Model
EFIE	Electrical Field Integral Equation
FDTD	Finite Difference Time Domain
FFT	Fast Fourier Transform
FIPWA	Fast Inhomogeneous Plane Wave Algorithm
FMM	Fast Multipole Method
GFI	Generalized Fresnel Integral
HIPWA	Harmonic-based Inhomogeneous Plane Wave Algorithm
ISB	Incident Shadow Boundary
IPO	Iterative Physical Optics
IPW	Inhomogeneous Plane Wave
LoS	Line-of-Sight
MIMO	Multiple Output Multiple Input
MLFMA	Multi-Level Fast Multipole Method
MoM	Method-of-Moments
NFFT	Nonequispaced Fast Fourier Transform

GO	Geometrical Optics
GTD	Geometrical Theory of Diffraction
PEC	Perfectly Electrical Conductor
p-FFT	Pre-corrected Fast Fourier Transform
PO	Physical Optics
PTD	Physical Theory of Diffraction
PWS	Plane-Wave Spectrum
RL	Ray-Launching
RSB	Reflection Shadow Boundary
RT	Ray-Tracing
SDP	Steepest Descent Path
SIP	Sommerfeld Integration Path
SPO	Spectral-domain Physical Optics
USFLT	Unequally-Spaced Fast Laplace Transform
UTD	Uniform Theory of Diffraction

Introduction

1

1.1 The channel in modern wireless communication systems

The growing demand for mobile internet access has driven the recent technological development of wireless communication systems. The information must be transmitted with ever higher bit-rates. CISCO company forecasts a consumption of 24 and 49 exabytes per month in 2019 and 2021, respectively. It is known [1] that mobile data traffic tends to double every two years. This exponential evolution, similar to Moore's law in electronics, reflects the reactivity with which innovations in the communication field are absorbed by the society.

Currently, cell phones are mostly operating in the Ultra-High Frequency (UHF) band (0.3-3 GHz). Multiple Input Multiple Output (MIMO) systems, relays and Heterogeneous Network (Het Net) have increased the spectral efficiency of the fourth generation (4G) of communication technologies [2]. Still, the inexhaustible need for bandwidth will lead to a shortage of available spectrum at cm waves. Hence, 5G communications will also use mm waves since most of this spectrum is unexploited and unlicensed. The 5G work at the World Radiocommunication Conference (WRC) in 2019 will look at spectrum in frequencies between 24.25 and 86 GHz [3]. In Europe, the European Conference of Postal and Telecommunications Administrations (CEPT) has already defined harmonisation measures in the 26 GHz band since it will provide over 3 GHz of contigu-

ous spectrum and more favourable propagation than the higher frequency bands [4]. Such communications are inherently short-ranges due to the increase of the propagation losses with frequency. The network will then become denser since the base stations will cover smaller cells ranging from a few to hundreds of meters. Particularly, the antennas placed closer to the ground level [5] will supply local near-field zones, such as offices, homes or public facilities. Other pragmatic factors such as energy saving and cost reduction will also tip the scales.

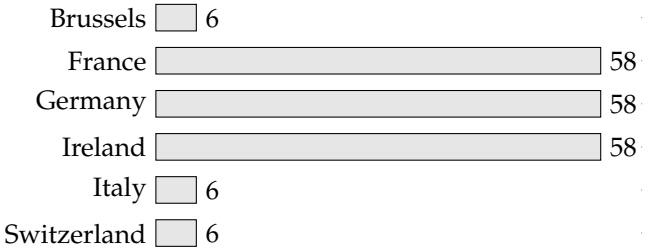

Figure 1.1: Some exposure limits to radio-frequency fields at 1800 MHz in V/m adopted by some European countries in sensitive area [7].

In parallel to that, the country authorities impose strict limits on the field levels radiated by cellular networks in precaution to unknown health effects of the exposure of human bodies to radio-frequency electromagnetic waves. Presently, the safety guidelines are prescribed by the International Commission on Non-Ionizing Radiation Protection (ICNIRP) and advocates, for instance, a maximum field level of 58 V/m at 1800 MHz. Since those standards are criticized by scientists, some countries have already adopted lower limits [7], as summarized in Fig. 1.1 for some European countries/cities, mainly in residential or more sensitive areas, such as schools, hospitals or playgrounds. In Brussels, the maximum field level is 6 V/m for the cumulative exposure from multiple antenna locations [8]. Instead of only increasing throughput, the coming technological challenges will thus also be to lower the average power intensity while guaranteeing a similar performance. A promising approach [9] consists of jointly shaping the antenna pattern of multiple base stations according to their surrounding environment in order to better homogenize their radio coverage while

respecting the constraints on the field level. In [10], this was implemented by placing a passive array of parasitic dipoles in front of existing antennas.

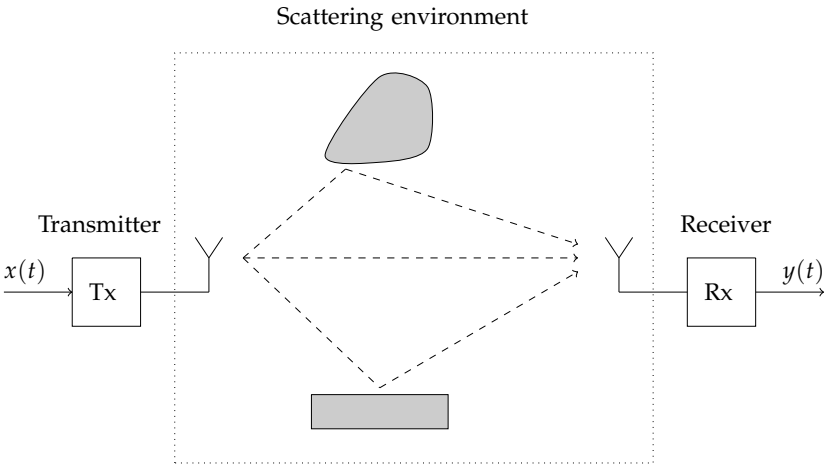

Figure 1.2: Block diagram of a wireless communication system.

The performance of any wireless network strongly depends on how electromagnetic waves propagate within the surrounding environment. Characterizing the radio channel is essential to the effective design, assessment and installation of future communication systems. Such systems are often represented with the block diagram shown in Fig. 1.2. At first, a signal $x(t)$ is amplified and radiated into space by the antenna of a Tx transmitter. Then, the electromagnetic waves propagate within the environment from Tx to the Rx antenna through multiple paths resulting from the scattering interactions with obstacles, such as buildings, mountains, trees, cars or human bodies. It is well-known [11] that the signal $y(t)$ received by the Rx receiver can be mathematically represented with the following convolution,

$$y(t) = \int h_t(\tau)\, x(t-\tau)\, d\tau \tag{1.1}$$

where h_t is the impulse response of the communication channel and varies over time with the scattering environment. The channel impulse response is often considered constant over the duration of the transmission of x. The

properties of h_t may vary with many parameters such as the frequency, the environment (urban, rural or green areas) and the position of the antennas.

The channel models have evolved along with the sophistication of the cellular systems. The first ones accounted for the shadowing attenuation resulting from the occlusion of waves by obstacles. Later, they characterized the fading due to the destructive interferences between multi-path components. The time delay dispersion of the channel is particularly critical when analysing the interference between symbols in digital transmission. With the emergence of techniques exploiting the spatial diversity of the multi-path components, a spatial information was required to predict the performance degradation produced by the statistical correlation between several sub-channels. Thanks to the simultaneous progress in electromagnetic theory, computational graphics and power, the deterministic approaches have gained significant interest in the last decade. By offering the advantage of providing fast deterministic results, they could be used as channel simulators, thereby replacing the need for costly measurements.

1.2 Geometrical database

The free access to realistic city models delivered by the public authorities plays a key role in the popularization of deterministic approaches. The three-dimensional representations are generally obtained from telemeters, e.g. Lidar, drones, and reconstructed from measurements or photographs using image processing techniques. The City Geography Markup Language (CityGML) is a standardised data model which defines different standard levels of detail (LoDs), ranging from 0 to 4, for 3D objects. An example of available geometry of LoD 2 of a neighborhood in Brussels, provided by the Centre d'Informatique pour la Region Bruxelloise (CIRB), is shown in Fig. 1.3. One can see that the buildings are represented by a volume with a simplified roof structure. The ground level can also be extracted from the digital terrain model (DTM).

With the trend to increase the frequency to mm-waves, one will have to take into account finer geometrical details in order to achieve accurate channel models. Geometrical and textural informations on bridges, railways, water zones, trees, city furniture, doors and windows are currently

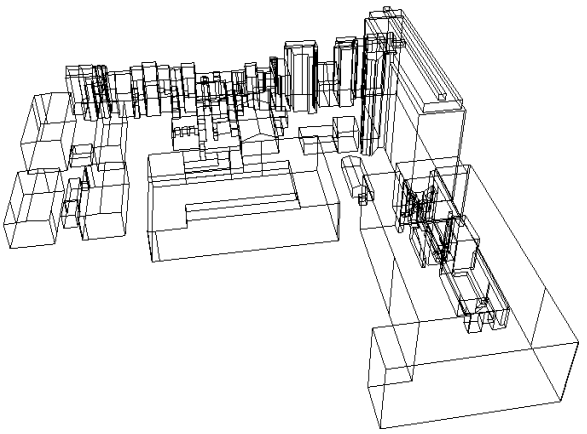

Figure 1.3: Illustration of available geometry in Brussels from CIRB [12].

being added to the database. In the longer term, the inclusion of the detailed interior features of the buildings will allow accurate indoor to outdoor simulations.

1.3 Computational electromagnetics

Physically, the channel impulse response h_t corresponds to the electrical voltage at the Rx antenna port when the electrical current fed into the Tx port is a Dirac delta pulse. The function h_t can thus be derived from a solution of the Maxwell's equations using a proper set of boundary conditions on the scattering environment. In practice, the analysis of the antennas and the wave propagation inside the environment are analysed separately. On one side, one assumes that the surrounding environment does not affect the technical properties of the antenna, i.e. its input impedance and radiation pattern. On the other side, one considers that the antenna acts as a point source and operates in the far-field. Even though this assumption may be questionable [5], it is common to extract the effect of the antenna pattern in the propagation simulation or measurement campaigns.

The computational electromagnetic (CEM) field numerically models the interactions between electromagnetic fields and objects. One can

mainly distinguish two approaches : the full-wave methods, i.e. integral or differential equation solvers, which aims to solve the Maxwell's equations using a fine spatial mesh and the high-frequency (HF) methods which are essentially derived from high-frequency approximation of Maxwell's equations.

The HF theories of diffraction were initiated in the mid-20th century with the Geometrical Theory of Diffraction (GTD) [13], a long time before the popularization of full-wave methods, to describe the scattered fields around edges in terms of rays for which the Geometrical Optics (GO) theory fails using only reflection or refraction mechanisms. The diffracted-field expressions are derived from the solutions of canonical problems, e.g. wedges, plane sectors, cylinders, cones and pyramids, and their accuracy increases with the frequency, i.e. when the object becomes electrically large. The Uniform Theory of Diffraction (UTD) [14] is the most popular technique and provides an accurate solution to the perfectly-conducting (PEC) wedge. However, in real-world structures, the edges are of finite extent and one must add corner-diffracted fields to contribute in the regions where the GO and edge-diffracted fields vanish. Currently, the exact derivation of corner-diffracted fields is hindered by the lack of a general analytical solution for the plane angular sector and for the infinite pyramid. In addition, the general solution of the impedance wedge problem is also unknown. In practice, an heuristic extension of the PEC case to the dielectric case is often used [15]. Finally, the diffraction by multiple edges is complex since the field diffracted by an isolated edge does not exhibit a ray structure everywhere in space. Thanks to their frequency-independent computational cost, ray-based methods are widely used within the propagation community. The provided physical picture of the scattering problem is particularly appreciated and allows a physical interpretation of the simulations or measurements by directly pointing out the most powerful ray contributions.

Ray-Tracing (RT) tools implement the HF theories to simulate the radio channels in both indoor or outdoor scenarios. If one considers a microcell with a typical coverage of 1 km in an urban area, several hundreds of buildings must be included in the RT simulations. A naive implementation leads to several days of computation. The time-consuming operation

in RT simulations consists of tracking the rays between Tx and Rx positions after encountering HF interactions. The number of computations can be lowered by using Ray-Launching (RL). In this technique, one basically launches a set of ray tubes from the transmitter in all directions using a pre-defined angular discretization of the antenna pattern. This approximation leads to an increasing number of tracking errors when the ray path gets longer. Another approach consists of accelerating the visibility computations using the fast algorithms developed in the Computer Graphics field. The computational complexity is essentially decreased by exploiting the a-priori information contained in the geometrical database using a hierarchical tree partition.

When the geometrical complexity of the structures increases, including details of smaller electrical size, the accuracy of RT methods degrades and their computation times rapidly increase. Diffuse scattering models [16] help to counteract this issue by stochastically modelling the effect of small-scale features. However, some researchers suggested to start from accurate full-wave methods and try to reduce their computational costs. A well-known technique consists of meshing the structure and solving the electric field integral equations (EFIE) with the Method-of-Moments (MoM). This results in a dense linear system of equations whose number of unknowns depends on the electrical size of the scatterers. The matrix-vector products involved in the iterative solution of the system can be accelerated using fast methods, such as the Multi-level fast multipole method (MLFMA) or the Fast Fourier Transform (FFT). Currently, the computational burdens are too high for the simulation of a three-dimensional propagation problem at GHz frequencies. However, the reduced two-dimensional problems are less time-consuming and have shown promising results for indoor [17] and outdoor [18] cases. When the transmitter is placed above the rooftops, a terrain height profile of cities, i.e. a vertical cut, provides accurate results. When both the transmitter and the receiver are located well above the ground level and below the rooftop level, one can reasonably assume that the buildings are of infinite height. Apart from these conditions, the reduced models may not account for important field contributions.

Finally, the intermediate techniques, sometimes qualified as hybrid, aim to provide more accurate results than RT within a computation time

lower than full-wave methods. The finite-difference time-domain (FDTD) method is combined with RT in [19] to predict the field scattered by parts of the structure containing electrically small details. An improved accuracy of the simulations is highlighted by a comparison with measurements for an outdoor-to-indoor realistic scenario at 1.29 GHz. However, the computation times, which are still presumably high, have not been specified for this example. Moreover, a detection scheme for the zones with finer details is needed. The authors of [20] developed a two-dimensional radio-coverage simulator which basically computes the scattered field resulting from the HF propagation mechanisms using radiation integrals of the current densities approximated with the Physical Optics (PO) theory. The latter integrals have been evaluated with a spatial-domain brute-force numerical technique or with an analytical far-field formula whenever possible. This simplistic acceleration approach results in consequent computation times, i.e. few hours. Moreover, the improvement in accuracy compared to RT is not clearly demonstrated neither by the theory or by the measurements.

1.4 Contributions

The guideline of this thesis is the development of a numerical method for simulating urban radio propagation which is more accurate than current RT and still provides results within a decent computation time.

The starting point is an intuition that the truncation effect due to the finite dimension of scatterers is better represented by the surface radiation integral rather than by considering explicit edge or corner asymptotic contributions. However, at UHF frequencies, the building walls are a few tens of wavelength wide and the integration of highly oscillating currents is a great challenge regarding computation time. This can be mitigated by benefiting from the long-standing research in the field of high-frequency fast computational methods. In particular, a previous work [21] on an inhomogeneous plane-wave decomposition has shown a rapid convergence when source and observation domains are sufficiently separated from each other.

The contributions of this thesis are summarized and ranked by importance as follows.

1. Sampling rules are derived for an accurate and concise field repre-

sentation with inhomogeneous plane waves (IPW) based on a linear contour deformation for scattering problems in which source and observation domains are visible within a limited angular sector. Given an error level, we derive closed-form expressions for the truncation limit, the sampling step and the contour slope that minimize the number of plane waves. A relation is drawn between the required number of plane waves and the degrees of freedom of the field, defined as the minimum number of orthonormal basis functions that represents scattered fields [22].

2. We develop a fast method to accelerate the computation of radiation integrals over arbitrarily oriented planar source and observation domains which lie in the intermediate field of each other. It combines the simplicity of the IPW representation with the $N \log N$ complexity of a recently proposed Unequally-Spaced Fast Laplace Transform [23]. This method also shows promising results in the case of parallel near-field plates as compared to other existing FFT-based techniques.

3. The Spectral-domain Physical Optics (SPO) is presented to evaluate the PO radiation integral over polygonal plates in intermediate-field regions. The integrations are carried out entirely in the spectral domain and the calculation does not require any spatial mesh. The resulting formulation extends the spectral integration proposed in [24], [25], [26] to complex-wavenumber spectra.

4. The geometrical visibilities between the facets are determined with a fast method which uses a Binary Tree Partitioning (BSP) representation of the city. This brings down the computational complexity for finding the lit surfaces from a given view-point from quadratic $O(N_f^2)$ to linear $O(N_f)$ with N_f the number of facets in the scene.

1.5 Outline

The manuscript is detailed hereafter.

In Chapter 2, we recall the plane-wave decomposition of scalar Green's functions and vector fields. We analyse the numerical errors inherent to an

IPW representation separately for intermediate- to far-field and for near-field distances. Concise error models are derived, discussed and inverted in order to provide simple sampling rules. Then, we estimate the required number of plane waves for intermediate- to far- field distances. The provided sampling formulas will be used throughout the thesis to control the spectral-domain numerical integrations for arbitrary source and observation domains.

In Chapter 3, it is proven that the plane-wave spectrum (PWS) of the Physical Optics (PO) field is analytical. This allows to express the scattered PWS in terms of the incident one and entirely perform the calculations in the spectral domain without any spatial mesh. The resulting spectral-domain formulation benefits from the decreasing number of IPWs with the field of view between source and observation plates. In addition, an uniform asymptotic evaluation of the PO spectral integrals is performed and helps to assess the accuracy of ray-optical representation of scattered fields in terms of Geometrical Optics (GO) and diffracted-field contributions.

In Chapter 4, we analyse the error resulting on the scattered field when using the PO approximation of the current on flat surfaces. We first review the asymptotic solutions of the wedge problem and re-derive them using a spectral-domain approach. This provides the physical insight used later on to analyse the PO results for the PEC plate and compare them with those obtained with the Method-of-Moments (MoM) or UTD.

In Chapter 5, we explain how multiple scattering interactions can be evaluated with PO to simulate urban radio propagation. The proposed method relies on the evaluation of shadows using the radiation integral and on the computation of multiple interactions only between plates lying within or nearby the regions illuminated by GO reflections. The visibility computations are accelerated using a three-step fast method based on a Binary Space Partitioning (BSP) representation of the geometry. Besides, it is observed that the computation cost of the SPO is still too high to simulate a moderate size city at GHz frequencies. Hence, another solution is therefore necessary to further reduce the computation costs.

In Chapter 6, we present a fast algorithm based on the recently proposed [23] Unequally-Spaced Fast Laplace transform for the scattering analysis of arbitrarily oriented large plates lying in each other

intermediate-field. The numerical results show important time savings w.r.t. both spectral-domain and spatial-domain numerical integrations.

Sampling rules for an inhomogeneous plane-wave representation of scattered fields

2

2.1 Introduction

Over the past years, the inhomogeneous plane-wave (IPW) methods have been developed to accelerate full-wave simulations of radar cross-sections, input impedances, radiation patterns of both electricly large and small objects [27], [28], that can possibly lie above or below a penetrable ground [29], [30], [31] and physical optics simulations of the radio-coverage of base station antennas located in urban environments [32], in which facets with size of hundreds of wavelengths stand in each other's near-fields.

Since the emergence of fast computational methods for high-frequency electromagnetics in the eighties, many field representations have been successfully proposed and applied, e.g. the multipole decomposition [33], the spherical wave functions [34], the Slepian's prolate spheroidal wave functions [35], [36], the complex point source [37], the homogeneous [38] and the inhomogeneous plane waves [39]. In one way or another, they all exploit the quasi band-limitation of the scattered fields outside the reactive

region [40]. Consequently, an efficient field reconstruction in intermediate- to far-field regions is achieved when the required number of coefficients is as close as possible to the degrees of freedom (DoF) [22] for a given accuracy. When fields are evaluated at close distances from the source, their spectrum becomes broadband and slowly decaying as a result of the singular near fields. This inevitably renders spectral-domain approaches computationally expensive. Nowadays, a remaining challenge concerns the mathematical derivation of invertible error models. For arbitrary geometries, such models form the only way to guarantee the accuracy of accelerated methods.

The IPW decomposition originates from a spectral representation of the fields in a given reference plane, each Fourier component corresponding to a plane wave. Then, a contour deformation is applied to circumvent the singularities and accelerate the numerical convergence. Because of the complex-valued wavevectors, the plane waves, qualified as "inhomogeneous", are both propagating and evanescent in the direction orthogonal to the reference plane. This expansion is particularly well suited to scattering problems in which source and observation domains see each other through a sufficiently small angular sector. Indeed, as will be demonstrated later, the number of plane waves needed is proportional to the electric dimensions of the scatterer and to the size of the observation sector. The IPW decomposition was exploited by [39] in the computational electromagnetics area to develop a fast integral-equation solver. The selected contour was the steepest descent path (SDP) in the angular domain since it annihilates the oscillations of the integrand around a given saddle point [41]. It is then possible to keep only the plane waves for which the wavevectors have a limited real part. Later in [27], the SDP is found impractical for large groups due to the presence of peaks and oscillations in the integrand. Hence, it is distorted into a discontinuous path including an interval on the real axis. The method, called fast inhomogeneous plane-wave algorithm (FIPWA), is less sensitive to numerical instabilities than the Fast Multipole Method (FMM) [33]. A strategy for the control of the truncation and extrapolation errors is presented in [42]. However, no general rules for error control are available so far. Recently, thanks to a change of the integration variables from angles to wavevectors [47], it was demon-

strated in [21], [50] that the integration with rectangles is efficient since the integrand along the SDP ressembles the Fourier transform of a modulated Gaussian function when the field is evaluated inside a small angular sector. In addition, an integration scheme that benefits from a compensation between the aliasing and the truncation errors has been developed. Among the many fast methods, FIPWA has shown the ability to accurately reconstruct the reactive fields [28], [29] in which the evanescent waves prevail. The IPW decompositions also inherit a long history of field analysis in multi-layered media [30], [43], [44], [45]. In this context, an important issue concerns the evaluation of the scattered fields from the analytical expression of the layered-medium Green's functions in the spectral domain. Since they contain poles and branch-points, the spectral integrals are usually computed using a contour deformation to circumvent the possible singularities or to avoid searching for their exact locations. Currently, the choice of the contour shape is purely heuristic and we can mention elliptic [46], parabolic [47], triangular [48] and exponentially-decaying [49] contours.

In this chapter, we first recall the plane-wave representation of scalar Green's functions and vector fields in Section 2.2. Then, we analyse the numerical errors inherent to an IPW field decomposition separately for intermediate- to far-field distances and for near-field distances in Section 2.3. In the first case, the analysis is carried out on the scalar free-space Green's function under the paraxial approximation and does not directly rely on the concept of quasi band-limitation. The truncation error as a result of the spectral domain finiteness, the discretization error as a result of the integrand sampling and the rounding error as a result of the computer's finite precision are derived, discussed and inverted in order to provide concise expressions and conditions for the truncation limit, the sampling step and the contour slope. Afterwards, we estimate the number of plane waves and the contour slope that minimizes it for intermediate- to far- field distances. This is an improvement compared to [21], [50] where error models developed for a SDP contour have not been inverted and the number of required plane waves was tabulated. A relation with the DoF of fields will be also carried out. Similarly, at sub-wavelength distances, the truncation and the discretization error models are derived and inverted.

Finally, conclusions are drawn in Section 2.4.

2.2 Spectral-domain formulation

2.2.1 Plane-wave representation of free-space Green's functions

Considering an observation point $\mathbf{r} = x\hat{\mathbf{x}} + y\hat{\mathbf{y}}$, the plane-wave decomposition of the two-dimensional free-space Green's function in Cartesian coordinates is

$$\begin{aligned} G(r) &= \frac{-j}{4} H_0^2(kr) \\ &= \frac{1}{2\pi} \int_{-\infty}^{\infty} \tilde{G}(k_x)\, e^{-jk_x x}\, \frac{\mathrm{d}k_x}{\mathrm{d}k_{xr}}\, \mathrm{d}k_{xr} \end{aligned} \tag{2.1}$$

where k is the free-space wavenumber, k_x is the spectral coordinate along $\hat{\mathbf{x}}$, $H_0^{(2)}$ is the Hankel's function of the second kind, the factor $\mathrm{d}k_x/\mathrm{d}k_{xr}$ accounts for the contour deformation, shown in 2.1, and the spectral Green's function is defined by

$$\tilde{G}(k_x) = \frac{e^{-jk_y|y|}}{2jk_y} \tag{2.2}$$

where $k_y = (k^2 - k_x^2)^{1/2}$ is the spectral coordinate along $\hat{\mathbf{y}}$. One can interpret the spectral-domain formulation (2.1) as a complex Fourier transform w.r.t. a lateral distance x. The absolute value in (2.2) imposes the parity w.r.t. y. The evanescence for $k_x > k$ is imposed through the right choice of the square root in the expression of k_y. Using the change of variables $k_x = k\sin\alpha$, $k_y = k\cos\alpha$, $y = r\cos\phi$ and $x = r\sin\phi$, one can rewrite (2.1) in a polar CS as

$$G(r) = \frac{-j}{4\pi} \int_{SIP} e^{-jkr\cos(\alpha-\phi)}\, \mathrm{d}\alpha \tag{2.3}$$

where the Sommerfeld's integration path (SIP) is shown in Fig. 2.1 for $\phi \in [-\pi/2, \pi/2]$.

Then, for an observation point $\mathbf{r} = x\hat{\mathbf{x}} + y\hat{\mathbf{y}} + z\hat{\mathbf{z}}$, the spectral decomposition of the three-dimensional free-space scalar Green's function in Carte-

sian coordinates is [51],

$$G(r) = \frac{e^{-jkr}}{4\pi r} = \frac{1}{4\pi^2} \iint_{-\infty}^{\infty} \tilde{G}(k_\rho)\, e^{-jk_x x - jk_y y}\, \frac{k_\rho}{k_{\rho r}} \frac{\mathrm{d}k_\rho}{\mathrm{d}k_{\rho r}}\, \mathrm{d}k_{xr}\mathrm{d}k_{yr} \tag{2.4}$$

with the spectral Green's function given by

$$\tilde{G}(k_\rho) = \frac{e^{-jk_z|z|}}{2jk_z} \tag{2.5}$$

Again, one can view the spectral decomposition as a complex Fourier transform w.r.t. spatial coordinates x and y. The function $\mathrm{d}k_\rho/\mathrm{d}k_{\rho r}$ accounts for a contour deformation along $k_\rho = (k^2 - k_z^2)^{1/2} = (k_x^2 + k_y^2)^{1/2}$ and the fraction $k_\rho/k_{\rho r}$ stems from a polar-to-cartesian change of variables [47]. Given $k_x = k_\rho \cos\alpha$, $k_y = k_\rho \sin\alpha$, $x = \rho\cos\phi$, $y = \rho\sin\phi$ and $\rho = (x^2 + y^2)^{1/2}$, we can re-express the plane-wave decomposition into cylindrical coordinates,

$$G(r) = \frac{1}{2\pi} \int_0^{\infty} \tilde{G}(k_\rho)\, J_0(k_\rho\rho)\, k_\rho\, \frac{\mathrm{d}k_\rho}{\mathrm{d}k_{\rho r}}\, \mathrm{d}k_{\rho r} \tag{2.6}$$

which is sometimes called Sommerfeld's identity and benefits from the fact that Green's functions are axially symmetrical. This relation has been extensively used for the tabulation of layered media Green's function. Switching to spherical coordinates with $k_x = k\sin\beta\cos\alpha$, $k_y = k\sin\beta\sin\alpha$, $k_z = k\cos\beta$, $x = r\sin\theta\cos\phi$, $y = r\sin\theta\sin\phi$ and $z = r\cos\theta$ leads to Weyl's identity [51],

$$G(r) = \int_0^{2\pi} \int_{SIP^+} e^{-jkr(\sin\theta\sin\beta\cos(\alpha-\phi)+\cos\theta\cos\beta)}\, \sin\beta\, \mathrm{d}\beta\mathrm{d}\alpha \tag{2.7}$$

where SIP^+ is the positive part of the SIP contour depicted in 2.1.

One can note that the spectral Green's functions (2.2) and (2.4) are singular at $k_x = \pm k$ or $k_\rho = k$ while the angular relations (2.3), (2.7) are not. In addition, one can infer that k_y is a multi-valued function with branch-points at $k_x = \pm k$ by factorizing it into

$$k_y = \sqrt{k^2 - k_x^2} = \sqrt{k - k_x}\,\sqrt{k + k_x} \tag{2.8}$$

This relation indicates that we can not perform a closed loop around an isolated branch-point without increasing the phase of k_y by π. In Fig. 2.1, we have thus plotted frequently-used branch cuts ranging from $\pm k$ to $\pm(k + j\infty)$ which are denoted by *classical branch cuts*. Those cuts produce improper regions in the complex plane where the plane waves grow exponential, i.e. $k_{yi}, k_{zi} > 0$. Instead, one can use to the Sommerfeld branch-cuts defined by

$$\begin{aligned} k_{xr}k_{xi} &= 0 \\ k_{xi}^2 - k_{xr}^2 &> 0 \end{aligned} \tag{2.9}$$

Those cuts lie on the imaginary axis and on the real axis and produce a complex plane without improper regions, i.e. $k_{yi} < 0$, as illustrated in Fig.2.1.

Finally, in order to to circumvent the free-space singularities and to accelerate the numerical convergence of the integral, the k_x-component in (2.4) and the radial component k_ρ in (2.4) follow a path in the complex plane. It generally lies in the first and third quadrant of the complex plane to prevent us from crossing the branch cuts. Among the many popular contour deformations, we have plotted in Fig. 2.1 :

– A linear contour with a parametrizable slope a,

$$k_{xi} = a k_{xr} \tag{2.10}$$

– The steepest-descent path (SDP) for a saddle-point at $k_x = 0$ and a lossless medium [21],

$$k_{xi} = \frac{k_{xr}}{(1 + (k_{xr}/k)^2)^{1/2}} \tag{2.11}$$

See Appendix 2.5.1 for the derivation of SDP for a lossy medium.

– A parabolic contour of height ak [47],

$$k_{xi} = \text{sign}(k_{xr})\ \frac{a}{k}\ \left(k^2 - (k_{xr} - k)^2\right) \tag{2.12}$$

– An exponentially decaying contour with initial slope a [49],

$$k_{xi} = a k_{xr}\ e^{1 - k_{xr}/k} \tag{2.13}$$

The shape of the contour and its parametrization are entirely governed by the critical dimensions of the source and the observation domain, i.e. the distance z/λ and the field of view ρ/z, as well as by the targeted relative error ϵ. For instance, when the distance z is much larger than the wavelength and the field of view is much smaller than one, the steepest descent path (SDP) is relevant because it keeps the imaginary part of the exponent $-jk_{zi}$ constant and decreases rapidly away from the saddle-point. However, when the field of view ρ/z increases, the integrand starts to oscillate and its amplitude grows considerably. Consequently, its numerical integration along the SDP is no longer optimal and, in some cases, not even converging. At near-field distances $z \ll \rho$, the spectrum decays very slowly and one generally prefers a path which returns on the real-axis, such as parabolic or exponentially-decaying contours.

2.2.2 Decomposition of vector fields

In the spatial domain, the electric and the magnetic field are obtained from a convolution of the induced surface electric currents $\mathbf{J}$ on the source domain S' with dyadic Green's functions [54],

$$\begin{aligned}\mathbf{E}(\mathbf{r}) &= -jk\eta \iint \mathbf{G}_e(\mathbf{r}-\mathbf{r}')\cdot\mathbf{J}(\mathbf{r}')\,\mathrm{d}S' \\ \mathbf{H}(\mathbf{r}) &= \iint \mathbf{G}_h(\mathbf{r}-\mathbf{r}')\times\mathbf{J}(\mathbf{r}')\,\mathrm{d}S'\end{aligned} \tag{2.14}$$

where η is the free-space impedance, $\mathbf{r}'$ is the position of a source point on S', $\mathbf{G}_e = (\mathbf{I} + 1/k^2\nabla\nabla\cdot)G(R)$ and $\mathbf{G}_h = \nabla G(R)$ are the dyadic electric and magnetic Green's functions in which $R = ||\mathbf{r}-\mathbf{r}'||$ is the distance between source and observation points, $\mathbf{I}$ is the identity matrix, $\nabla\cdot$ and ∇ are the div and grad operators, respectively.

As shown in Fig. 2.2, we will consider a local system of coordinates (CS) centred on the source domain S' and oriented toward an observation point $\mathbf{r} = x\hat{\mathbf{x}} + y\hat{\mathbf{y}} + z\hat{\mathbf{z}}$. With this CS, any source point $\mathbf{r}' = x'\hat{\mathbf{x}} + y'\hat{\mathbf{y}} + z'\hat{\mathbf{z}}$ satisfies $z \geq z'$. Under those conditions, the inhomogeneous plane-wave decomposition of the free-space Green's function appearing in (2.14) reads

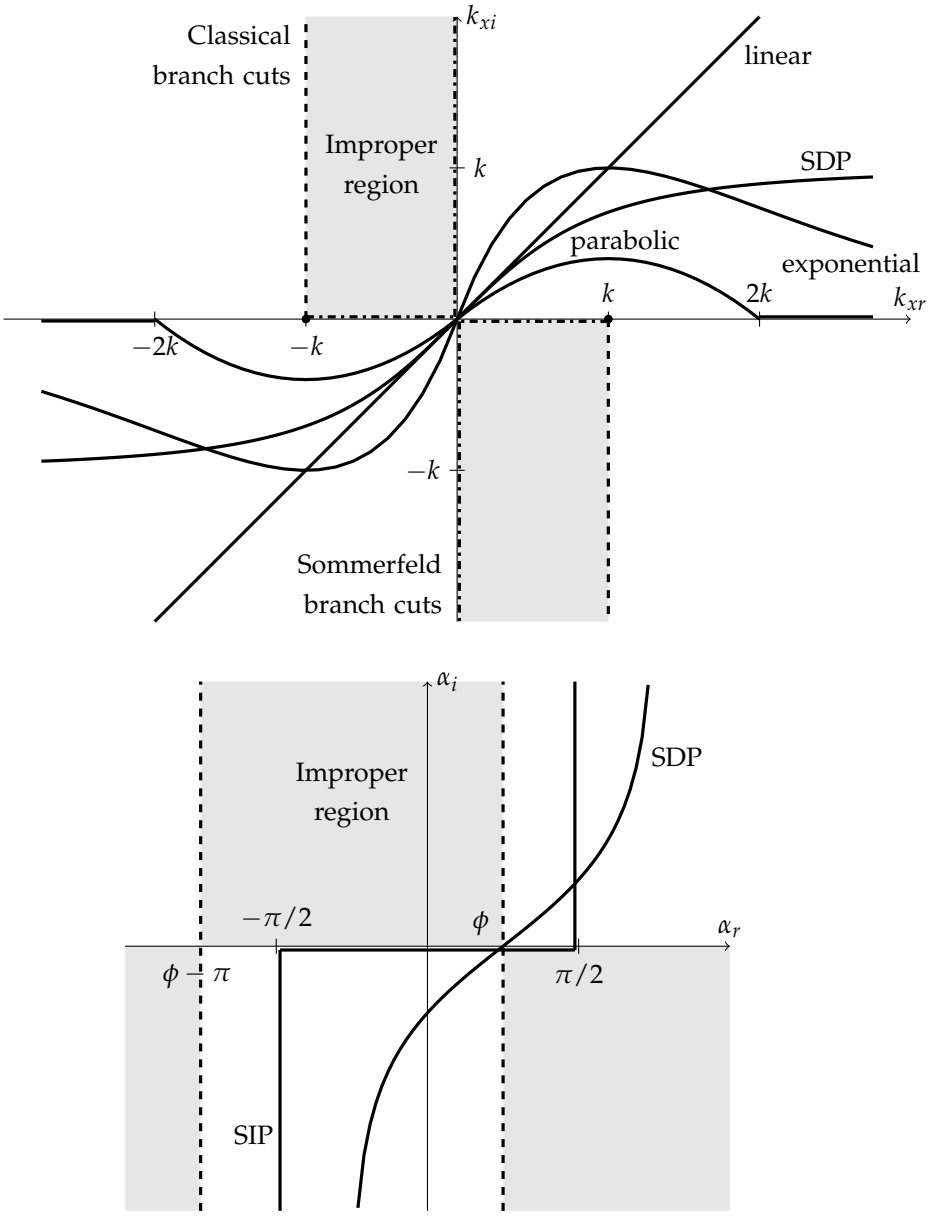

Figure 2.1: Illustration of several contours in Cartesian coordinates (top) and in polar coordinates for $\phi \in [-\pi/2, \pi/2]$ (bottom).

as

$$G(R) = \frac{-j}{8\pi^2} \iint_{-\infty}^{\infty} e^{-jk_x x - jk_y y - jk_z z}\, e^{jk_x x' + jk_y y' + jk_z z'} \frac{k_\rho k_z}{k_{\rho r}} \frac{\mathrm{d}k_\rho}{\mathrm{d}k_{\rho r}}\, \mathrm{d}k_{xr}\mathrm{d}k_{yr} \tag{2.15}$$

The exponential in the integrand of (2.15) has been explicitly factorized to highlight the separability of source and observation coordinates. Inserting (2.15) into (2.14) and swapping the integrals leads to a spectral-domain formulation [29],

$$\begin{aligned} \mathbf{E}(\mathbf{r}) &= \frac{-j}{8\pi^2} \iint \tilde{\mathbf{E}}(\mathbf{k})\, \frac{e^{-j\mathbf{k}\cdot\mathbf{r}}}{k_z}\, \frac{k_\rho}{k_{\rho r}}\, \frac{\mathrm{d}k_\rho}{\mathrm{d}k_{\rho r}}\, \mathrm{d}k_{xr}\mathrm{d}k_{yr} \\ \mathbf{H}(\mathbf{r}) &= \frac{-j}{8\pi^2} \iint \tilde{\mathbf{H}}(\mathbf{k})\, \frac{e^{-j\mathbf{k}\cdot\mathbf{r}}}{k_z}\, \frac{k_\rho}{k_{\rho r}}\, \frac{\mathrm{d}k_\rho}{\mathrm{d}k_{\rho r}}\, \mathrm{d}k_{xr}\mathrm{d}k_{yr} \end{aligned} \tag{2.16}$$

The plane-wave spectrum (PWS) of the electric and magnetic field, sometimes called the complex patterns, are defined by

$$\begin{aligned} \tilde{\mathbf{E}}(\mathbf{k}) &= -jk\eta \left(\tilde{\mathbf{J}}(\mathbf{k}) - (\tilde{\mathbf{J}}(\mathbf{k}) \cdot \mathbf{k})\, \mathbf{k}/k^2 \right) \\ \tilde{\mathbf{H}}(\mathbf{k}) &= -j\, \mathbf{k} \times \tilde{\mathbf{J}}(\mathbf{k}) \end{aligned} \tag{2.17}$$

in which $\mathbf{k} = k_x\hat{\mathbf{x}} + k_y\hat{\mathbf{y}} + k_z\hat{\mathbf{z}}$. The complex Fourier transform of the current distribution is expressed as

$$\tilde{\mathbf{J}}(\mathbf{k}) = \iint \mathbf{J}(\mathbf{r}')\, e^{j\mathbf{k}\cdot\mathbf{r}'} \mathrm{d}S' \tag{2.18}$$

Discretizing relations (2.16) yields

$$\begin{aligned} \mathbf{E}^d(\mathbf{r}) &= \sum_p \sum_q w_{pq}\, \tilde{\mathbf{E}}(\mathbf{k}_{pq})\, e^{-jk_{x,pq}x - jk_{y,pq}y - jk_{z,pq}z} \\ \mathbf{H}^d(\mathbf{r}) &= \sum_p \sum_q w_{pq}\, \tilde{\mathbf{H}}(\mathbf{k}_{pq})\, e^{-jk_{x,pq}x - jk_{y,pq}y - jk_{z,pq}z} \end{aligned} \tag{2.19}$$

where the superscript d stands for a discrete representation and the spectral weight is

$$w_{pq} = \frac{-j\Delta k^2}{8\pi^2 k_{z,pq}} \frac{k_{\rho,pq}}{k_{\rho r,pq}} \frac{\mathrm{d}k_{\rho,pq}}{\mathrm{d}k_{\rho r,pq}} \tag{2.20}$$

where Δk is the sampling step along real spectral coordinates. It is important to recall that the integrals (2.16) and (2.17) must be evaluated in a local

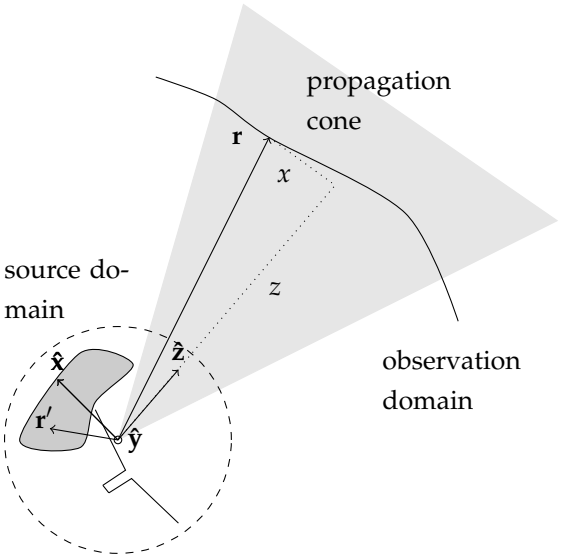

Figure 2.2: Cut view of the problem geometry with a local system of coordinates

system of coordinates (CS) with $(\hat{\mathbf{x}}, \hat{\mathbf{y}}, \hat{\mathbf{z}})$. This results from the dependence of the contour deformation on the direction of the z-axis.

Given that the coordinates $k_{z,pq}$ have real and imaginary parts, the plane waves, qualified as "inhomogeneous", are both propagating and evanescent w.r.t the forward direction $\hat{\mathbf{z}}$. A property of any plane-wave expansion is the separability of the source and observation coordinates within the spectral integral (2.4). From a computational perspective, this separability allows us to store the samples of the plane-wave spectrum (2.17) and reuse them for another field evaluation. From a physical perspective, the plane waves, which are solutions to Maxwell's equations, can further propagate and provide a field representation over an extended domain. In contrast to purely propagating plane-wave expansions, e.g. in the FMM algorithm, the inhomogeneous plane-wave decomposition has the feature of being spatially selective. Generally, the field can only be reconstructed inside a conical region, as depicted in Fig. 2.2. Moreover, the IPW field expansion is not exposed to numerical instabilities when the observation point approaches the source since it does not entail the attempt to extract near-field information from far-field patterns.

Finally, we can be established a relation with the far-field approximation by selecting a CS with z-axis pointing exactly toward the observation point, i.e. $\mathbf{r} = z\hat{\mathbf{z}}$. When $kz \to \infty$, we can deform the contour of (2.16) into the SDP (2.11), approximate the field PWS (2.17) by its value at $k_\rho = 0$ and factorize it out of the integral,

$$\begin{aligned}\mathbf{E}(\mathbf{r}) &= \frac{e^{-jkz}}{j8\pi^2}\,\tilde{\mathbf{E}}(k\hat{\mathbf{z}}) \iint_{-\infty}^{\infty} \frac{e^{-jk_{\rho r}^2/(kS)}}{k_z}\,\frac{k_\rho}{k_{\rho r}}\,\frac{\mathrm{d}k_\rho}{\mathrm{d}k_{\rho r}}\,\mathrm{d}k_{xr}\mathrm{d}k_{yr} \\ &= \tilde{\mathbf{E}}(k\,\hat{\mathbf{z}})\,G(z) \end{aligned} \tag{2.21}$$

where $S = (1 + (k_{\rho r}/k)^2)^{1/2}$.

2.3 Numerical errors

In this section, the mathematical identities are established for the estimation of error sources inherent to the numerical integration in (2.4), i.e. the truncation error as a result of the spectral domain finiteness, the discretization error as a result of the integrand sampling and the rounding error as a result of the computer's finite precision.

In this paragraph, we explain why the error levels derived for the scalar Green's function can be extended to vector fields. As demonstrated in [40], the absolute error resulting from a field decomposition is bounded by the product of the maximum possible field value and an error measure of the dyadic Green's function,

$$|\mathbf{E}^d(\mathbf{r}) - \mathbf{E}(\mathbf{r})| \leq |\mathbf{E}^{\max}| \cdot |\bar{\boldsymbol{\epsilon}}| \tag{2.22}$$

with

$$\begin{aligned}|\mathbf{E}^{\max}| &= \frac{k\eta}{d_{\min}} \iiint |\mathbf{J}(\mathbf{r}')|\,dV' \\ |\bar{\boldsymbol{\epsilon}}| &= d_{\min} \max_{\mathbf{r},\mathbf{r}'} |\bar{\mathbf{G}}^d(\mathbf{r},\mathbf{r}') - \bar{\mathbf{G}}(\mathbf{r},\mathbf{r}')| \end{aligned}$$

where $\bar{\boldsymbol{\epsilon}}$ is a matrix and $d_{\min}$ is the minimum distance between source and observation domains. The upper bound (2.22) links the maximum absolute error of the electric field with that of the dyadic Green's function. This relation is no longer valid for the relative error. Indeed, the field can be much lower than its maximum value within some observation domains, e.g. in

the shadow region of a scatterer or around the sidelobes of a directive antenna. This issue will be highlighted through an example in Chapter 3.

2.3.1 Intermediate- to far-field distances

In the mathematical derivations below, we will repetitively use a paraxial, or small-angle, approximation. In the spectral domain, it consists of replacing $k_z \approx k$ in the denominator [21] and of performing a second order Taylor's series of k_z in the exponential,

$$k_z \approx k - \frac{k_\rho^2}{2k} \tag{2.23}$$

which is accurate when $|k_m| \ll k$. After substituting those approximations in the plane-wave decomposition of the Green's function, (2.4) becomes the two-dimensional Fourier transform of a Gaussian function which is equal to,

$$G(r) \approx \frac{e^{-jkz-jk\rho^2/(2z)}}{4\pi z} \tag{2.24}$$

Clearly, this relation establishes an equivalence with the paraxial approximation of the Green's function in the spatial domain which requires $\rho \ll z$ and $kz \gg 1$, i.e. a field of view much smaller than one and a distance z much larger than the wavelength. In the whole manuscript, the field of view will be defined by the maximum value of the ratio ρ/z among the observation points lying within the observation domain. Moreover, additional conditions on the contour slope α will be introduced s.t. the errors resulting from the numerical integration of the exact integrand and the integrand approximated with (2.23) are comparable. In addition, we will make use of the near-field coefficient defined in [110] as

$$C = 2\pi F = \frac{k\rho^2}{z} = \frac{\pi}{4}\frac{z_f}{z} \tag{2.25}$$

where F is the Fresnel number and $z_f = 8\rho^2/\lambda$ is the Fraunhofer limit. According to IEEE Standard for Definitions of Terms for Antennas, $C < \pi/4$ ($z_f/z < 1$) corresponds to the far-field region and $C > \pi/4$ ($z_f/z > 1$) corresponds to the intermediate-to-near field region. It is important to mention that the paraxial approximations will be limited to the determination

of the sampling rules, while the exact formulation will be used for field calculations. It will be shown in Chapter 3 that the error models derived in that way can still be used to represent the field in the intermediate-to-near field region.

It is proven in Appendix 2.5.4 that the elements of $\bar{\epsilon}$ are of the same order of magnitude as the relative error of the scalar Green's function G evaluated at $z = d_{\min}$ and $\rho = \rho_{\max}$,

$$\epsilon = \frac{G(r) - G^d(r)}{G(r)} \tag{2.26}$$

where $r^2 = \rho_{\max}^2 + d_{\min}^2$, $\rho_{\max}$ is the sum of the radial extents of the source and the observation domains and G^d is the discrete IPW decomposition of G. In the following, we will thus only analyse ϵ.

2.3.1.1 Truncation error

The $k_x k_y$ spectral domain is limited to a disk of radius k_{mr}. Compared to a square integration domain, the area is reduced by a factor $\pi/4$ and the error ϵ is axially symmetrical. The corresponding complex-valued limit is given by $k_m = k_{mr} + jk_{mi}$.

When the approximation (2.23) holds, the truncation error can be estimated with the help of (2.6), (2.23) and (2.24) as

$$\epsilon \approx \frac{-jz}{k}\, e^{jk\rho^2/(2z)} \int_{k_m}^{\infty} e^{jk_\rho^2 z/(2k)} J_0(k_\rho \rho)\, k_\rho \mathrm{d}k_\rho \tag{2.27}$$

Then, as proven in Appendix 2.5.2, the error can be approximately bounded by,

$$-\ln|\epsilon| \gtrsim k_{mr}k_{mi}z/k - k_{mi}\rho \tag{2.28}$$

From there, for a linear contour deformation of slope a, i.e. for $k_{mi} = ak_{mr}$ the truncation limit is given by the root of a quadratic polynomial,

$$k_{mr} \gtrsim \frac{k\rho}{z}\left(\frac{1}{2} + \sqrt{\frac{1}{4} - \frac{\ln|\epsilon|}{aC}}\right) \tag{2.29}$$

The spectral approximation (2.23) made in (2.27) requires $|k_m| \ll k$. By considering successively the real and the imaginary parts of k_m, we can

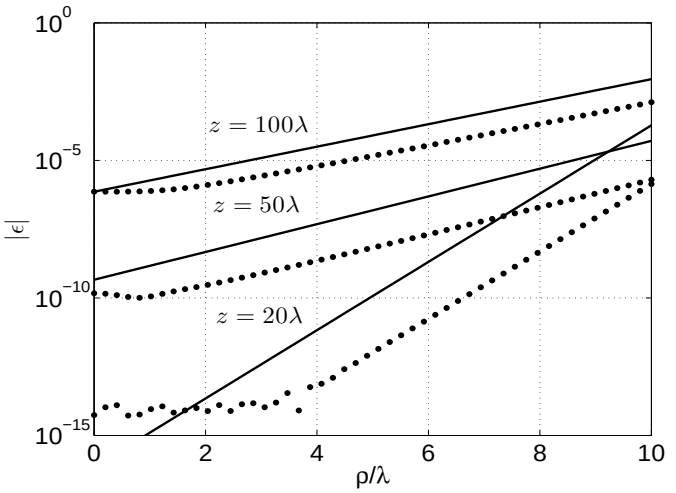

Figure 2.3: Upper bound (solid) and exact value (dotted) of the truncation error for $(a, z, k_{mr}) = \{(0.7, 20\lambda, 0.7k); (0.5, 50\lambda, 0.37k); (1, 100\lambda, 0.15k)\}$.

extract four underlying conditions given (2.29),

$$\frac{\rho}{z} \ll 1 \ , \ a \ll \frac{z}{\rho} \ , \ a \ll \frac{-kz}{\ln|\epsilon|} \ , \ a \gg \frac{-\ln|\epsilon|}{kz} \tag{2.30}$$

The first condition defines the paraxial regime. The second condition will always be satisfied since the optimal contour slope is smaller than one, as we will show later. The third and fourth conditions generate an interval for the contour slope which is not restrictive when the distance z is much larger than the wavelength.

In Fig. 2.3, the upper bound (2.28) is validated for three values of the linear contour slope a and distances z selected to satisfy (2.30). The large range of validity of (2.28) is observed. One can see that the solid curve (upper bound) is always above to the dashed curve (exact error). The stabilization of the exact error around 10^{-14} at the lower values of ρ/λ has been associated with the round-off error.

2.3.1.2 Discretization error

We will now consider a numerical integration performed in the $k_x k_y$ spectral domain with a rectangle rule using a left-endpoint approximation

of the integrand. Discretizing (2.4) with a rate Δk is equivalent to multiplying the integrand with the Fourier series of a Dirac comb,

$$\epsilon = \frac{-j}{8\pi^2 G(r)} \iint \frac{q_\rho k_\rho}{k_z k_{\rho r}} e^{-j\mathbf{k}\cdot\mathbf{r}} \sum_m \sum_n e^{-jk_{xr}2\pi m/\Delta k - jk_{yr}2\pi n/\Delta k} \, \mathrm{d}k_{xr}\mathrm{d}k_{yr} \tag{2.31}$$

where $(n, m) \in \mathbb{Z}_0^2$ and the term $(0, 0)$ corresponds to the exact plane-wave decomposition of the Green's function (2.4). After swapping sums and integrals and grouping the arguments of the exponentials, we can identify for each term a complex modulation factor in the spectral domain corresponding to a complex-valued shift in the spatial domain [58],

$$\epsilon = \frac{1}{G(r)} \sum_m \sum_n G\left(r_{mn}\right) \tag{2.32}$$

where the complex-valued distance is

$$r_{mn} = \left((x - m\Delta x)^2 + (y - n\Delta y)^2 + z^2\right)^{1/2} \tag{2.33}$$

and $\Delta y = \Delta x = 2\pi/(\Delta k(1 + ja))$ are complex shifts in the spatial domain. For the case $|\Delta y| \ll z$ and an observation domain within a disk of radius ρ, it is proven in Appendix 2.5.3 that the error is

$$-\ln|\epsilon| \approx \frac{2\pi k a}{z\Delta k\,(1 + a^2)} \left(\frac{2\pi}{\Delta k\,(1 + a^2)} - \rho\right) \tag{2.34}$$

The inverse relation for the sampling step Δk is again obtained through the root of a quadratic polynomial,

$$\Delta k = \frac{2\pi}{(1 + a^2)\,\rho} \left(\frac{1}{2} + \sqrt{\frac{1}{4} - \frac{\ln|\epsilon|}{aC}}\right)^{-1} \tag{2.35}$$

Expression (2.35) is accurate when $|\Delta y| \ll z$ and it can be proven that the underlying conditions are exactly those of (2.30).

The identity (2.32) can be interpreted as a generalization of the Nyquist-Shannon sampling theorem to Laplace transforms on a linear path and takes implicitly into account the intricacy of contouring the free-space singularity. It also establishes an equivalence between a discrete plane-wave representation and an infinite set of parasitic sources with complex-valued

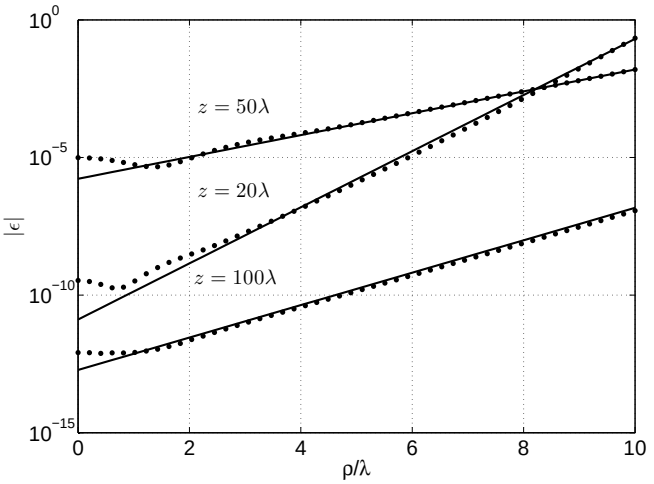

Figure 2.4: Model (solid) and exact value (dotted) of the discretization error for $(a, z, dk) = \{(0.7, 20\lambda, 0.063k); (0.5, 50\lambda, 0.055k); (1, 100\lambda, 0.023k)\}$.

translated coordinates. The model of (2.34) is validated in Fig. 2.4 for the same contour slopes and distances as in Fig. 2.3. One can observe that the numerically computed relative error ϵ (dotted) is almost superimposed with the model (solid). For lower values of ρ/λ, we notice a little discrepancy associated to the contribution of the three other nearest replicas in (2.32).

2.3.1.3 Round-off error

When the electric dimensions ρ/λ increase, the integrand of (2.4) quickly grows by several orders of magnitude while the Green's function does not. Indeed, the integrand samples oscillate and should thus compensate each other. However, due to the finite precision with which calculations are carried out, a round-off error remains. This ill-conditioning is inherent to any inhomogeneous plane-wave decomposition since its basis element, the IPW, is growing exponentially w.r.t. xy due to the presence of the $e^{k_{xi}x+k_{yi}y}$ factor in the spectral integral (2.4). Considering a random complex-valued noise $n(k_{xr}, k_{yr})$ and the approximation (2.23), it is proven in Appendix 2.5.5 that the relative round-off error can be approximated

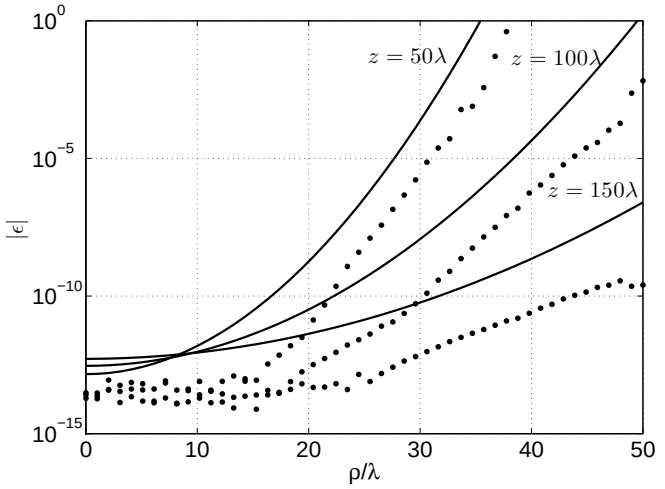

Figure 2.5: Upper bound (solid) and exact value (dotted) of the round-off error for $(a, z) = \{(0.75, 50\lambda); (0.75, 100\lambda); (0.5, 150\lambda)\}$.

with

$$\epsilon \approx \frac{-jz^2}{2\pi}\, e^{jk\rho^2/(2z)} \iint n\, e^{jk_\rho^2 z/(2k)}\, e^{-jk_x x - jk_y y}\, \frac{k_\rho}{k_{\rho r}}\, \frac{\mathrm{d}k_\rho}{\mathrm{d}k_{\rho r}}\, \mathrm{d}k_{xr}\mathrm{d}k_{yr} \tag{2.36}$$

As also proven in Appendix 2.5.5, it can be bounded by

$$|\epsilon| \leq\ kz\epsilon_m\, \frac{1+a^2}{a}\, e^{ak\rho^2/(4z)} \tag{2.37}$$

where $\epsilon_m = 2.2 \times 10^{-16}$ corresponds to the machine error level for double precision. Noticing that $e^x/x \leq e^x$ when $x > 1$ and that the approximation $1 + a^2 \approx 1$ holds since the optimal contour slope is always less than 1 as we will see in Section 2.3.1.4, the inverse relation provides a maximum value for the contour slope

$$a \leq \frac{4}{C}\, \ln\left(\frac{|\epsilon|}{\epsilon_m (k\rho)^2}\right) \tag{2.38}$$

when $4\epsilon/(\epsilon_m(k\rho)^2) > 1$. This inequality implies that the contour slope should be lowered when the near-field coefficient increases. The exact round-off error and its upper bound (2.37) are compared in Fig. 2.5 for three distances and contour slopes selected s.t. the distances is in the order

of dozens of wavelength and the round-off error starts to affect the numerical integration.

2.3.1.4 Optimal integration scheme

In this section, we evaluate the number of plane waves P required to achieve a given relative error ϵ. For the two-dimensional plane-wave representation of (2.4), it is given by

$$P = \pi \left(\frac{k_{mr}}{\Delta k} \right)^2 \tag{2.39}$$

where the factor π results from the integration over a disc. In practice, P is obtained by solving a Gauss circle problem [55] and can slightly differ from approximation (2.39). Targeting equal truncation and discretization errors, it is demonstrated in Appendix 2.5.6 with the help of (2.29), (2.35) and (2.39) that

$$\sqrt{\pi P} \sim \frac{C}{2} \left(1 + a^2\right) \left(1 - \frac{2 \ln |\epsilon|}{aC} \right) \tag{2.40}$$

where we assume that the overestimation of P resulting from the use of the lower bound (2.29) is small because of the slow dependence of k_{mr} w.r.t. ϵ. The contour slope that minimizes P is obtained by cancelling out the derivatives of (2.40) and solving the following cubic equation

$$-\frac{C}{\ln |\epsilon|} a^3 + a^2 - 1 = 0 \tag{2.41}$$

for which the real positive root is developed in Appendix 2.5.7. Since the expression (2.80) is relatively complicated, we will analyse its asymptotic behaviour. When the coefficient $-C/\ln|\epsilon|$ is much larger than 1 (near field and/or low accuracy), the second-order term of (2.41) becomes negligible compared to the third order. Then, solving the reduced cubic equation yields

$$a \sim \left(\frac{-\ln |\epsilon|}{C} \right)^{1/3} \tag{2.42}$$

When the coefficient $-C/\ln|\epsilon|$ is much smaller than 1 (far field and/or high accuracy), we can neglect the third-order term of (2.41) and obtain,

$$a \approx 1 \tag{2.43}$$

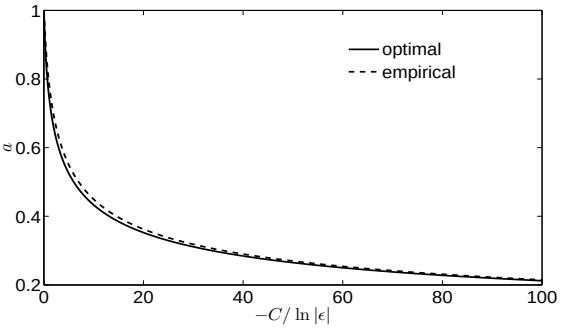

Figure 2.6: Optimal and empirical contour slope a as function of $-C/\ln|\epsilon|$

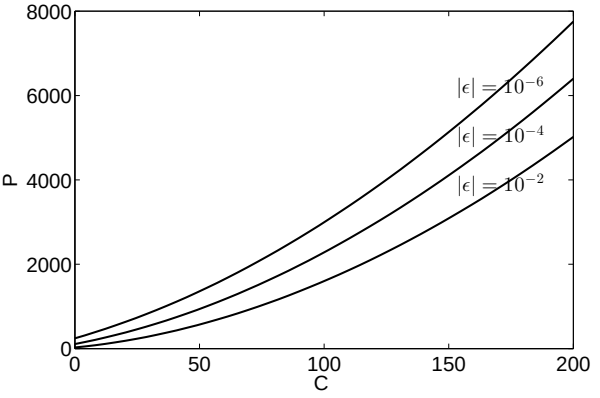

Figure 2.7: Required number of plane waves vs. the near-field parameter C for three relative errors.

Instead of the relatively complicated expression (2.80) given in Appendix 2.5.7, the user may consider (2.42) and (2.43), combined with an empirical transition rule, such as

$$a = \left(1 - \frac{C}{\ln|\epsilon|}\right)^{-1/3} \tag{2.44}$$

From Fig. 2.6, one can infer that the empirical slope of (2.44) agrees well with the optimal slope of (2.80).

For the case where the asymptotic expression (2.42) is accurate, i.e. $-C/\ln|\epsilon| \gg 1$, it is proven in Appendix 2.5.6 that the number of plane

waves is asymptotically given by

$$P \sim \frac{C^2}{4\pi}\left(1 + 3\,(-\ln|\epsilon|)^{2/3}\,C^{-2/3}\right)^2 \tag{2.45}$$

The number of plane waves is illustrated in Fig. 2.7 as a function of the near-field parameter C for three error levels. One can observe that the convergence rate is high since the number of plane waves varies slowly w.r.t ϵ. One can also note that the powers of the near-field coefficient C and of $-\ln|\epsilon|$ present in (2.45) are equal to those obtained in [22] and [53] in the context of the error control of the FMM algorithm.

Next, we will establish a relation between the number of plane waves (2.45) and the degrees of freedom (DoF) of the scattered field [22], defined as the minimum number of orthonormal basis functions needed to represent a given field distribution. Let us consider two spheres of minimum radius ρ_s and ρ_o enclosing source and observation domains for which centers $\mathbf{r}_o$ and $\mathbf{r}_s$ are separated by a distance $z = ||\mathbf{r}_s - \mathbf{r}_o||$, respectively. By setting the relative error $|\epsilon|$ to one and ρ to $\rho_s + \rho_o$ in (2.45) in order to account for the sizes of both the source and the observation domains, we obtain

$$P_0 = \frac{k^2(\rho_o + \rho_s)^4}{4\pi z^2} \tag{2.46}$$

When the observation domain is a disk, the number of DoF $N_0 = (k\rho_s\rho_o/z)^2/\pi$ is obtained by taking the square of equation (30) in [22] and multiplying it with $\pi/4$. From there, we can write

$$\frac{P_0}{N_0} = \frac{(\rho_o + \rho_s)^4}{4\rho_s^2\rho_o^2} \tag{2.47}$$

for which a minimum value $P_0/N_0 = 4$ is achieved for $\rho_o = \rho_s$. When the observation domain is reduced to a point, i.e. $\rho_o = 0$, N_0 goes to zero while P_0 does not. The differences between N_0 and P_0 could be explained by noting that we are specifically targeting an IPW representation. For instance, we can mention that the a priori extraction of a phase factor $e^{-jk||\mathbf{r}-\mathbf{r}_s||}$ of the field over the observation domain, considered in the approach of [40], [22], has not been performed in this paper.

Finally, for increasing far-field distances, i.e. when $C/\ln|\epsilon| \to 0$, it can be easily proven from (2.29), (2.35) and (2.39) that the number of plane

waves converges towards

$$P = \frac{(-\ln|\epsilon|)^2}{\pi} \tag{2.48}$$

which only depends on the target accuracy $|\epsilon|$. This minimum number is higher than one and mathematically translates the intuition that interferences between plane waves are necessary to produce the $1/r$-decay of far fields. Table 2.1 gives the number of plane waves P, obtained by solving the Gauss quadrature [55], for three error levels $|\epsilon|$. The distances z are expressed in terms of the Fraunhofer limit z_f defined in (2.25) and are selected s.t. the relative error of the far-field approximation extracted from Fig. 1 in [56] is equal to $|\epsilon|$. One can infer that the number of plane-waves increases with $|\epsilon|$ according to (2.48) and remains large at far-field distances. However, in contrast to the far-field approximation, the IPW decomposition can achieve arbitrary error levels for a given distance z.

$\lvert\epsilon\rvert$	10^{-2}	10^{-3}	10^{-4}
z/z_f	1.5	5	15
$C/\ln\lvert\epsilon\rvert$	0.11	0.023	0.0057
P	27	27	47

Table 2.1: Number of plane-wave P for three error levels $|\epsilon|$ and distances z.

2.3.2 Near-field distances

In this section, truncation and discretization error models are derived and inverted for near-field distances z smaller than the wavelength. The analysis will be carried out on the three-dimensional free-space Green's function and its extension to vector fields can be obtained by bounding the derivatives of the error models, as it was done in Appendix 2.5.4 for intermediate- to far-field distances.

2.3.2.1 Truncation error

In the following derivations, the integrand of (2.4) will be again truncated to a disk of radius k_{mr}. For such distances, the envelope of the truncation error resembles a concave function and reaches its maximum value either at $\rho = 0$ or at $\rho = \rho_{\max}$. Hence, we will analyse both cases separately.

First, for low values of k_{mi}, the relative error is higher at a null distance ρ, as illustrated with case 2 and case 3 in Fig. 2.8 and in Fig. 2.9 for on-plane evaluation. This can be qualitatively explained by pointing out the greater importance of higher frequencies near the more singular part of the Green's function. Fortunately, the truncation error at $\rho = 0$ is given analytically by

$$\begin{aligned} \epsilon &= -jze^{jkz} \int_{k_m}^{\infty} \frac{e^{-jk_z z}}{k_z} \frac{\mathrm{d}k_\rho}{\mathrm{d}k_{\rho r}} \, k_\rho \, \mathrm{d}k_{\rho r} \\ &= e^{-j\sqrt{k^2-k_m^2}z+jkz} \end{aligned} \tag{2.49}$$

If we now suppose $|k_m| \gg k$, this relation can be inverted via

$$k_{mr} \approx -\frac{\ln|\epsilon|}{z} \tag{2.50}$$

The error at $\rho = 0$ is thus roughly independent of the imaginary part of the limit k_{mi}. One can also prove from (2.50) that $|k_m| \gg k$ is valid when $z/\lambda \ll -\ln|\epsilon|/(2\pi)$, i.e. at distances much smaller than the wavelength.

For distances $|k_m|\rho \gg 1$, we can perform a first-order integration by parts of (2.6) using an asymptotic series of the primitive of the zero-order Bessel's function [57],

$$\epsilon \sim -\sqrt{\frac{2}{\pi}} \, e^{jkr-jk_{zm}z} \sum_{n=0}^{\infty} \frac{\lambda_n}{(k_m\rho)^{n+1/2}} \, \sin\left(k_m\rho - \frac{2n+1}{4}\pi\right) \tag{2.51}$$

where $k_{zm} = (k^2 - k_m^2)^{1/2}$ and the coefficients $\lambda_n = 1, -5/8, \ldots$ are tabulated in [57]. In Fig. 2.8, the first-order of the series in (2.51) (dots), i.e. when $n = 0$, is validated for several values of k_m, z/λ and a. As already proven in [58] for the two-dimensional free-space on-plane Green's function, one can select observation points on a regular spatial grid $\rho_n = (n + 1/4)\pi/k_{mr}$ s.t. we cancel out the first term of (2.51) and therefore accelerate the numerical convergence of the error by one inverse power. In Fig. 2.9, we have plotted the first and second orders (dots), i.e. when $n = 0$ and $n = 1$, respectively, as well as the numerically-computed errors (solid lines) for the

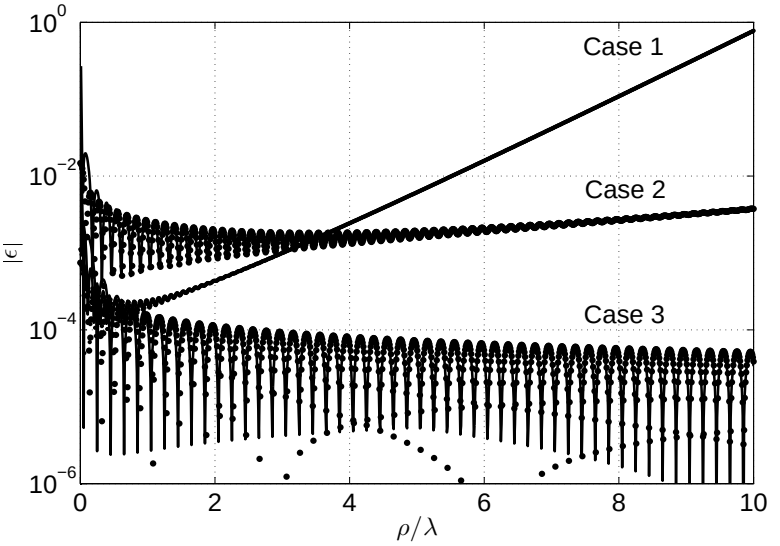

Figure 2.8: Model (dots) and exact value (solid lines) of the truncation error for three different values of a, k_{mr} and z. Case 1: $(a, z, k_{mr}) = (0.05, 0.5, 2.5)$, Case 2 : $(a, z, k_{mr}) = (0.03, , 0.2, 5.5)$ and Case 3 = $(a, z, k_{mr}) = (0.01, 0.2, 3.5)$.

on-plane case. Some observation points have been intentionally placed on the grid in order to validate the second-order term. The model (2.51) has been inverted in Appendix 2.5.8 for a linear contour,

Finally, when the observation point lies onto the reference plane ($z = 0$ and $\rho > 0$) and are selected on the grid $\rho_n = (n + 1/4)\pi/k_{mr}$, the inversion of the second-order term in (2.51) leads to

$$k_{mr} \approx 0.6 \, \frac{e^{2k_{mi}\rho/3}}{\rho \, |\epsilon|^{2/3}} \tag{2.52}$$

The relation (2.52) indicates that the contour should return close the real axis if one wants to lower the truncation limit. This explains why parabolic (2.12) or exponentially decaying contours (2.13) are commonly preferred over SDP (2.11) or linear (2.10) contours for on-plane evaluation. When $k_{mi} = 0$, the truncation limit (2.52) is decreasing w.r.t. ρ and is then maximum for an observation domain at $\rho = \rho_{\min}$. One can a posteriori verify that, for an error $|\epsilon| = 10^{-1}$, the large argument approximation of Bessel

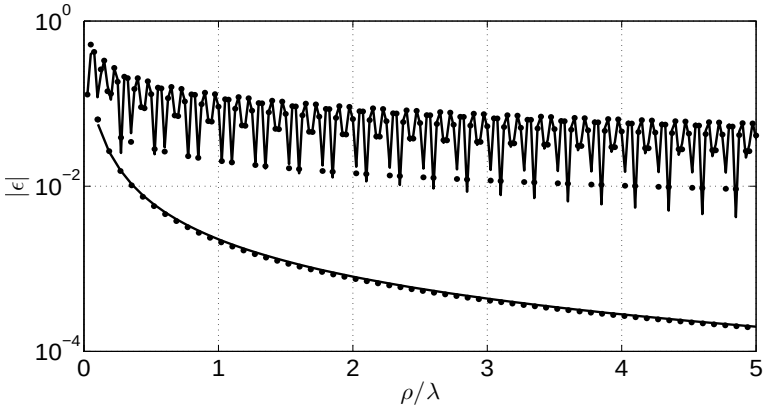

Figure 2.9: First and second order term of (2.51) (dots) and exact value (solid line) of the truncation error for $k_{mr} = 6k$ and $z = 0$.

function used to derive (2.51) is legitimized since $k_{mr}\rho \approx 3$.

2.3.2.2 Discretization error

In [58] and [59], the sampling error resulting from a low contour was observed to be mostly dependent on the distance from the path to the free-space singularity. Hence, discretization is expected to have a similar effect on a linear path selected s.t. ak is equal to the height $k_{\rho i}$ of the exact contour at $k_{\rho r} = k$. This can be verified in Fig. 2.10 and in Fig. 2.11 for distances $z = \lambda$ and $z = 0$, respectively. Indeed, one can observe that the error curves resulting from a parabolic (blue dotted with crosses), a linear (dotted black with circles) and an exponentially-decaying (dotted black with squares) contours are almost superimposed.

For near-field distances z, the sum of the first four replicas in (2.32) evaluated at $z = 0$ provides an accurate model of the error, as confirmed by the agreement of solid lines in Fig. 2.10 and Fig. 2.11. Moreover, it can be proven that those replicas have close amplitude s.t. an estimate of its envelope is given by

$$|\epsilon| \approx 4r \, \frac{e^{-2\pi ka/((1+a^2)\Delta k)}}{2\pi/\Delta k - \rho} \tag{2.53}$$

This expression is plotted (dashed black line) and validated in Fig. 2.10

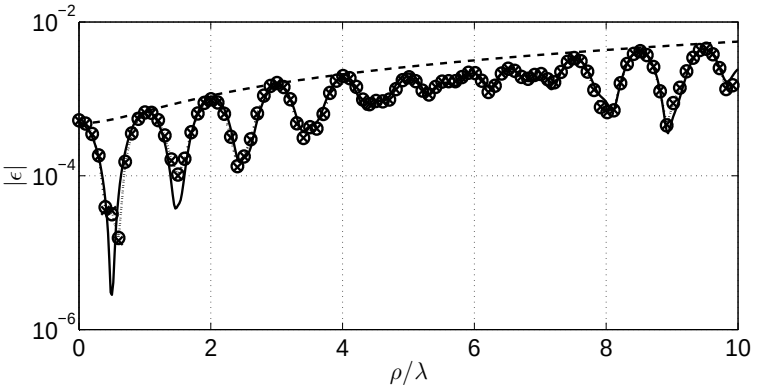

Figure 2.10: Model (2.53) (dashed), first replicas of (2.32) at $z = 0$ (solid) and exact discretization errors using a parabolic (dotted with circles) and a linear contour (dotted with cross) for $z = \lambda$, $\Delta k/k = 0.012$ and $a = 0.01$.

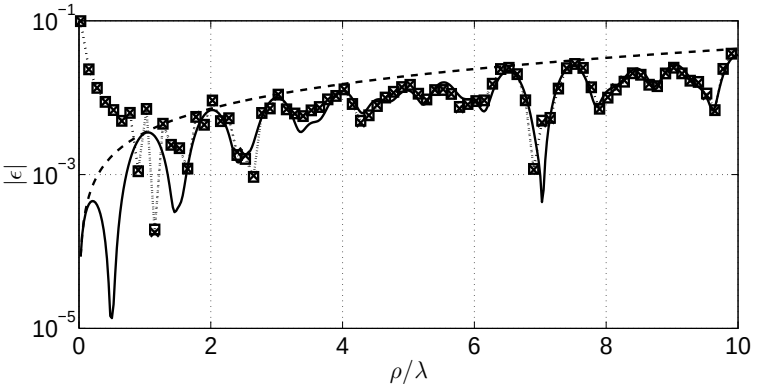

Figure 2.11: Model (2.53) (dashed), first replicas of (2.32) at $z = 0$ (solid) and exact discretization errors using a parabolic (dotted with squares) and an exponentially-decaying contour (dotted with cross) for $z = 0$, $\Delta k/k = 0.02$ and $a = 0.01$.

and Fig. 2.11. One can note that the envelope of complex aliasing error is close to the crests of the exact error and increases progressively on the side of the observation domain. The inaccuracies at lower values of ρ/λ in Fig. 2.11 have been associated to the truncation error. Finally, the model (2.53) has been inverted in Appendix 2.5.9.

2.4 Conclusion

We proposed an integration scheme and sampling rules for the field IPW decomposition for given error level ϵ. For intermediate- to far-field distances, this expansion based on a parametrizable linear contour is well suited to scattering problems in which interacting groups are visible from each other within a limited angular sector. In this case, we derived concise expressions for the contour slope, the truncation limit and the sampling step which are accurate when the field of view ρ/z is smaller than one and the distance z is larger than the wavelength. It was demonstrated that the required number of plane waves follows a similar dependence w.r.t. $k\rho$, kz and ϵ as the number of degrees of freedom (DoF) of the scattered field defined in [22]. At sub-wavelength distances, we have proven that the truncation limit is roughly independent of the contour height and that we can accelerate the convergence rate of the truncation error by selecting observation points on a proper regular grid. The discretization error has also been modelled and inverted assuming an equivalent linear contour.

Generally, the subsequent methodology can be followed for an IPW decomposition

1. A local system of coordinates is defined with its z-axis oriented from the center of the source domain toward the center of the observation domain.

2. The relative distance z between the two domains is evaluated and the maximum radial extend ρ of both domains are summed up.

3. In intermediate- to far- field regions, the contour slope, the truncation

limit and the sampling step are selected with

$$\begin{aligned} a &= \left(1 - \frac{C}{\ln|\epsilon|}\right)^{-1/3} \\ k_{mr} &= \frac{k\rho}{z}\left(\frac{1}{2} + \sqrt{\frac{1}{4} - \frac{\ln|\epsilon|}{aC}}\right) \\ \Delta k &= \frac{2\pi}{(1+a^2)\,\rho}\left(\frac{1}{2} + \sqrt{\frac{1}{4} - \frac{\ln|\epsilon|}{aC}}\right)^{-1} \end{aligned}$$

where $C = k\rho^2/z$ is the near-field parameter and ϵ is the targeted relative error.

4. the field plane-wave spectrum is analytically or numerically computed with (2.17).

5. The electric field is evaluated on the observation domain using (2.16).

The provided sampling rules could also be used to accelerate the evaluation of intermediate fields, from a few wavelengths to a few times the Fraunhofer distance, in fast method-of-moments implementations based on IPWs, such as FIPWA [27] or HIPWA [21], or in the context of the Spectral Theory of Diffraction [62]. In addition, the models could help to evaluate scattered fields within and above layered media [44], [59].

2.5 Appendices

2.5.1 Derivation of steepest descent paths (SDP)

Considering the plane-wave decomposition (2.1) and a surrounding medium of complex-valued wavenumber $k = k_r + jk_i$, the SDP at $x = 0$ corresponds to the contour which keeps the real part of $k_y = k_{yr} + jk_{yi} = (k^2 - k_x^2)^{1/2}$ constant and which passes through the saddle-point at $k_x = 0$. By taking the square of k_y, we can obtain

$$\begin{aligned} k_{yr}k_{yi} &= k_r k_i - k_{xr}k_{xi} \\ k_{yr}^2 - k_{yi}^2 &= k_r^2 - k_i^2 - k_{xr}^2 + k_{xi}^2 \end{aligned} \tag{2.54}$$

For a saddle point at $k_x = 0$, we have $k_{yr} = k$. Substituting the first equation into the second yields

$$k_{xi} = \frac{k_{xr}}{1 + \left(\frac{k_{xr}}{k_r}\right)^2} \left(\frac{k_i}{k_r} + \sqrt{1 + \left(\frac{k_i}{k_r}\right)^2 + \left(\frac{k_{xr}}{k_r}\right)^2} \right) \tag{2.55}$$

For a lossless medium, i.e. $k_i = 0$, this reduces to

$$k_{xi} = \frac{k_{xr}}{\sqrt{1 + \left(\frac{k_{xr}}{k_r}\right)^2}} \tag{2.56}$$

and we have

$$k_y = k - j\frac{k_{xr}^2}{k\sqrt{1 + \left(\frac{k_{xr}}{k}\right)^2}} \tag{2.57}$$

Using the polar coordinates characterized with $k_x = (k_r + jk_i)\sin(\alpha_r + j\alpha_i)$ and $k_y = (k_r + jk_i)\cos(\alpha_r + j\alpha_i)$, we can equalize the imaginary of the exponential in (2.3) with its value at the saddle-point $\alpha = \phi$ to obtain,

$$\cos(\alpha_r - \phi)\cosh\alpha_i + \frac{k_i}{k_r}\sin(\alpha_r - \phi)\sinh\alpha_i = 1 \tag{2.58}$$

This corresponds to the equations presented in [27], [84] and indicates that the SDP for an observation angle ϕ is simply shifted.

2.5.2 Truncation error

With (2.6), (2.24) and (2.23), the truncation error is given by

$$\epsilon = \frac{-jz}{k}\, e^{jk\rho^2/(2z)} \int_{k_m}^{\infty} e^{jk_\rho^2 z/(2k)} J_0(k_\rho\rho) k_\rho \mathrm{d}k_\rho \tag{2.59}$$

Performing a first-order integration by parts leads to

$$\epsilon = -e^{jk\rho^2/(2z) + jk_\rho^2 z/(2k)} J_0(k_\rho\rho) - R \tag{2.60}$$

for which the remainder is

$$R = \rho\, e^{jk\rho^2/(2z)} \int_{k_m}^{\infty} e^{jk_\rho^2 z/(2k)} J_1(k_\rho\rho)\, \mathrm{d}k_\rho \tag{2.61}$$

Let us consider a flat contour with $k_{\rho i} = k_{mi}$. Using the Cauchy-Schwarz inequality and an upper bound on the amplitude of the Bessel function $|J_1(x)| < e^{|x_i|}$, we can write

$$|R| \leq \rho\, e^{k_{mi}\rho} \int_{k_{mr}}^{\infty} e^{-k_{mi}k_{\rho r}z/k}\, \mathrm{d}k_{\rho r} \tag{2.62}$$

for which the integral is analytical,

$$|R| \leq \frac{k\rho}{k_{mi}z}\, e^{-k_{mr}k_{mi}z/k + k_{mi}\rho} \tag{2.63}$$

Anticipating the relation $k_{mr} \sim k\rho/z$ from (2.29), we have

$$|\epsilon| \leq e^{-k_{mr}k_{mi}z/k + k_{mi}\rho}\ (1 + \mathcal{O}(k_{mr}/k_{mi})) \tag{2.64}$$

2.5.3 Discretization error

The series (2.32) converges fast enough to keep only the strongest replica of indices (m, n). When $|\Delta y| \ll z$, we can use (2.24) to obtain

$$\epsilon \approx e^{jk(\rho^2 - (x - m\Delta x)^2 - (y - n\Delta y)^2)/(2z)} \tag{2.65}$$

where $\Delta y = \Delta x = 2\pi/((1 + ja)\Delta k)$ and the magnitude is

$$|\epsilon| = e^{\left(mx - Dm^2 + ny - Dn^2\right)kaD/z} \tag{2.66}$$

with $D = 2\pi/((1 + a^2)\Delta k)$. For a conical field of view of radius ρ, the maximum error is achieved when $(m, n) = \{(1, 0); (0, 1)\}$ and $(x, y) = \{(\rho, 0); (0, \rho)\}$ and is given by

$$-\ln|\epsilon| \approx (D - \rho)\, kaD/z \tag{2.67}$$

2.5.4 Error of the dyadic Green's function

The element ij of the absolute error $\bar{\mathbf{e}}^a$ of the IPW decomposition of the dyadic Green's function $\bar{\mathbf{G}}^d$ is given by

$$\bar{e}^a_{ij} = \bar{G}_{ij} - \bar{G}^d_{ij} = e^a + \frac{1}{k^2}\frac{\partial^2 e^a}{\partial u_i \partial u_j} \tag{2.68}$$

where $(u_1, u_2, u_3) \equiv (x, y, z)$. $e^a = G - G^d$ is the absolute error of the IPW decomposition of the scalar Green's function G^d which can be decomposed as $e^a = e^a_t + e^a_d$ where

$$\begin{aligned} e^a_t &\approx -\frac{e^{-jkz}}{4\pi z}\, e^{jk_m^2 z/(2k)}\, J_0(k_m\rho) \\ e^a_d &\approx \frac{e^{-jkz}}{4\pi z}\, e^{-jk(x-m\Delta x)^2/(2z) - jk(y-n\Delta y)^2/(2z)} \end{aligned} \tag{2.69}$$

In (2.69), e^a_t refers to absolute errors resulting from truncation (Appendix 2.5.2) while e^a_d refers to absolute errors resulting from discretization (Appendix 2.5.3). Considering only a e^{-jkz} dependence w.r.t. z yields $\partial e^a/\partial z \approx -jke^a$. For $i = (1,2)$ and $m = n = 1$, the partial derivatives are expressed as

$$\frac{\partial e^a}{\partial u_i} = \frac{-jk}{z}\,(u_i - \Delta x)\, e^a_d - jk_m \frac{u_i}{\rho}\,\frac{J_1(k_m\rho)}{J_0(k_m\rho)}\, e^a_t \tag{2.70}$$

where division by J_0 has been introduced to let e^a_t appear in the numerator. Using the results $k_m \sim k\rho/z$ obtained in (2.29) and $\Delta x \sim \rho$ from (2.35) leads to $\partial e^a/\partial u_i \sim k\rho/z e^a$.

We can now compare the second term of (2.68) with the first term. Deriving w.r.t. u_1, u_2 multiplies the error level by $k\rho/z$. Hence, e^a is multiplied by $\rho^2/z^2 \ll 1$ given observation in limited fields of view. Thus, the first term of (2.68) dominates. Since that term is simply proportional to the scalar Green's function, the error analysis of the latter is sufficient to analyse the error of the vector field in the already defined field of view.

2.5.5 Round-off error

In practice, each spectral variable in the integrand of (2.4) is rounded by the computer. However, we have experimentally observed that the round-off of k_z in the exponential has a stronger impact for $z \gg \lambda$. Assuming a simple multiplicative noise $1 + n(k_{xr}, k_{yr})$, we can perform a first-order Taylor series expansion of this exponential and use $k_z \approx k$ to obtain

$$e^{-jk_z z(1+n)} \approx (1 - jnkz)\, e^{-jk_z z} \tag{2.71}$$

With the help of (2.23) and (2.24), the relative round-off error can be written as

$$\epsilon \approx \frac{-jz^2}{2\pi}\, e^{jk\rho^2/(2z)} \iint n\, e^{jk_\rho^2 z/(2k)} \\ e^{-jk_x x - jk_y y}\, \frac{k_\rho}{k_{\rho r}}\, \frac{\mathrm{d}k_\rho}{\mathrm{d}k_{\rho r}}\, \mathrm{d}k_{xr}\mathrm{d}k_{yr} \quad (2.72)$$

Using the Cauchy-Schwarz inequality and $|n| \leq 2\epsilon_m$ within (2.72), the round-off error for a linear contour is bounded by

$$|\epsilon| \leq \frac{-j\epsilon_m z^2}{\pi}\,(1+a^2) \iint e^{a(-k_\rho^2 z/k + k_{xr}x + k_{yr}y)}\, \mathrm{d}k_{xr}\mathrm{d}k_{yr} \quad (2.73)$$

where a is the straight contour slope and ϵ_m is the double-precision machine error level. Finally, we have

$$|\epsilon| \leq\ kz\epsilon_m\, \frac{1+a^2}{a}\, e^{ak\rho^2/(4z)} \quad (2.74)$$

2.5.6 Optimal integration scheme

Dividing the truncation limit of (2.29) by the sampling step of (2.35) leads to

$$\frac{k_m}{\Delta k} = \frac{C}{4\pi}\,(1+a^2)\, \left(1 - \frac{2\ln|\epsilon|}{aC} + \sqrt{1 - \frac{4\ln|\epsilon|}{aC}}\right) \quad (2.75)$$

Performing a first-order Taylor approximation of the square root yields

$$\sqrt{\pi P} \sim \frac{C}{2}\,(1+a^2)\, \left(1 - \frac{2\ln|\epsilon|}{aC}\right) \quad (2.76)$$

where P is given in (2.39). When the approximation (2.42) is accurate, i.e. $-C/\ln|\epsilon| \gg 1$, we can write

$$\sqrt{\pi P} \sim \frac{C}{2} + \frac{3C^{1/3}}{2}\,(-\ln|\epsilon|)^{2/3} + C^{-1/3}\,(-\ln|\epsilon|)^{4/3} \quad (2.77)$$

Finally, by dropping the last term, we obtain

$$P \sim \frac{C^2}{4\pi}\left(1 + 3\,(-\ln|\epsilon|)^{2/3}\, C^{-2/3}\right)^2 \quad (2.78)$$

2.5.7 Optimal contour slope

Equalizing the derivative of (2.40) to zero and defining $e = -C/\ln|\epsilon|$ leads to

$$e\,a^3 + a^2 - 1 = 0 \tag{2.79}$$

If $\zeta = (27e^2 - 2 + ((27e^2-2)^2 - 4)^{1/2})/2$, the real positive root is given by

$$a = -\frac{1}{3e} + \frac{\zeta^{1/3}}{3e} + \frac{\zeta^{-1/3}}{3e} \tag{2.80}$$

2.5.8 Inversion of the truncation error in the near-field

Let us approximate the amplitude of the truncation error for a linear contour $k_{mi} = ak_{mr}$ by retaining only the first term of the series in (2.51) and by using $k_{zm} \approx jk_m$ with

$$|\epsilon| = b\,\frac{e^{-k_{mr}(z-a\rho)}}{k_{mr}^n} \tag{2.81}$$

where $b = \sqrt{2/\pi}|\lambda_n|/\rho^n$. We can make the substitution $y = b^{1/n}/(k_{mr}|\epsilon|^{1/n})$ to obtain

$$\frac{n|\epsilon|^{1/n}}{b^{1/n}}\,y\ln y = z - a\rho \tag{2.82}$$

Using another change of variables $w = \ln y$ leads to

$$e^w w = \frac{b^{1/n}(z-a\rho)}{n|\epsilon|^{1/n}} \tag{2.83}$$

A solution of this equation is provided by Lambert's W function [60] and yields

$$k_{mr} = \frac{n}{(z-a\rho)}\,W\left(\frac{b^{1/n}(z-a\rho)}{n|\epsilon|^{1/n}}\right) \tag{2.84}$$

Finally, we have

$$k_{mr} = \frac{a_n}{(z-a\rho)}\,W\left(\frac{z-a\rho}{a_n\rho}\,\left(\sqrt{2}|\lambda_n|/(\sqrt{\pi}|\epsilon|)\right)^{1/a_n}\right) \tag{2.85}$$

where W is Lambert's W function [60], $a_0 = 1/2$ and $a_1 = 3/2$ depending on whether or not the observation points lie close to the nodes of the

Bessel's function. The relation (2.85) imposes $a < z/\rho$ for the integrand to converge toward zero as $k_{\rho r} \to \infty$. Rigorously, given an observation range $\rho \in [0, \rho_{\max}]$ and a targeted error level ϵ, the truncation limit should be selected as the maximum of (2.50) and (2.85).

2.5.9 Inversion of the discretization error in the near-field

Let us start from the approximation (2.53) of the amplitude of the discretization error in the near-field,

$$|\epsilon| = r \, \frac{e^{-2\pi k \Delta k a/(1+a^2)}}{2\pi/\Delta k - \rho} \tag{2.86}$$

This can be easily rewritten as,

$$|\epsilon| = \frac{rka/(1+a^2)\; e^{-ka\rho/(1+a^2)}}{ka/(1+a^2)(2\pi/\Delta k - \rho)\; e^{ka/(1+a^2)(2\pi/\Delta k - \rho)}} \tag{2.87}$$

in which one can note that the denominator has xe^x structure. Hence, this expression can be inverted w.r.t. Δk with the help of Lambert's W function [60] and leads to

$$\Delta k^{-1} = \frac{1}{2\pi a k} \, W\left(\frac{rake^{-ka\rho}}{|\epsilon|}\right) + \frac{\rho}{2\pi} \tag{2.88}$$

where we have assumed a low contour height s.t. $1 + \alpha^2 \approx \alpha$.

Spectral-domain Physical Optics

3

3.1 Introduction

The sampling rules derived in Chapter 2 are now applied to the near-to-intermediate field evaluation of the Physical Optics (PO) radiation integral for planar structures, e.g. walls in urban scattering. Making use of the Green's theorem, the plane-wave spectrum (PWS) of the scattered field can be analytically expressed in terms of the incident one [25], [26]. Hence, the integration is carried out in the spectral domain and the calculation does not require any spatial mesh. The resulting formulation extends the spectral integration proposed in [24] to complex-wavenumber spectra. This method, called Spectral-domain Physical Optics (SPO), will be later considered to perform radio-coverage simulations. The error produced by the PO approximation will be analysed in the next chapter.

In order to assess the accuracy of ray-optical representation and compare it with the SPO, we derive an uniform asymptotic evaluation of the scattered fields from the spectral integral of SPO. This leads to the decomposition of the field into Geometrical Optics (GO), edge-diffracted and corner-diffracted contributions. The mathematical derivations rely on a proven equivalence between the PO field radiated from a polygon and that radiated from a set of properly-chosen sectors for which uniform asymptotic expressions were already developed in [73].

This chapter is organized as follows. In Section 3.2.1, we present the mathematical formulation of SPO. In Section 3.3, we derive the uniform expressions of the PO scattered field in terms of GO, edge- and corner-

diffracted fields. The sampling rules are then applied to the PO evaluation of the field scattered by a planar surface and the results are compared to those produced by the uniform asymptotic expansion in Section 3.4. Finally, conclusions are drawn in Section 3.5.

3.2 Spectral-domain Physical Optics

3.2.1 Mathematical formulation for a PEC plate

Let us consider an incident magnetic field represented by a sum of P_i plane waves,

$$\mathbf{H}^i(\mathbf{r}) = \sum_m^{P^i} \mathbf{H}^i_m \, e^{-j\mathbf{k}^i_m \cdot \mathbf{r}} \tag{3.1}$$

where $\mathbf{H}^i_m$ and $\mathbf{k}^i_m$ are expressed in a local system of coordinates (CS) "s" $(\hat{\mathbf{x}}^s, \hat{\mathbf{y}}^s, \hat{\mathbf{z}}^s)$ centred on the scatterer and oriented toward the observation domain, as illustrated in Fig. 3.1. In PO theory, the current density on a

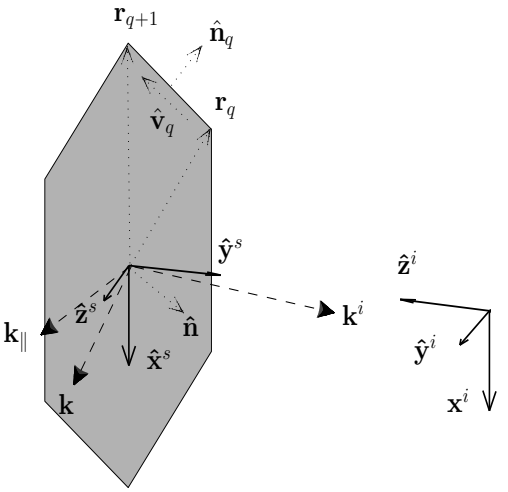

Figure 3.1: Geometrical quantities associated to a polygon.

perfectly-electrical conductor (PEC) object is directly expressed from the

tangential component of the incident magnetic field as $\mathbf{J} = 2\hat{\mathbf{n}} \times \mathbf{H}^i$ with $\hat{\mathbf{n}}$ the unit normal to the surface. This allows us to write

$$\mathbf{J}(\mathbf{r}) = \sum_m 2\ \hat{\mathbf{n}} \times \mathbf{H}^i_m\ e^{-j\mathbf{k}^i_m \cdot \mathbf{r}} \tag{3.2}$$

Then, we can substitute (3.2) into (2.16) and write the PWS of the scattered field as

$$\tilde{\mathbf{H}}^s(\mathbf{k}) = -j\ \mathbf{k} \times \tilde{\mathbf{J}}(\mathbf{k}) \tag{3.3}$$

with the Fourier transform of the induced current given by

$$\tilde{\mathbf{J}}(\mathbf{k}) = 2 \sum_m \left(\hat{\mathbf{n}} \times \mathbf{H}^i_m\right)\ W(\mathbf{k} - \mathbf{k}^i_m) \tag{3.4}$$

The window function W corresponds to the Fourier transform of a complex exponential over the polygonal domain,

$$W(\mathbf{k}) = \iint e^{j\mathbf{k}\cdot\mathbf{r}}\ dS' \tag{3.5}$$

When the surface S' is planar, the integral has an analytical primitive thanks to the Green's theorem. This is derived in Appendix 3.6.1 and may be viewed as an extension of results from [24] to complex wavenumbers. The result reads

$$W(\mathbf{k}) = \frac{1}{jk_\parallel^2} \sum_{q=1}^{Q} L_q\ (\mathbf{k}\cdot\hat{\mathbf{n}}_q)\ \operatorname{sinc}\left(\mathbf{k}\cdot\hat{\mathbf{v}}_q\ \frac{L_q}{2}\right) e^{j\mathbf{k}\cdot(\mathbf{r}_q + L_q\hat{\mathbf{v}}_q/2)} \tag{3.6}$$

where Q is the number of corners of a polygonal scatterer, $\mathbf{r}_q$ is the position vector of the q-th corner, $\hat{\mathbf{v}}_q = (\mathbf{r}_{q+1} - \mathbf{r}_q)/L_q$ is the unit segment direction with $L_q = ||\mathbf{r}_{q+1} - \mathbf{r}_q||$, $\hat{\mathbf{n}}_q = \hat{\mathbf{v}}_q \times \hat{\mathbf{n}}$ is the in-plane outgoing unit normal to the segment, $\mathbf{k}_\parallel = \mathbf{k} - (\hat{\mathbf{n}}\cdot\mathbf{k})\ \hat{\mathbf{n}}$ is the component of the wave-vector parallel to the surface with $k_\parallel^2 = \mathbf{k}_\parallel \cdot \mathbf{k}_\parallel$. Those geometrical quantities are illustrated in Fig. 3.1.

Finally, the scattered magnetic field $\mathbf{H}^s$ is evaluated within the observation domain through (2.19) as

$$\mathbf{H}^s(\mathbf{r}) = \sum_{n=1}^{P^s} w_n\ \tilde{\mathbf{H}}^s(\mathbf{k}_n)\ e^{-j\mathbf{k}_n\cdot\mathbf{r}} \tag{3.7}$$

where w_m is the spectral weight was defined in (2.20). The computational cost of the method is directly related to the computation of the nested sums when we substitute (3.4) into (3.7). If P^i and P^s are the number of plane waves required for the incident and the scattered spectrum, the computational complexity for evaluating the required IPW spectral samples of the scattered field is $\mathcal{O}(P^i P^s)$.

3.2.2 Extension to imperfectly conducting structures

In this section, we discuss how we can compute the fields scattered from a lossy dielectric slab, e.g. a penetrable wall, using the extension of PO presented in [64] and called the Modified Equivalent Current Approximation (MECA). Let us thus consider an arbitrary incident field illuminating a dielectric polyhedron of impedance η_1, of small height and of polygonal cross-section surrounded by free-space, as illustrated in Fig. 3.2.

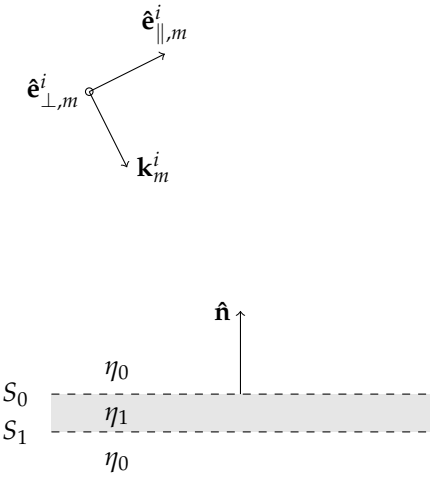

Figure 3.2: Cut view of a dielectric slab of polygonal faces and of impedance η_1 surrounded by free-space.

For each term m of (3.1), we can define unit vectors perpendicular and

parallel to the plane of incidence by

$$\hat{\mathbf{e}}^i_{\perp,m} = \frac{\mathbf{k}^i_m \times \hat{\mathbf{n}}}{\sqrt{k_0^2 - (\mathbf{k}^i_m \cdot \hat{\mathbf{n}})^2}}$$
$$\hat{\mathbf{e}}^i_{\parallel,m} = \frac{\hat{\mathbf{e}}_\perp \times \mathbf{k}^i_m}{k_0} \tag{3.8}$$

where k_0 is the free-space wavenumber and $\hat{\mathbf{n}}$ is the unit normal to the air-dielectric interface S_0, as shown in Fig. 3.2. From there, the polarization $\mathbf{H}^i_m$ of the magnetic field of each incident plane wave m in (3.1) can be decomposed into parallel and perpendicular components s.t. we have

$$\mathbf{H}^i(\mathbf{r}) = \sum_m \left(H^i_{\parallel,m}\, \hat{\mathbf{e}}^i_{\parallel,m} + H^i_{\perp,m}\, \hat{\mathbf{e}}^i_{\perp,m} \right) e^{-j\mathbf{k}^i \cdot \mathbf{r}} \tag{3.9}$$

One can also obtain a similar expression for the incident electric field $\mathbf{E}^i$.

When the surface S_0 is electrically large, the polarizations $\mathbf{H}^t_m$ and $\mathbf{E}^t_m$ of the total fields induced by each incident plane wave m separately can be fairly approximated on the surface S_0 using the Geometrical Optics (GO) theory as follows

$$\mathbf{H}^t_m \approx \mathbf{H}^r_m + \mathbf{H}^i_m$$
$$\mathbf{E}^t_m \approx \mathbf{E}^r_m + \mathbf{E}^i_m \tag{3.10}$$

where $\mathbf{E}^r_m$ and $\mathbf{H}^r_m$ are the polarization of the reflected fields associated to the incident plane wave m computed according the GO laws of reflection. In [64], those vectors have been re-expressed only in terms of $E^i_{\perp,m}$ and $E^i_{\parallel,m}$ with

$$\mathbf{H}^r_m = -E^i_{\parallel,m}\, R_{\parallel,m}\, \hat{\mathbf{e}}^i_{\perp,m}/\eta_0 + R_{\perp,m}\, E^i_{\perp,m}\, \mathbf{k}^r_m \times \hat{\mathbf{e}}^i_{\perp,m}/(\eta_0 k_0)$$
$$\mathbf{E}^r_m = R_{\perp,m}\, E^i_{\perp,m}\, \hat{\mathbf{e}}^i_{\perp,m} + R_{\parallel,m}\, E^i_{\parallel,m}\, \mathbf{k}^r_m \times \hat{\mathbf{e}}^i_{\perp,m}/k_0 \tag{3.11}$$

where η_0 is the free-space impedance, $\mathbf{k}^r_m = \mathbf{k}^i_m - 2\hat{\mathbf{n}}\ (\mathbf{k}^i_m \cdot \hat{\mathbf{n}})$ is the wavevector of the reflected plane wave and $R_{\perp,m}$, $R_{\perp,m}$ are the Fresnel reflection coefficients [65]. The total fields on the surface S_0 are thus approximated by summing the contributions from each incident plane wave,

$$\mathbf{E}^t \approx \sum_m \left(\mathbf{E}^r_m + \mathbf{E}^i_m\right) e^{-j\mathbf{k}^i_m \cdot \mathbf{r}}$$
$$\mathbf{H}^t \approx \sum_m \left(\mathbf{H}^r_m + \mathbf{H}^i_m\right) e^{-j\mathbf{k}^i_m \cdot \mathbf{r}} \tag{3.12}$$

Making use of the equivalence theorem and of (3.12), the authors of [64] have thus expressed the equivalent electric and magnetic currents, i.e. $\mathbf{J} = \hat{\mathbf{n}} \times \mathbf{H}^t$ and $\mathbf{M} = -\hat{\mathbf{n}} \times \mathbf{E}^t$, on the top face of S_0 as

$$\begin{aligned} \mathbf{J}(\mathbf{r}) &\approx \sum_m \hat{\mathbf{n}} \times (\mathbf{H}_m^r + \mathbf{H}_m^i)\, e^{-j\mathbf{k}_m^i \cdot \mathbf{r}} \\ \mathbf{M}(\mathbf{r}) &\approx -\sum_m \hat{\mathbf{n}} \times (\mathbf{E}_m^r + \mathbf{E}_m^i)\, e^{-j\mathbf{k}_m^i \cdot \mathbf{r}} \end{aligned} \tag{3.13}$$

Then, the Fourier transform of the induced currents can be written as

$$\begin{aligned} \tilde{\mathbf{J}}(\mathbf{k}) &= \sum_m \hat{\mathbf{n}} \times (\mathbf{H}_m^r + \mathbf{H}_m^i)\, W(\mathbf{k} - \mathbf{k}_m^i) \\ \tilde{\mathbf{M}}(\mathbf{k}) &= -\sum_m \hat{\mathbf{n}} \times (\mathbf{E}_m^r + \mathbf{E}_m^i)\, W(\mathbf{k} - \mathbf{k}_m^i) \end{aligned} \tag{3.14}$$

where W is the window function, derived in (3.6), associated to the polygonal interface S_0.

Finally, it could be easily proven from (2.17) that the PWS of the scattered magnetic field in the upper half-plane is given by

$$\tilde{\mathbf{H}}^s(\mathbf{k}) = -j\, \mathbf{k} \times \tilde{\mathbf{J}}(\mathbf{k}) - jk_0\eta_0 \left(\tilde{\mathbf{M}}(\mathbf{k}) - (\tilde{\mathbf{M}}(\mathbf{k}) \cdot \mathbf{k})\, \mathbf{k}/k_0^2 \right)$$

Then, the magnetic field $\mathbf{H}^s$ scattered above the interface S_0 can be evaluated through (3.7).

3.3 Uniform asymptotic evaluation

We now decompose the PO fields scattered from a PEC plate into a GO part, i.e. incident and reflected fields, and a diffracted part which originate either from the edges or the corners of the polygon.

First, let us rewrite (3.6) by expanding the sinc function into complex exponentials and regrouping the terms associated with each corner q,

$$W(\mathbf{k}) = \frac{1}{k_\parallel^2} \sum_{q=1}^{Q} \frac{(\mathbf{k} \cdot \hat{\mathbf{n}}_q)\,(\mathbf{k} \cdot \hat{\mathbf{v}}_{q+1}) - (\mathbf{k} \cdot \hat{\mathbf{n}}_{q+1})\,(\mathbf{k} \cdot \hat{\mathbf{v}}_q)}{(\mathbf{k} \cdot \hat{\mathbf{v}}_q)\,(\mathbf{k} \cdot \hat{\mathbf{v}}_{q+1})}\, e^{j\mathbf{k} \cdot \mathbf{r}_q} \tag{3.15}$$

Then, using the two on-plane orthogonal vectors $\hat{\mathbf{v}}_q$ and $\hat{\mathbf{n}}_q$, the following equalities are obtained using projections,

$$\begin{aligned} \hat{\mathbf{v}}_{q+1} &= (\hat{\mathbf{v}}_{q+1} \cdot \hat{\mathbf{v}}_q)\, \hat{\mathbf{v}}_q + (\hat{\mathbf{v}}_{q+1} \cdot \hat{\mathbf{n}}_q)\, \hat{\mathbf{n}}_q \\ \hat{\mathbf{n}}_{q+1} &= \hat{\mathbf{n}} \times \hat{\mathbf{v}}_{q+1} = (\hat{\mathbf{v}}_{q+1} \cdot \hat{\mathbf{v}}_q)\, \hat{\mathbf{n}}_q - (\hat{\mathbf{v}}_{q+1} \cdot \hat{\mathbf{n}}_q)\, \hat{\mathbf{v}}_q \end{aligned} \tag{3.16}$$

Inserting (3.16) into (3.15) and using $k_{\parallel}^2 = (\mathbf{k}\cdot\hat{\mathbf{v}}_q)^2 + (\mathbf{k}\cdot\hat{\mathbf{n}}_q)^2$ leads to

$$W(\mathbf{k}) = \sum_{q=1}^{Q} \frac{\hat{\mathbf{n}}_q \cdot \hat{\mathbf{v}}_{q+1}}{(\mathbf{k}\cdot\hat{\mathbf{v}}_q)\,(\mathbf{k}\cdot\hat{\mathbf{v}}_{q+1})}\, e^{j\mathbf{k}\cdot\mathbf{r}_q} \tag{3.17}$$

Let us now restart from the plane-wave decomposition of the magnetic field (2.16) with a real-axis integration,

$$\mathbf{H}^s(\mathbf{r}) = \frac{-j}{8\pi^2} \iint \tilde{\mathbf{H}}^s(\mathbf{k})\, \frac{e^{-j\mathbf{k}\cdot\mathbf{r}}}{k_z}\, \mathrm{d}k_{xr}\mathrm{d}k_{yr} \tag{3.18}$$

Assuming a single incident plane wave ($m = 0$), we can now substitute the Fourier transform (3.4) into the PWS (3.3) to obtain

$$\mathbf{H}^s(\mathbf{r}) = \frac{-1}{4\pi^2} \iint \mathbf{k} \times \left(\hat{\mathbf{n}} \times \mathbf{H}_0^i\right)\, W(\mathbf{k} - \mathbf{k}_0^i)\, \frac{e^{-j\mathbf{k}\cdot\mathbf{r}}}{k_z}\, \mathrm{d}k_{xr}\mathrm{d}k_{yr} \tag{3.19}$$

Next, we can insert the relation (3.17) of W to have

$$\mathbf{H}^s(\mathbf{r}) = \frac{1}{4\pi^2} \sum_{q=1}^{Q} \iint \frac{\tilde{\mathbf{F}}(\mathbf{k})\, e^{-j\mathbf{k}\cdot(\mathbf{r}-\mathbf{r}_q)}}{(\mathbf{k}\cdot\hat{\mathbf{v}}_q)\,(\mathbf{k}\cdot\hat{\mathbf{v}}_{q+1})}\, \mathrm{d}k_{xr}\mathrm{d}k_{yr} \tag{3.20}$$

where, for convenience, we used

$$\tilde{\mathbf{F}}(\mathbf{k}) = \left(\hat{\mathbf{n}}_q \cdot \hat{\mathbf{v}}_{q+1}\right)\, \left(\frac{\mathbf{k}}{k_z} \times \left(\hat{\mathbf{n}} \times \mathbf{H}_0^i\right)\right) \tag{3.21}$$

Finally, we rewrite the expression (3.20) as

$$\mathbf{H}^s(\mathbf{r}) = \sum_{q=1}^{Q} \mathbf{H}_q^s(\mathbf{r}) \tag{3.22}$$

where $\mathbf{H}_q^s$ can be viewed as a contribution arising from the corner q of the polygon. Each q-th term will be next evaluated in its own local CS $(\hat{\mathbf{v}}_q, \hat{\mathbf{n}}_q, \hat{\mathbf{n}})$ attached to edge q, centred at $\mathbf{r}_q$ on the corner and with z-axis parallel to the normal. For this particular choice, we have

$$\begin{aligned} \mathbf{k}\cdot\hat{\mathbf{v}}_q &= k_x \\ \hat{\mathbf{n}}_q \cdot \hat{\mathbf{v}}_{q+1} &= -\sin\Phi \\ \mathbf{k}\cdot\hat{\mathbf{v}}_{q+1} &= -\sin\Phi\, k_x + \cos\Phi\, k_y \end{aligned} \tag{3.23}$$

where k_x and k_y are the spectral coordinates in the local CS and Φ the exterior angle between $\hat{\mathbf{v}}_q$ and $\hat{\mathbf{v}}_{q+1}$, as shown in Fig. 3.3. From there, the integrals in (3.20) are developed into

$$\mathbf{H}_q^s(\mathbf{r}) = \frac{-1}{4\pi^2} \iint_{-\infty}^{\infty} \frac{\tilde{\mathbf{F}}(k_x, k_y)\, e^{-j\mathbf{k}\cdot\mathbf{r}}}{(k_x - k_x^i)\,(k_y - k_y^i + a\,(k_x - k_x^i))}\, \mathrm{d}k_x \mathrm{d}k_y \tag{3.24}$$

where $a = -\cot\Phi$ and

$$\tilde{\mathbf{F}}(k_x, k_y) = \epsilon_z H_{0x}^i\, \hat{\mathbf{x}} + \epsilon_z H_{0y}^i\, \hat{\mathbf{y}} - \frac{k_x H_{0x}^i + k_y H_{0y}^i}{k_z}\, \hat{\mathbf{z}} \tag{3.25}$$

One can infer that (3.24) exactly matches the equation (3.19) in [73] of the magnetic PO field radiated from a planar sector. Hence, we conclude that the PO scattering analysis of a polygonal surface is rigorously equivalent to that of a proper set of sectors. This was somehow observed in [66] but not yet rigorously proven.

For the sake of completeness, we will summarize the asymptotic development of the integral (3.24) presented in [73] for a homogeneous incident plane wave. It is based on the observation that four critical points in (3.24) contribute asymptotically to the spectral integral : a two-dimensional pole, a two-dimensional saddle-point and the two combinations of a one-dimensional pole and a one-dimensional saddle-point.

The computation of the residue associated to the two-dimensional pole leads to the GO fields,

$$\begin{aligned}\mathbf{H}^{go}(\mathbf{r}) = &\left(\epsilon_z\, (H_{0x}^i\, \hat{\mathbf{x}} + H_{0y}^i\, \hat{\mathbf{y}}) - H_{0z}^i\, \hat{\mathbf{z}}\right) \\ &e^{-j(k_x^i x + k_y^i y - k_z^i |z|)}\, U^1(\mathbf{r})\, U^2(\mathbf{r})\end{aligned} \tag{3.26}$$

where U^1 and U^2 are step functions which commute at the incident shadow boundary (ISB) and at the reflection shadow boundary (RSB) of both edges of the sector. They will be carefully analysed in Appendix 3.6.2. When $z \geq 0$, the expression (3.26) is a reflected field. When $z < 0$, it is a shadowed field, i.e. the opposite of the incident field.

The first part of the diffracted field, defined by the difference between the scattered $\mathbf{E}^s$ and the GO fields $\mathbf{E}^{go}$ originates from the edges of the sector. Fig. 3.3 illustrates the particular CS $(\hat{\mathbf{v}}_1, \hat{\mathbf{n}}_1, \hat{\mathbf{n}})$ attached to edge 1 and centred on the corner 1. According to [73], the field diffracted from

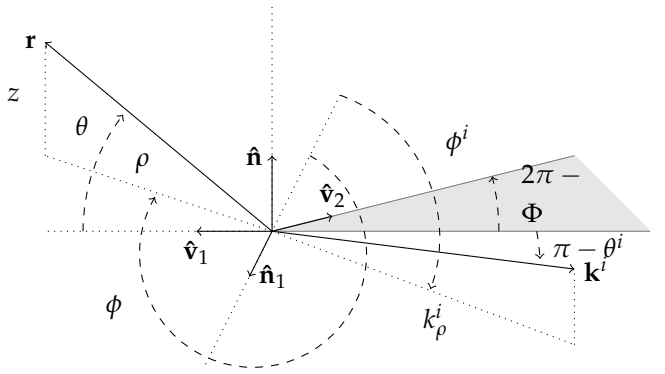

Figure 3.3: Geometry of a sector and related geometrical quantities.

edge 1 is given by

$$\mathbf{H}^e(\mathbf{r}) = \frac{e^{-j\pi/4 - jk_z^i z - jk_\rho^i \rho}}{\sqrt{2\pi k_\rho^i \rho}\,\sin\theta^i}\, F\left(2k_\rho^i \rho a\right)\; U^e(\mathbf{r}) \left(H_{0\perp}^i \cos\theta^i\, \hat{\mathbf{e}}_\parallel + \frac{H_{0\parallel}^i \sin\phi^i\, \hat{\mathbf{e}}_\parallel + \sin\phi\, H_{0\perp}^i\, \hat{\mathbf{e}}_\perp}{\cos\phi + \cos\phi^i} \right) \tag{3.27}$$

where $a = \cos\left((\phi + \epsilon_z \phi^i)/2\right)$, F is the Fresnel's function and U^e is a step function switching at the top diffraction shadow boundary of edge 1 which is detailed in Appendix 3.6.2. The vectors perpendicular and parallel to the direction of propagation are given by $\hat{\mathbf{e}}_\perp = \mathbf{k}^d \times \hat{\mathbf{z}}/k_\rho^i$ and $\hat{\mathbf{e}}_\parallel = \hat{\mathbf{e}}_\perp \times \mathbf{k}^d/k$ and $\hat{\mathbf{e}}_\perp$ with $\mathbf{k}^d = k_\rho^i \cos\phi \hat{\mathbf{x}} + k_\rho^i \sin\phi \hat{\mathbf{y}} + k_z^i \hat{\mathbf{z}}$. The field diffracted from the edge 2 is the counterpart of (3.27) in the local CS $(\hat{\mathbf{v}}_2, \hat{\mathbf{n}}_2, \hat{\mathbf{n}})$.

The second part of the diffracted field emanates from the corner of the sector. The following expression is derived from [73] using an uniform evaluation of the double integral that passes through the two-dimensional saddle-point,

$$\mathbf{H}^c(\mathbf{r}) = \frac{j \sin\Phi\; T(\delta_a, \bar{\delta}_a, \delta_b, \bar{\delta}_b)}{(\cos\theta^{i1} - \cos\theta^1)(\cos\theta^{i2} - \cos\theta^2)}\, \frac{G(R)}{k}\, \hat{\mathbf{r}} \times (\hat{\mathbf{n}} \times \mathbf{H}_0^i) \tag{3.28}$$

where G is the free-space Green's function, R is the distance from the corner to the observation point $\mathbf{r}$, the angles θ^{i1}, ϕ^{i1}, θ^{i2}, ϕ^{i2} are related to edges 1 and 2, as illustrated in Fig. 3.3, and the variables δ_a, $\bar{\delta}_a$, δ_b, $\bar{\delta}_b$ have been defined by (2.90)-(2.99) in [73]. The double transition function T commutes

at the diffraction shadow boundaries of edge 1 and edge 2 to compensate the discontinuity of the edge-diffracted fields. It was shown in [73] that this function accurately reproduces the behavior of fields around the shadow boundaries of the edge-diffracted fields. It is expressed in terms of two generalized Fresnel integrals (GFI) [68] which could be either tabulated or efficiently computed with the algorithm described in [69].

3.4 Numerical results

In the two first following examples, we validate the analytical formula of the field PWS using (3.6) by comparing a spectral-domain integration using the IPW sampling rules with a spatial-domain integration of the PO currents using a Simpson rule and N sample points.

The relative error will be computed numerically through

$$\epsilon(\mathbf{r}) = \left(\frac{\Big(\mathbf{E}(\mathbf{r}) - \mathbf{E}^d(\mathbf{r})\Big) \cdot \Big(\mathbf{E}(\mathbf{r}) - \mathbf{E}^d(\mathbf{r})\Big)^*}{\mathbf{E}(\mathbf{r}) \cdot \mathbf{E}(\mathbf{r})^\star} \right)^{1/2} \tag{3.29}$$

where $\mathbf{E}^d$ is the field reconstructed with SPO and $(^*)$ stands for complex conjugate. In the two first examples, we analyse the total field $\mathbf{E} = \mathbf{E}^s + \mathbf{E}^i$ while, in the last one, it is the scattered field $\mathbf{E}^s$. The computation times are obtained using a PC with 16 GB RAM and Processor Intel (R) Core(TM) i5-3570 CPU @ 3.4 GHz.

According to definition (2.17), the field PWS of a point source is analytically given by

$$\tilde{\mathbf{E}}^{il}(\mathbf{k}^{il}) = -jk\eta \, \left(\hat{\mathbf{p}}^l - (\mathbf{k}^{il} \cdot \hat{\mathbf{p}}^l) \, \mathbf{k}^{il}/k^2 \right) \tag{3.30}$$

where $\hat{\mathbf{p}}^l$ is the polarization of the dipole and the superscript l means that the quantities are expressed in a local CS "i" with $(\hat{\mathbf{x}}^i, \hat{\mathbf{y}}^i, \hat{\mathbf{z}}^i)$ centred on the dipole and oriented toward the center of the scatterer, as illustrated in Fig. 3.1. In contrast, vectors defined in (3.1) were expressed in the CS "s". Hence, we will use a rotation matrix $\mathbf{R}$, as provided in Appendix 3.6.3, in order to transform vectors expressed in CS "i" into vectors expressed in CS "s". This transformation reads as

$$\mathbf{E}^i_m = w^{il}_m \, \mathbf{R} \cdot \tilde{\mathbf{E}}^{il}(\mathbf{k}^{il}_m) \, e^{-j\mathbf{k}^i_m \cdot \mathbf{r}^i} \tag{3.31}$$

where $\mathbf{k}_m^i = \mathbf{R} \cdot \mathbf{k}_m^{il}$, $w_m^{il} = -j(1+ja)^2\Delta k^2/(8\pi^2 k_{zm}^{il})$, a is the slope of the linear contour and the indices (p,q) in (2.19) and in (2.20) have been concatenated into a single index m.

3.4.1 Example 1 : Varying the relative distance

In this example, we consider two parallel plates of length $L = 10\lambda$ separated by a distance d and a point source located at a distance $2L$ from the scatterer, as illustrated in Fig. 3.4. A target error level of $\epsilon_{tar} = 10^{-2}$ has been chosen. The PWS of the incident and scattered fields are evaluated with the help of (2.29), (2.35) and (2.44) in which the triplet $(\rho, z, |\epsilon|)$ is replaced by $(\sqrt{2}L/2, 2L, \epsilon_{tar})$ and $(\sqrt{2}L, d, \epsilon_{tar})$, respectively. The resulting number of plane waves in the IPW decomposition of the incident field is $P^i \approx 200$. The far-field results correspond to a ratio $d/L \geq z_f/L = 40$. In Fig. 3.5, we have plotted the maximum value of the relative error $\epsilon_{max} = \max_{\mathbf{r}} \epsilon(\mathbf{r})$ over the observation domain for a varying distance d.

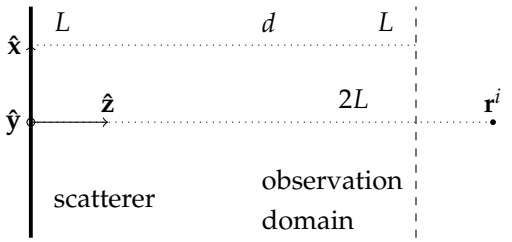

Figure 3.4: Scattering scenario 1: a vertical dipole (dot) illuminates a square plate (solid) of side $L = 10\lambda$. The observation domain lies on a second plate (dashed) separated by a distance d.

As expected, one can observe that $\epsilon_{\max}$ (solid line) is below ϵ_{tar} (dashed line) for distances d satisfying conditions (2.30). More precisely, the error is controlled down to $d \approx 0.3L$. This contributes to validating the paraxial approximation (2.23) used to derive the sampling rules in this thesis. It is worth recalling that the paraxial approximation is not made when estimating the plane-wave spectra. A spatial sampling step of $\lambda/10$ has been empirically chosen for the numerical integration in the spatial domain s.t. the corresponding discretization error is much smaller than ϵ_{tar}. This leads

to $N = 10^4$ spatial samples.

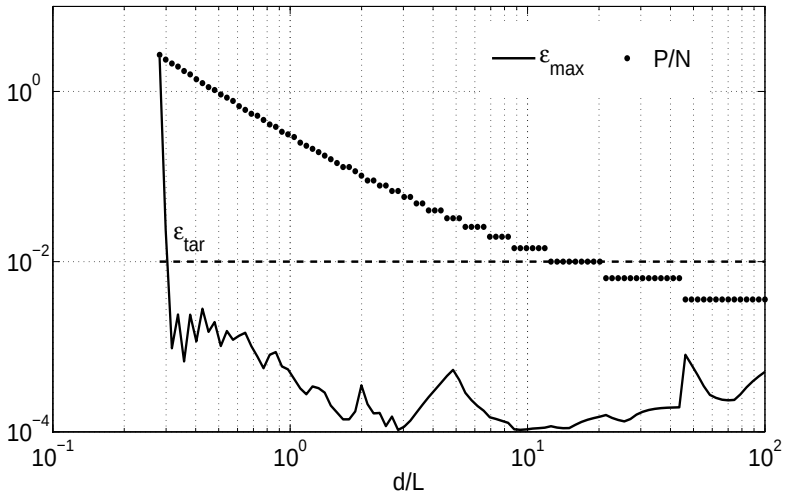

Figure 3.5: Maximum relative error $\epsilon_{\max}$ (solid), target relative error ϵ_{tar} (dashed) and ratio P/N of number of plane waves to number of spatial samples (dotted).

In order to provide a theoretical measure of the acceleration ratio of the spectral method, the ratio P/N is also plotted in Fig. 3.5. The piecewise constant behaviour of this ratio, observed at $d/L \gg 1$, is explained by noting that P/N is an integer and that for a fixed length L and for distances $d \gg L$, the number of plane waves P decays slowly at rate $1/d^2$, according to (2.40). A comparison between the computation times of the spatial-domain and the spectral-domain methods is shown Fig. 3.6. The two integration methods have been coded in Matlab language [112] with low overheads and the same number of "for" loops. One can infer that the speed-up factor becomes important, i.e. between 1 and 2 orders of magnitude, when the field of view $L/(2d)$ is reduced.

3.4.2 Example 2 : Forward scattering

The geometry of the scenario is sketched in Fig. 3.7. The dipole is now located at a distance $3L$ from a plate of length $L = 20\lambda$. The amplitude

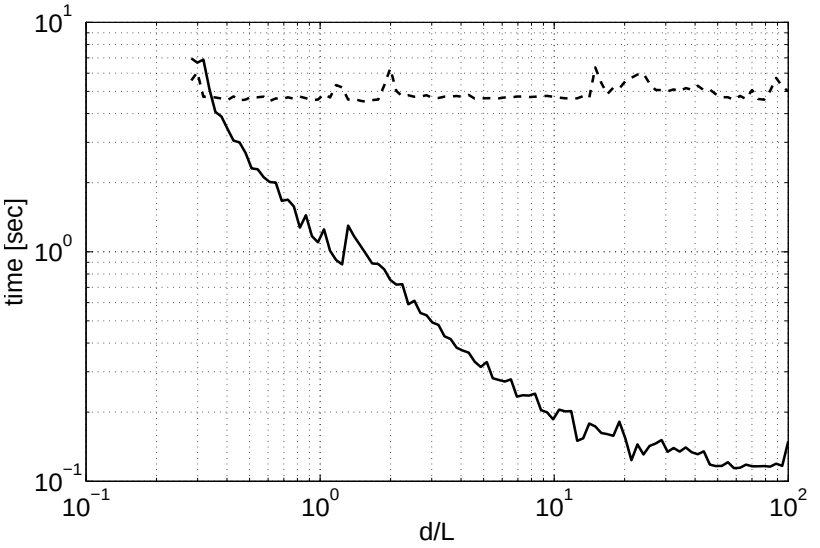

Figure 3.6: Computation times (in sec) of the spatial-domain (dashed) and the spectral-domain (solid) methods.

of the total field is computed within an horizontal square plate of length $2.5L$ contained in the plane $y = 0$ and located at a distance $d = 2.5L$ from the scatterer. A target error of $\epsilon_{tar} = 10^{-3}$ has been selected. This example may be found critical since the observation domain crosses the shadow boundary.

The magnitude of the total electrical field and the relative errors are illustrated in Fig. 3.8 and in Fig. 3.9, respectively. As expected, we observe that the magnitude of the field reaches low values in Fig. 3.8 which correspond to peak values of ϵ in Fig. 3.9. For this scenario, we infer that the relative error of the Green's function is not representative of the relative error of the total field since it does not take into account the possible destructive interference between the incident and scattered fields. Nevertheless, one can notice that those higher values remain in the order of ϵ_{tar} in Fig. 3.9. The PWS of the incident field is sampled with $a = 0.63$, $k_{mr} = 0.3k$, $\Delta k = 0.03k$ and $P^i = 240$. The PWS of the scattered field is sampled with $a = 0.3$, $k_{mr} = 0.95k$, $\Delta k = 0.02k$ and $P = 7300$. The number of spatial samples is $N = 10^4$. Hence, the speed-up factor is less important for this

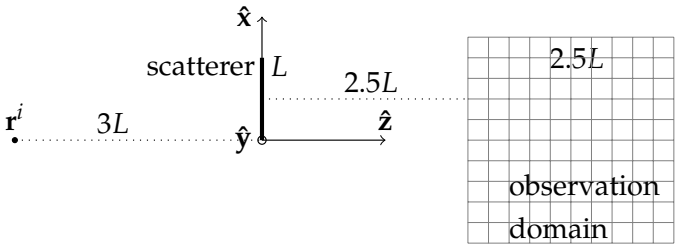

Figure 3.7: Scattering scenario 2: a vertical dipole (dotted) illuminates a square plate (solid) of side $L = 20\lambda$. The observation domain lies on a horizontal second plate (grid).

example since the field of view is still large.

3.4.3 Example 3 : Asymptotic evaluation of PO fields

We now validate the uniform expressions (3.26), (3.27) and (3.28) of the GO field, the edge-diffracted field and the corner-diffracted field, respectively, in the case when a square plate of width 10λ is illuminated at normal incidence ($\theta^i = \pi/2$ and $\phi^i = \pi/2$) by a homogeneous plane wave. As shown in Fig. 3.10, the magnitude back-scattered field is evaluated on a semi-circular path of radius R for an azimuthal angle ϕ ranging from 0 to π and for several elevation angles θ.

The first results in Fig. 3.11 are for $R = 10^4\lambda$ and $\theta = \pi/8$ and $\theta = \pi/4$. At such far-field distances, the edge-diffracted and GO rays are non-zero in a very limited angular range. Hence, the still fine resolution of Fig. 3.11 does not allow us to visualize them. Nevertheless, this example confirms the accuracy of the corner-diffracted field (dots) in the far-field outside the transition regions since it is superimposed with the exact analytical expression (solid).

Next, we consider the same example with an observation path at a near-field distance $R = 20\lambda$ and for angles $\theta = \pi/8$, $\theta = \pi/4$ and $\theta = \pi/2$. Again, one can notice in Fig. 3.12 an excellent agreement between the total asymptotic field (dots), i.e. corner + edges + GO, and the exact value (solid). The GO (circles) and the edge-diffracted fields (dashed-dotted) are now visible. Particularly, we can note the accuracy of the asymptotic solution near the shadow boundaries. The bottom plot of Fig. 3.12 clearly

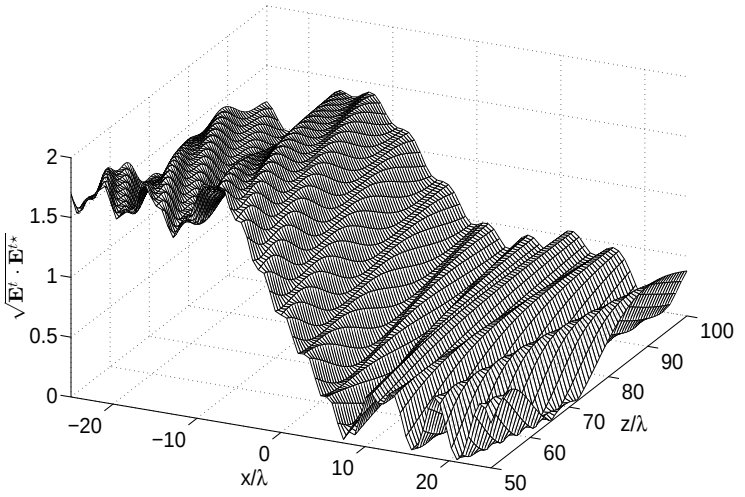

Figure 3.8: Magnitude of the total electrical field, in configuration of Fig. 3.7.

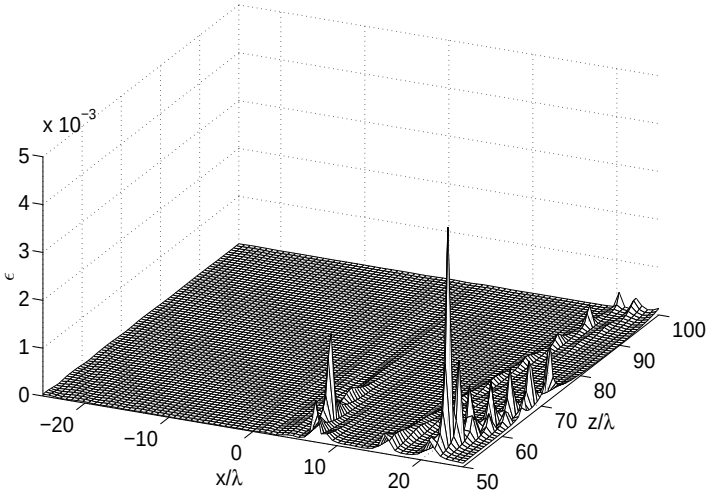

Figure 3.9: Relative error of the IPW decomposition of the total electrical field for $\epsilon_{tar} = 10^{-3}$, in configuration of Fig. 3.7.

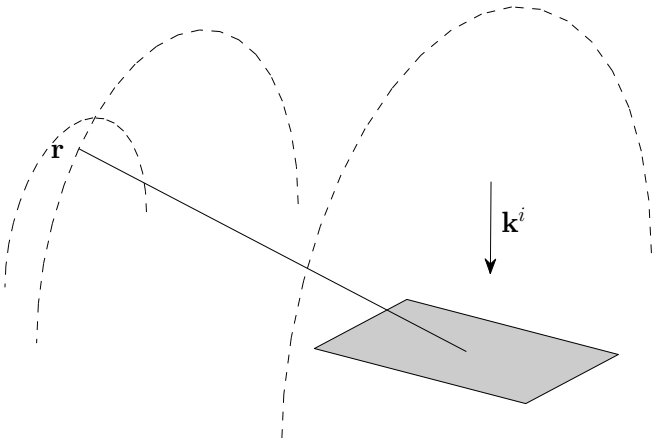

Figure 3.10: Scattering scenario 3: a plane wave illuminates a square plate of side 10λ at normal incidence. The observation path are three semi-circles with elevation $\theta = \{\pi/2, \pi/4, \pi/8\}$.

illustrates the power level of each asymptotic contribution. The difference can be theoretically explained by noting the $(kR)^0$, $(kR)^{-1/2}$ and $(kR)^{-1}$ in the expressions (3.26), (3.27), (3.28) of the GO, edge-diffracted and corner-diffracted fields, respectively, away from the shadow boundaries.

3.5 Conclusion

The integration scheme, derived in Chapter 2, has been applied to accelerate the evaluation of the PO radiation integral in the near-to-intermediate field. By directly expressing the scattered PWS in terms of the incident one, the computations can be entirely performed in the spectral domain. We are thus able to avoid any spatial sampling and associated discretization errors. The method has been called the Spectral-domain Physical Optics (SPO) and will be used later to compute the field scattered by polygonal plates in urban environments. The corresponding computational cost becomes proportional to the product of the degrees of freedom of the incident

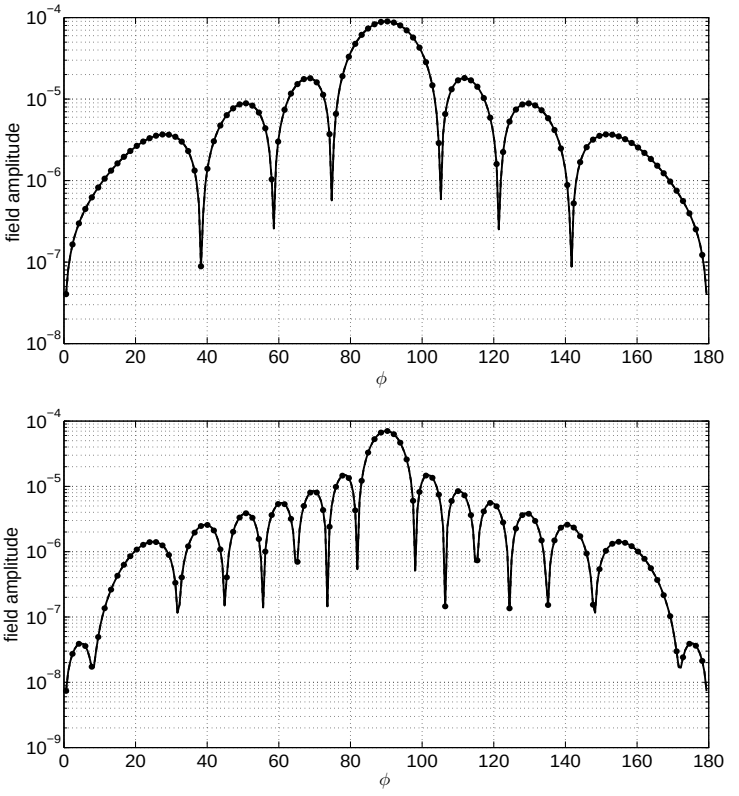

Figure 3.11: Comparison of of the magnitude (in V/m) of the corner-diffracted PO field (3.28) (dots) vs. the exact PO field (solid) on a observation path of radius $R = 10000\lambda$, of elevation angles $\theta = \pi/8$ (top) and $\theta = \pi/4$ (bottom) for a plate of width 10λ at normal incidence.

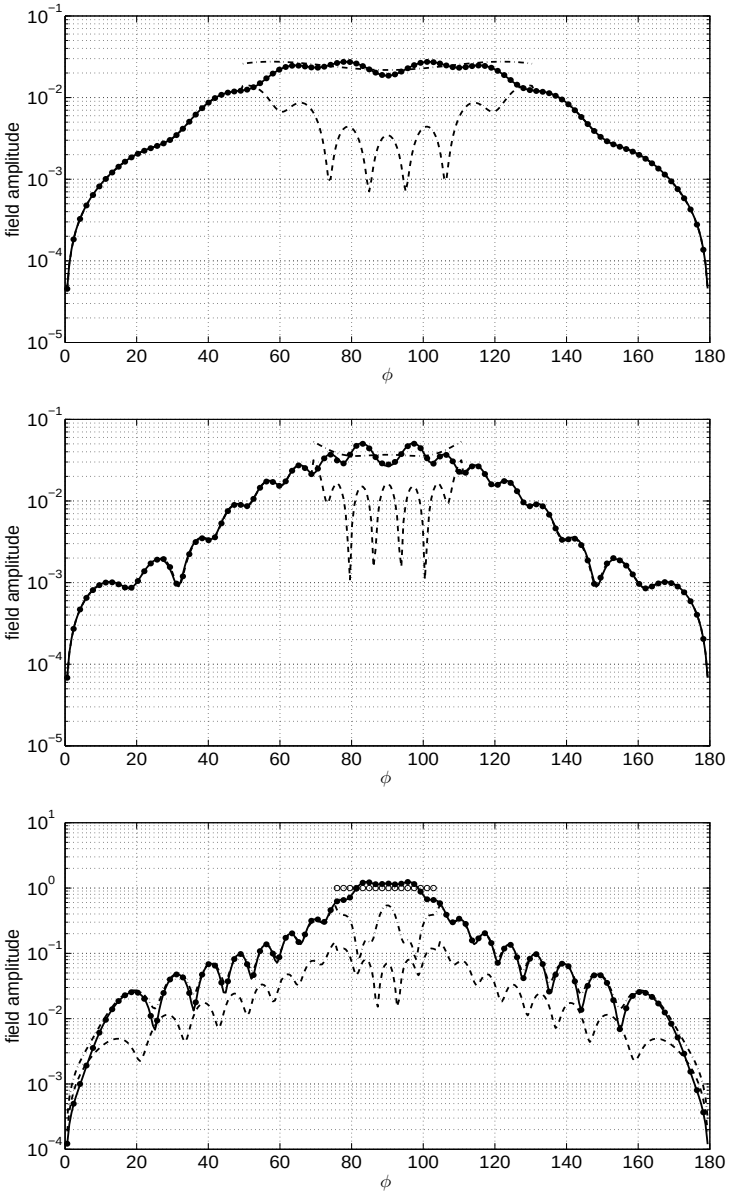

Figure 3.12: Comparison of of the magnitude (in V/m) of the corner-diffracted PO field (3.28) (dashed), the edge-diffracted field (3.27) (dashed-dotted), the GO field (3.26) (circles), their sum (dots) and the exact PO field (solid) on a observation paths of radius $R = 20\lambda$ of elevation angles $\theta = \pi/8$ (top), $\theta = \pi/4$ (center) and $\theta = \pi/2$ (bottom) for a plate of width 10λ at normal incidence.

and of scattered field. In addition, we performed an uniform asymptotic evaluation of the spectral-domain radiation integral using an equivalence between the PO field scattered from a polygon and that by a set of sectors. It was shown that the resulting ray-optical representation which uses GO, edge- and corner-diffracted contributions is highly accurate for a 10λ plate.

3.6 Appendices

3.6.1 Fourier transform over a polygonal domain

We are looking for an analytical expression for the Fourier transform of an exponential over a polygonal domain,

$$W(\mathbf{k}) = \iint e^{j\mathbf{k}\cdot\mathbf{r}} dS' \tag{3.32}$$

In order to reduce the surface integral to a line integral, we will use the divergence theorem. Hence, we need to find a vectorial function $\mathbf{f}$ s.t. $\nabla_s \cdot \mathbf{f} = \nabla \cdot (\mathbf{f} - (\hat{\mathbf{n}} \cdot \mathbf{f})\, \hat{\mathbf{n}}) = e^{j\mathbf{k}\cdot\mathbf{r}}$ where $\nabla\cdot$ is the divergence operator and $\hat{\mathbf{n}}$ is the outgoing normal to the surface. A function satisfying this property is,

$$\mathbf{f} = \frac{\mathbf{k}_\parallel}{jk_\parallel^2}\, e^{j\mathbf{k}\cdot\mathbf{r}} \tag{3.33}$$

where $\mathbf{k}_\parallel = \mathbf{k} - (\hat{\mathbf{n}} \cdot \mathbf{k})\hat{\mathbf{n}}$ is the component of the wave-vector parallel to the surface and $k_\parallel^2 = \mathbf{k}_\parallel \cdot \mathbf{k}_\parallel$. Using the surface divergence theorem, we can rewrite it as a line integral over the boundary of the polygon,

$$W(\mathbf{k}) = \frac{1}{jk_\parallel^2} \int \mathbf{k}_\parallel \cdot \hat{\mathbf{n}}_o\, e^{j\mathbf{k}\cdot\mathbf{r}} d\Gamma \tag{3.34}$$

where Γ is the boundary of the planar domain and $\mathbf{n}_o$ is the unit outgoing normal to the segment. Since we are considering a polygonal shaped surface, we can integrate over each boundary segment separately, which yields

$$W(\mathbf{k}) = \frac{1}{jk_\parallel^2} \sum_{q=1}^{Q} L_q\, (\mathbf{k}\cdot\hat{\mathbf{n}}_q)\ \mathrm{sinc}\left(\mathbf{k}\cdot\hat{\mathbf{v}}_q\, \frac{L_q}{2}\right) e^{j\mathbf{k}\cdot(\mathbf{r}_q + L_q\hat{\mathbf{v}}_q/2)} \tag{3.35}$$

where Q is the number of corners, $\mathbf{r}_q$ is the position vector of the q-th corner, $\hat{\mathbf{v}}_q = (\mathbf{r}_{q+1} - \mathbf{r}_q)/L_q$ is the unit segment direction with $L_q = ||\mathbf{r}_{q+1} - \mathbf{r}_q||$, $\hat{\mathbf{n}}_q = \hat{\mathbf{v}}_q \times \hat{\mathbf{n}}$ is the in-plane outgoing unit normal to the segment. Those quantities are illustrated in Fig. 3.1.

3.6.2 Sign and sense of the step functions

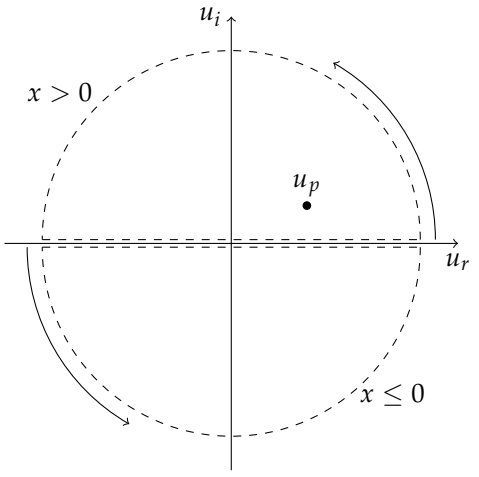

Figure 3.13: Contour deformation used to evaluate the integral (3.36).

We discuss the step functions appearing in (3.26), (3.27) which translate the discontinuities of the GO and edge-diffracted fields. In the development of [73], those functions result from the following integral,

$$f(x) = 2\pi j \int_{-\infty}^{\infty} \frac{e^{jxu}}{u - u_p} \mathrm{d}u \tag{3.36}$$

As illustrated in Fig. 3.13, this integral is evaluated thanks to the Cauchy theorem using a half-circle contour of infinite radius lying either in the positive part of the imaginary domain when $x > 0$ or in the negative part when $x < 0$. If the pole u_p is enclosed by the upper or the lower contour, the value of f is, respectively, $+1$ or -1. Otherwise, it is zero. When the pole lies onto the real axis, e.g. for an homogeneous incident plane wave [73], there is an ambiguity regarding the sign and the sense of the step function since it is not clear whether the pole belongs to the upper

or the lower contour. For a closed polygon, it is necessary to resolve this uncertainty since the fields created outside the shadow boundaries of the polygon by an isolated sector must be properly compensated by the other sectors. This can be done by adding an infinitesimally small imaginary part $\mathbf{k}_i^i$ to the incident wavevector $\mathbf{k}^i$ which is not perpendicular to any of the polygon edges. This leads to

$$\begin{aligned} U^1(\mathbf{r}) &= \operatorname{sign}\left(\sin\Phi\ \hat{\mathbf{k}}_i^i \cdot \hat{\mathbf{v}}_2\right)\ H\left(\operatorname{sign}\left(\sin\Phi\ \hat{\mathbf{k}}_i^i \cdot \hat{\mathbf{v}}_2\right) y_o\right) \\ U^2(\mathbf{r}) &= -\operatorname{sign}\left(\hat{\mathbf{k}}_i^i \cdot \hat{\mathbf{v}}_1\right)\ H\left(-\operatorname{sign}\left(\hat{\mathbf{k}}_i^i \cdot \hat{\mathbf{v}}_1\right)(x_o - a y_o)\right) \end{aligned} \tag{3.37}$$

where H is the Heaviside step function [67], y_o and x_o are defined in [73]. The edge-diffraction shadow boundaries associated to edge 1 and edge 2 are respectively computed with

$$\begin{aligned} U^{e1}(\mathbf{r}) &= -\operatorname{sign}(\hat{\mathbf{k}}_i^i \cdot \hat{\mathbf{v}}_1)\ H(\operatorname{sign}(\hat{\mathbf{k}}_i^i \cdot \hat{\mathbf{v}}_1)\ l_1) \\ U^{e2}(\mathbf{r}) &= \operatorname{sign}(\hat{\mathbf{k}}_i^i \cdot \hat{\mathbf{v}}_2)\ H(\operatorname{sign}(\hat{\mathbf{k}}_i^i \cdot \hat{\mathbf{v}}_2)\ l_2) \end{aligned} \tag{3.38}$$

where l_1 and l_2 are given in [73].

Let us now consider a trivial example, depicted in Fig. 3.14, in which we want to evaluate the reflected and the edge-diffracted fields directly on the surface of a concave pentagon, i.e. for $\phi = \pi$. For the GO field, this is equivalent to the resolution of a point-in-polygon problem [70]. One can observe in Fig. 3.14 that the step functions (3.37) and (3.38) associated to each sector of the polygon recursively interfere with each other to produce, at the end of the process, a two-dimensional step function which is one inside the pentagon (grey domain) and zero outside (white domain). One can also note that the contributions from the edges (dashed lines) are properly compensated outside their lit regions. It is interesting to note that the presented algorithm could be used in a much broader context for solving point-in-polygon problems. This could consist of an elegant winding number algorithm [70] based on a complex-plane analysis of the Fourier transform of a two-dimensional step function representing an arbitrary polygon.

3.6.3 Rotation matrix

Let us first define the local CS "i" $(\hat{\mathbf{x}}^i, \hat{\mathbf{y}}^i, \hat{\mathbf{z}}^i)$ and "s" $(\hat{\mathbf{x}}^s, \hat{\mathbf{y}}^s, \hat{\mathbf{z}}^s)$, in which the IPW decomposition of the incident field and the scattered field are per-

formed, the center positions of a source domain $\mathbf{r}^{so}$, a scatterer $\mathbf{r}^{sc}$ and an observation domain $\mathbf{r}^{o}$. All those vectors are expressed in a global CS $(\hat{\mathbf{x}}, \hat{\mathbf{y}}, \hat{\mathbf{z}})$. The local CS "i" and "s" have their z-axis pointing from $\mathbf{r}^{so}$ to $\mathbf{r}^{sc}$ and from $\mathbf{r}^{sc}$ to $\mathbf{r}^{o}$, respectively. Thus, we have $\hat{\mathbf{z}}^{i} = \mathbf{r}^{sc} - \mathbf{r}^{so}/||\mathbf{r}^{sc} - \mathbf{r}^{so}||$ and $\hat{\mathbf{z}}^{s} = \mathbf{r}^{o} - \mathbf{r}^{sc}/||\mathbf{r}^{o} - \mathbf{r}^{sc}||$. Then, considering two arbitrary vectors $\mathbf{v}^{i}$ and $\mathbf{v}^{s}$, which are, respectively, not parallel to $\hat{\mathbf{z}}^{i}$ and $\hat{\mathbf{z}}^{s}$, we have $\hat{\mathbf{x}}^{i} = \hat{\mathbf{z}}^{i} \times \mathbf{v}^{i}/||\hat{\mathbf{z}}^{i} \times \mathbf{v}^{i}||$ and $\hat{\mathbf{x}}^{s} = \hat{\mathbf{z}}^{s} \times \mathbf{v}^{s}/||\hat{\mathbf{z}}^{s} \times \mathbf{v}^{s}||$. The rotation matrices that transforms vectors expressed in a local CS to vectors in the global CS are,

$$\mathbf{R}^{s,i} = \begin{pmatrix} \hat{\mathbf{x}}^{s,i} \\ \hat{\mathbf{y}}^{s,i} \\ \hat{\mathbf{z}}^{s,i} \end{pmatrix} \tag{3.39}$$

Finally, the rotation matrix for passing from a local CS "i" to a local CS "s" is

$$\mathbf{R} = \mathbf{R}^{s^T}\mathbf{R}^{i} \tag{3.40}$$

where the superscript T means transposition.

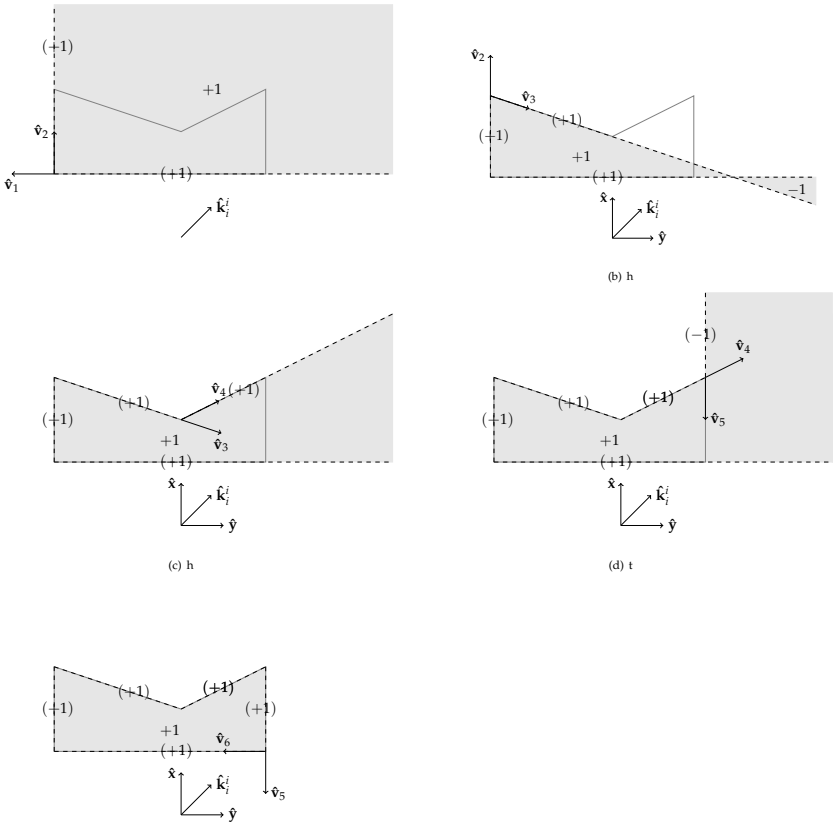

Figure 3.14: Illustration of the interferences between sectors defined by (3.37) and (3.38) to produce the GO and edge-diffracted fields of a concave pentagon. Dashed lines correspond to the diffracting part of the edges and grey domains correspond to the reflecting part of the surface.

On the error of Physical Optics for the scattering analysis of flat surfaces

4

4.1 Introduction

The conventional representation of the total electric field [71] in the CEM literature is

$$\mathbf{E}(\mathbf{r}) = \mathbf{E}^i(\mathbf{r}) + \mathbf{E}^s(\mathbf{r}) \tag{4.1}$$

where $\mathbf{E}^i$ is the incident field radiated by an external source in the absence of the scatterer, i.e. it exists everywhere in space, and $\mathbf{E}^s$ is the scattered field resulting from the radiation of induced current distributions. Besides, in the high-frequency regime, the total field is often decomposed into

$$\mathbf{E}(\mathbf{r}) = \mathbf{E}^i(\mathbf{r})\, U^i(\mathbf{r}) + \mathbf{E}^r(\mathbf{r})\, U^r(\mathbf{r}) + \mathbf{E}^d(\mathbf{r}) \tag{4.2}$$

where $\mathbf{E}^r$ is the reflected field obtained with the Geometrical Optics (GO) theory, $\mathbf{E}^d$ is called the diffracted field, U^i and U^r are step functions which account for the vanishing of $\mathbf{E}^i$ inside the shadow region of the scatterer and of $\mathbf{E}^r$ outside the region of specular reflection. One must note that the diffracted field is inherently discontinuous at the shadow boundaries where the reflected field and the incident field suddenly vanish.

The Physical Optics (PO) theory [72] is based on the approximation of the induced current in the illuminated region of a PEC scatterer from the tangential component of the incident magnetic field $\mathbf{H}^i$,

$$\mathbf{J}^{po}(\mathbf{r}) = 2\ \left(\hat{\mathbf{n}} \times \mathbf{H}^i(\mathbf{r})\right)\ U^i(\mathbf{r}) \tag{4.3}$$

where $\hat{\mathbf{n}}$ is the unit normal to the surface pointing toward the source. The PO omits the irregular part $\mathbf{J}^{fw}$, sometimes called fringe-wave current, of the exact current $\mathbf{J}$,

$$\mathbf{J}(\mathbf{r}) = \mathbf{J}^{po}(\mathbf{r}) + \mathbf{J}^{fw}(\mathbf{r}) \tag{4.4}$$

The fringe-wave current is generally stronger near the discontinuities of the scattering surface, e.g. edges or corners of a polygon. The scattered field can thus also be decomposed into

$$\mathbf{E}^s(\mathbf{r}) = \mathbf{E}^{po}(\mathbf{r}) + \mathbf{E}^{fw}(\mathbf{r}) \tag{4.5}$$

where $\mathbf{E}^{fw}$ originates locally around discontinuities and $\mathbf{E}^{po}$ accounts for a surface effect. The fringe-wave field can be viewed as the error of the PO field w.r.t. the exact scattered field. The estimation of $\mathbf{E}^{fw}$ in the high-frequency (HF) regime is challenging even for simple structures since it requires knowledge of $\mathbf{J}$.

In the HF theories, the asymptotic evaluation of the scattered field leads to a ray-optical representation. Rays are sometimes presented in a simple way as tubes of energy supplemented with a phase information which are launched from the source or which emerge from points on the scattering surface [75]. In fact, a ray can be either a plane, cylindrical, conical or spherical wave, and the expressions of the diffracted field are rigorously derived from asymptotic evaluations of the radiation integral of exact current distributions. The latter are known in closed form for some canonical problems, such as wedges [14], plane sectors [73] and cylinders [74]. As highlighted in the example of Chapter 3, an uniform asymptotic evaluation which includes GO, edge- and corner-diffracted fields is highly accurate when the polygon is electrically large [75]. A more fundamental issue concerns the derivation of general exact solutions for some important canonical problems, such as the plane sector [73], the infinite pyramid [76] or the impedance wedge [78].

In the past century, the Uniform Theory of Diffraction (UTD) [14] provided accurate expressions for the field diffracted by a perfectly-conducting (PEC) wedge. Nowadays, those expressions are widely used in ray-tracing simulations to evaluate the field scattered from a flat surface. The edges of the polygon are thus implicitly assumed to be of infinite extent. This rough approximation leads to a field value which abruptly falls to zero when the diffraction point leaves the edge of the polygon. In addition to predicting null fields, we may expect that the edge-diffracted field is not accurate near its shadow boundaries. In practice, one must thus also include contributions arising from the corners of the polygon. Currently, the exact derivation of corner-diffracted fields is hindered by the lack of a general solution and only approximate expressions have been presented [73], [76], [77].

In this chapter, we analyse the fringe-wave field $\mathbf{E}^{fw}$, i.e. the error resulting from the PO approximation, on flat surfaces. First, we re-derive the solutions of the wedge problem using the spectral-domain methodology presented in Chap 2, in a very similar way to [62], [71]. We then characterize numerically and analytically the fringe-wave $\mathbf{E}^{fw}$ and PO $\mathbf{E}^{po}$ parts of the scattered field $\mathbf{E}^{s}$, as already done in the pioneering work of Ufimtsev [72]. This provides a physical insight later used in the interpretation of the PO results for a PEC plate. In this case, the PO fields are compared with those produced with the Method-of-Moments (MoM) and with a UTD version which uses only edge-diffracted fields.

This chapter is organized as follows. In Section 4.2, we briefly recall the asymptotic high-frequency methods. In Section 4.3, we analyse analytically and numerically the PEC wedge problem. Then, in Section 4.4, we discuss the numerical results of PO for the PEC plate by comparing it to GO, UTD and MoM. Finally, the conclusions are drawn in Section 4.5.

4.2 Overview of high-frequency theories

At high-frequencies, the total field can be accurately approximated with incident, transmitted or reflected and diffracted rays which appears to emanate from few points on the scatterer. The transmitted and reflected fields are calculated with the Geometrical Optics (GO) theory. The GO field is ex-

pected to be accurate when the scattering surface contains enough oscillations around the stationary point, i.e. the point where the phase derivative of the field is null. The diffracted fields, derived in the Geometrical Theory of Diffraction (GTD), can be viewed as corrections of the GO fields to account for edges and corners. The Uniform Theory of Diffraction (UTD) and the Uniform Asymptotic Theory (UAT) are improved versions of GTD which aim to cancel the infinities of the GTD fields.

In Physical Optics (PO), the induced currents are approximated from the GO reflected fields on the scatterer. To obtain the scattered fields, one must compute the radiation integral either numerically, analytically or asymptotically. In the Physical Theory of Diffraction (PTD), the approximation of the current is refined with a non-uniform term, called the fringe-wave current, whose closed-form expression is derived from a canonical problem. Since the fringe-wave current rapidly decay from the edges, its numerical integration on the surface is impractical. Hence, the radiation integral of those currents has been reduced to a regular line integral over the rim of the surface which leads to Equivalent Edge Currents (EEC) [79], Incremental Length Diffraction Coefficients (ILDC) [80] or Elementary Edge Waves (EEW) [72].

Main	GO	PO
Correction	GTD/UTD	PTD

Table 4.1: Summary of HF theories.

The high-frequency theories are summarized in Table 4.1. It is well known [72], [73] that the GTD diffracted fields can be derived from an asymptotic evaluation of the PO+PTD radiation integral. Hence, it often admitted that PO, used alone, is less accurate than GTD. However, the numerical calculation of the scattered field from a radiation integral has some advantages compared to ray-optical representations : the diffraction is accurately and inherently captured for any incident and observation angles and any incident fields, the scattered field is continuous and finite everywhere and the generalization to multiple successive interactions is trivial.

4.3 Analytical study of the PEC wedge

This section is intended to provide a physical insight [72] into the behaviour of the fringe-wave field $\mathbf{E}^{fw}$ defined in (4.5) as the error resulting from the PO approximation. In particular, an analysis of the wedge problem, for which the exact solution has been known for a long time [81], is carried out. It allows the characterization of the singular current distribution $\mathbf{J}^{fw}$ and the field $\mathbf{E}^{fw}$ radiated from it. In the next mathematical derivations, we follow the spectral-domain procedure described in the conclusions of Chapter 2, which requires the analytical evaluation of the PWS from the current $\mathbf{J}$ and of the scattered field $\mathbf{E}^s$ from its PWS. Finally, an uniform asymptotic evaluation of the PO radiation integral helps to interpret the numerical results at high frequencies. Even though it is a well-known canonical problem, the treatment of the complex incidence case is recent [84] and not widely known.

4.3.1 Statement of the problem

A two-dimensional cut of the geometry is shown at Fig 4.1 ; we will use it later for the scattering analysis of a perfectly conducting wedge illuminated by a plane wave. The structure consists of two semi-infinite planes, denoted by face 1 and face 2, merging with an exterior angle Φ at an edge directed along $\hat{\mathbf{e}}$. For the convenience of further derivations, we will define a cylindrical system of coordinates of basis vectors $(\hat{\boldsymbol{\rho}}, \hat{\boldsymbol{\phi}}, \hat{\mathbf{z}}) = (\cos\phi\ \hat{\mathbf{x}} + \sin\phi\ \hat{\mathbf{y}}, \sin\phi\ \hat{\mathbf{x}} - \cos\phi\ \hat{\mathbf{y}}, \hat{\mathbf{e}})$.

Assuming an observation point $\mathbf{r}$ at coordinates (ρ, ϕ, z), an impinging plane wave of wavevector $\mathbf{k}^i$ can be written in cylindrical coordinates as

$$\mathbf{E}^i(\mathbf{r}) = \mathbf{E}_0^i\ e^{-jk_z^i z + jk_\rho^i \rho\cos(\phi-\phi^i)} \tag{4.6}$$

where $k_z^i = k\cos\theta^i$, $k_\rho^i = k\sin\theta^i$ and $\cos\theta^i = \mathbf{k}^i \cdot \hat{\mathbf{e}}/k$ is the elevation angle w.r.t. the z-axis.

In the following calculations, the plane-wave vector fields will be decomposed in two components with electric fields which are either parallel or perpendicular to the plane of incidence containing $\mathbf{k}$ and $\hat{\mathbf{e}}$. More precisely, the normalized basis vectors associated with this edge-fixed system

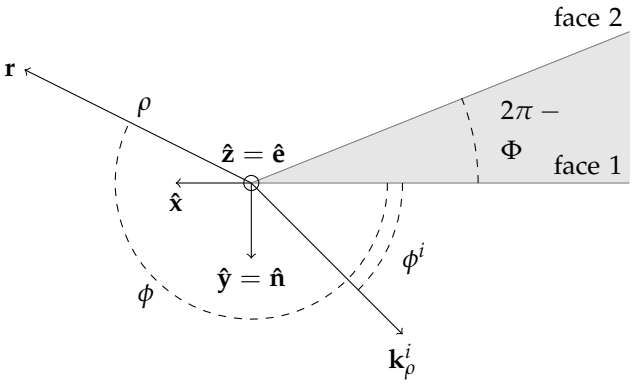

Figure 4.1: Cut view of the wedge geometry with a reference cylindrical CS.

of coordinates are given by

$$\begin{aligned} \hat{\mathbf{e}}_{\perp} &= \mathbf{k} \times \hat{\mathbf{z}}/k_{\rho} \\ \hat{\mathbf{e}}_{\parallel} &= \hat{\mathbf{e}}_{\perp} \times \mathbf{k}/k \end{aligned} \tag{4.7}$$

For instance, the incident electric field is decomposed into

$$\mathbf{E}^i(\mathbf{r}) = \frac{k}{k^i_{\rho}}\, e^{-j\mathbf{k}^i\cdot\mathbf{r}} \left(\eta H^i_{0z}\, \hat{\mathbf{e}}_{\perp} + E^i_{0z}\, \hat{\mathbf{e}}_{\parallel}\right) \tag{4.8}$$

One can clearly infer from (4.8) that only the z-components are necessary to fully describe the vector plane-wave fields. This observation will greatly alleviate the following asymptotic expressions.

4.3.2 Exact expression of the induced current

Considering the cylindrical geometry and results from [84], the z-component of the total electric and magnetic field are sufficient quantities to entirely describe the vector fields,

$$\begin{aligned} E_z(\mathbf{r}) &= E^i_{0z}\, e^{-jk^i_z z} \left(I(\rho,\phi-\phi^i) - I(\rho,\phi+\phi^i)\right) \\ H_z(\mathbf{r}) &= H^i_{0z}\, e^{-jk^i_z z} \left(I(\rho,\phi-\phi^i) + I(\rho,\phi+\phi^i)\right) \end{aligned} \tag{4.9}$$

with

$$I(\rho,\phi) = \Omega \sum_{l=0}^{\infty} \epsilon_l \cos(l\Omega\phi)\, J_{l\Omega}(k^i_{\rho}\rho)\, e^{jl\Omega\pi/2} \tag{4.10}$$

with $\Omega = \pi/\Phi$, $\epsilon_l = \{1, 2, 2, ...\}$ and J_n is the first kind Bessel's function of real order n. From there, the analytical expression of the induced current on both faces of the wedge has been derived in Appendix 4.6.1.

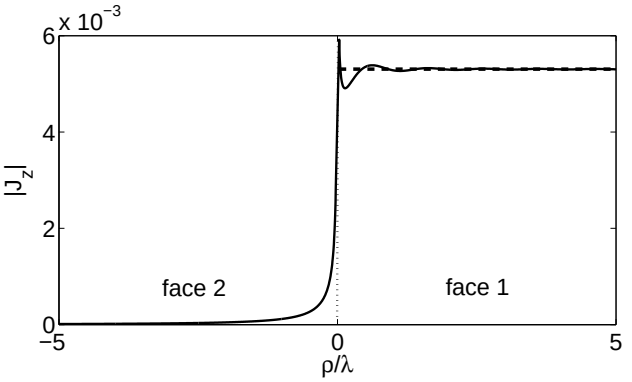

Figure 4.2: Magnitude of the z-component of the exact (solid) and physical optics (dashed) currents for $\Phi = 1.8\pi$, $\phi^i = \pi/2$, $\theta^i = 0$, $E^i_{0z} = 1$, $H^i_{0z} = 1$.

For small radial distances ρ/λ, an asymptotic expression of (4.32) can be obtained by using the small argument approximation of Bessel's functions and by retaining only the lowest power for each polarization. For the current on face 1, this yields

$$\mathbf{J}^1(k\rho, kz) \simeq -2\Omega e^{-jk^i_z z}\Bigg(H^i_{0z}\hat{\boldsymbol{\rho}} + \frac{\Omega\, e^{j\Omega\pi/2}}{j\eta k^i_\rho \Gamma(\Omega+1)} \Big(kE^i_{0z}\sin(\Omega\phi^i) - \eta k^i_z H^i_{0z}\cos(\Omega\phi^i)\Big)\left(\frac{k^i_\rho \rho}{2}\right)^{\Omega-1}\hat{\mathbf{z}}\Bigg) \tag{4.11}$$

where one can note the $\rho^{1-\Omega}$ singularity of the z-component. The exponent $\Omega - 1$ equals zero for a plane ($\Phi = \pi$) and then increases monotonically with Φ until it reaches its maximum value $1/2$ for a half-plane ($\Phi = 2\pi$). This property was interpreted in [82] as a consequence of the abrupt change of direction of the electric field at the edge s.t. it remains perpendicular to both faces. For a large distance ρ/λ, i.e. far away from the edge, it can be demonstrated that the current non-uniformly converges towards the physical optics approximation. This is illustrated in Fig. 4.2 where the amplitude of the z-component of the exact (solid) and physical

optics (dashed) currents are plotted on the two faces assuming an incoming wave propagating perpendicularly to face 1, i.e. $k_z^i = 0$ and $\phi^i = \pi/2$.

4.3.3 Plane-wave spectrum of the scattered field

As discussed in [72], the scattered fields from a three-dimensional wedge illuminated at oblique incidence must exhibit the same z-dependence as that of the incidence field in order to satisfy the boundary conditions,

$$E_z^s(\rho, \phi, z) = E_z'(\rho, \phi)\, e^{-jk_z^i z} \tag{4.12}$$

where E_z' is the solution of a reduced two-dimensional problem in which the incidence is normal $\theta^i = 0$ and k is replaced by k_ρ^i.

In Appendix 4.6.2, the two-dimensional PWS of the scattered field has been analytically evaluated from the following Fourier transforms of the induced currents,

$$\tilde{J}_z^{1,2}(\alpha) = \int_0^\infty J_z^{1,2}(\rho)\, e^{-jk_\rho \rho \cos\alpha}\, \mathrm{d}\rho \tag{4.13}$$

For an incident E-wave, i.e. $H_{0z}^i = 0$, the two-dimensional PWS is given by

$$\begin{aligned}\tilde{E}_z^s(\alpha) &= -jk_\rho^i \eta \left(\tilde{J}_z^1(\alpha) + \tilde{J}_z^2(\alpha)\right) \\ &= -2\Omega \sin(\Omega\pi) E_{0z}^i \left(\left(\cos(\Omega\pi) - \cos\left(\Omega(\alpha + \pi - \phi^i)\right)\right)^{-1} \right. \\ &\qquad \left. - \left(\cos(\Omega\pi) - \cos\left(\Omega(\alpha + \pi + \phi^i)\right)\right)^{-1} \right)\end{aligned} \tag{4.14}$$

One can note that this spectrum is singular when $\alpha = \pm\phi^i$ and $\alpha = 2\Phi - \phi^i$. A similar expression is also provided in Appendix 4.6.5 for an incident H-wave, i.e. $E_{0z}^i = 0$. Using the superposition principle, we can obtain the complex patterns for any incident polarization. The relations (4.14) and (4.38) of Appendix 4.6.5 agree with results of [71]. This thus helps to validate the derivation.

4.3.4 Plane-wave spectrum of the Physical Optics field

The PO ansatz of the induced current in the lit region of a PEC scatterer is obtained with (4.3). Using as similar decomposition as (4.8) for the mag-

netic field $\mathbf{H}^i$, it is possible to re-express the PO current in terms of E_z^i and H_z^i,

$$\mathbf{J}^{po}(\mathbf{r}) = 2\left(-\frac{k}{k_\rho^i}\,\sin\phi^i\,\frac{E_{z0}^i}{\eta}\,\hat{\mathbf{z}} + H_{z0}^i\,\hat{\mathbf{x}} + \cos\phi^i\,\frac{k_z^i}{k_\rho^i}\,H_{z0}^i\,\hat{\mathbf{z}}\right)\,e^{-j\mathbf{k}^i\cdot\mathbf{r}} \quad (4.15)$$

The Fourier transform of this PO current on face 1 has been derived in Appendix 4.6.3 as well as the z-component of the PO plane-wave spectra. This yields

$$\begin{aligned}\tilde{E}_z^{1po}(\alpha) &= \frac{2\sin\phi^i E_{z0}^i}{\cos\alpha - \cos\phi^i} - \frac{2\eta k_z^i H_{z0}^i}{k}\\ \tilde{H}_z^{1po}(\alpha) &= \frac{-2\sin\alpha H_{0z}^i}{\cos\alpha - \cos\phi^i}\end{aligned} \quad (4.16)$$

One can infer that the PO spectrum of face 1 is singular when $\alpha = \pm\phi^i$. When $\phi^i > \Phi - \pi$, face 2 is illuminated and its associated PO spectra are obtained by substituting ϕ^i with $\Phi - \phi^i$ and α with $\Phi - \alpha$ within (4.16) and reversing the sign of the magnetic field spectrum. As mentioned in [72], one can conclude from (4.16) that there is a coupling between the two spectra , i.e. TE_z fields produce TM_z fields and vice versa, when the incidence is oblique, i.e. $k_z^i \neq 0$. This was not the case for the exact spectra (4.14) and (4.38). Hence, this discrepancy results from an artefact of the PO approximation.

4.3.5 Plane-wave spectrum of the fringe-wave field

As stated earlier, the current distributions are singular near the edge and converge toward the physical optics (PO) approximation when moving away from it. Hence, the scattered field can be decomposed [72] into a fringe-wave part $\mathbf{E}^{fw}$, which roughly originates locally around the edge, and a PO part $\mathbf{E}^{po}$, which accounts for a surface effect.

According to (4.5), the PWS of $\mathbf{E}^{fw}$ is given by the difference between that of the exact scattered field (4.14) and that of the PO field (4.16). In the case when only the first face is illuminated $\phi^i < \pi$, we thus have

$$\begin{aligned}\tilde{E}_z^{fw}(\alpha) &= \tilde{E}_z^{s}(\alpha) - \tilde{E}_z^{po1}(\alpha)\\ \tilde{H}_z^{fw}(\alpha) &= \tilde{H}_z^{s}(\alpha) - \tilde{H}_z^{po1}(\alpha)\end{aligned} \quad (4.17)$$

It was mentioned previously that $\tilde{E}^s$ and $\tilde{E}^{po1}$ are both singular at $\alpha = \pm\phi^i$. However, it is proven in [71], [72] by resorting to the limits, that the difference between the PO and the exact spectra is finite at those poles α_p. This remarkable result, which lies in the fundamentals of the Physical Theory of Diffraction (PTD) [72], implies that the spectrum of the fringe-wave field is a regular function. This will also explain why the pattern of the fringe-wave field is not directive as opposed to those of the PO and exact fields.

4.3.6 Uniform asymptotic evaluation

Using results from Chapter 2, the scattered electric field is obtained by multiplying its PWS with that of the two-dimensional free-space Green's function in polar coordinates (2.3),

$$E_z^s(\rho,\phi,z) = \frac{-j}{4\pi}\, e^{-jk_z^i z} \int_\Gamma E_z^s(\alpha)\, e^{jk_\rho^i \rho\cos(\alpha-\phi)}\, \mathrm{d}\alpha \tag{4.18}$$

where the contour Γ was shown in Fig. 2.1. In order to obtain an insight on the behaviour of the scattered fields, we next develop an analytical asymptotic approximation of this integral.

When $k_\rho^i\rho$ is large, i.e. at normal incidence and/or for radial distances above the wavelength, the spectral integrals (4.18) are accurately approximated with a method which relies on deforming the contour Γ into the SDP in the angular domain, as shown in Fig. 2.1, s.t. it passes through the saddle-point at $\alpha = \phi$ of the exponential in the integrand of (4.18).

According to the Cauchy theorem, one must priorly extract the contribution of the poles at $\alpha_p = \pm\phi^i$ in the spectra of the PO field (4.16) scattered from face 1 lying within the contour Γ-SDP closed at infinity. Those residues correspond to the GO fields. Hence, the asymptotic decomposition of the PO field is

$$E_z^{po1}(\mathbf{r}) = E_z^{dpo1}(\mathbf{r}) + E_z^{go}(\mathbf{r}) \tag{4.19}$$

where superscript d stands for diffracted. It must be noted that this representation stands for the scattered field while (4.2) was referred to the total field. The GO fields are thus given by

$$E_z^{go}(\mathbf{r}) = -E_{z0}^i\, e^{-j(k_x^i x+\epsilon_y k_y^i y+k_z^i z)}\, H\left(\epsilon_z(\pi-\phi)-\phi_r^i\right) \tag{4.20}$$

where $\epsilon_y = \operatorname{sign} y$ accounts for back- or forward- fields w.r.t. face 1, H is the Heaviside step function which commutes either at the reflection shadow boundary (RSB) or at the incident shadow boundary (ISB). Those shadow boundaries are illustrated in Fig. 4.3. When $y > 0$, E^{go} is the reflected field. When $y < 0$, it is the shadowing field, i.e. the opposite of the incident field.

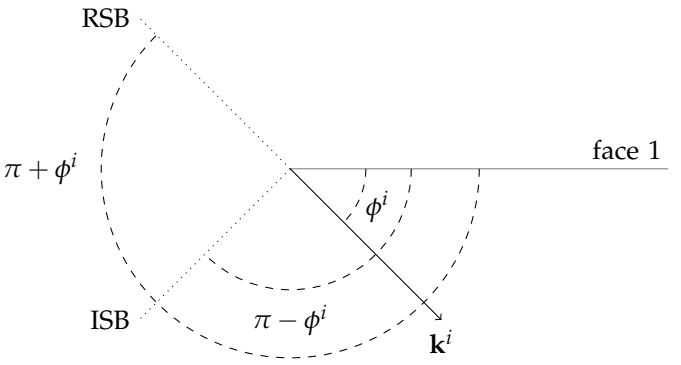

Figure 4.3: Illustration of the incident (ISB) and the reflection (RSB) shadow boundaries.

Next, the PO diffracted field is derived from integrating (4.18) along the SDP contour. We can map the complex-valued coordinate α onto the real axis by performing the following change of variables [72],

$$s = (\sin\theta^i)^{1/2} \cos\left((\alpha - \phi)/2\right) \; e^{-j\pi/4} \tag{4.21}$$

The integral (4.18) is then transformed into

$$E_z^{dpo1}(\mathbf{r}) = \frac{-j}{4\pi} \, e^{-jk_z^i z} \int_{-\infty}^{\infty} \tilde{E}_z^{1po}\left(\alpha(s)\right) \; e^{-k\rho s^2} \; \frac{\mathrm{d}\alpha}{\mathrm{d}s} \, \mathrm{d}s \tag{4.22}$$

The Gaussian function in the integrand recalls the one observed in Chapter 2 for the integration along the SDP in Cartesian coordinates. Otherwise, since the integrand decays rapidly away from the saddle-point at $s = 0$, while the field spectrum remains slowly varying around it, we can approximate the spectrum $\tilde{E}_z^{1po}$ by its value at $s = 0$,

$$E_z^{dpo1}(\mathbf{r}) = \frac{-j}{4\pi} \, e^{-jk_z^i z} \tilde{E}_z^{1po}\left(\alpha(0)\right) \; \frac{\mathrm{d}\alpha}{\mathrm{d}s}(0) \int_{-\infty}^{\infty} e^{-k\rho s^2} \, \mathrm{d}s \tag{4.23}$$

and then analytically evaluate the remaining integral. This corresponds to the well-known saddle-point method and produces the edge-diffracted fields of the Geometrical Theory of Diffraction (GTD) [13]. However, those non-uniform expressions tend toward infinity at the shadow boundaries when the poles located at

$$s_{\pm} = (2\sin\theta^i)^{1/2}\,\cos((\phi \pm \phi^i)/2)\,e^{-j\pi/4} \tag{4.24}$$

gets closer to the saddle point at $s = 0$. This behaviour is problematic and a more sophisticated asymptotic evaluation is required. In the following, we have decided to apply the method presented in [85] to our problem. It starts by regularizing the spectrum $\tilde{E}_z^{1po}$ through

$$T(s) = \tilde{E}_z^{1po}\,(\alpha(s))\;(s - s_-)\,(s - s_+)\,\frac{\mathrm{d}\alpha}{\mathrm{d}s} \tag{4.25}$$

This function is not singular and can thus be expanded into a Taylor series. This allows one to obtain

$$\tilde{E}_z^{1po}(\alpha(s))\,\frac{\mathrm{d}\alpha}{\mathrm{d}s} = \sum_{n=0}^{\infty} \frac{a_n\,s^n}{(s - s_-)\,(s - s_+)} \tag{4.26}$$

where a_n are the coefficients of the Taylor series of T. Substituting (4.26) into (4.22) and swapping sum and integral leads to

$$E_z^{dpo1}(\mathbf{r}) = \frac{-j}{4\pi}\,e^{-jk_z^i z}\,\sum_{n=0}^{\infty} a_n \int_{-\infty}^{\infty} \frac{s^n\,e^{-k\rho s^2}}{(s - s_-)\,(s - s_+)}\,\mathrm{d}s \tag{4.27}$$

The integrals of each term have been analytically evaluated in [85]. The sum was then rewritten in terms of an asymptotic series of $(k\rho)^{-1}$. The first-order term of this series is given in [85] by

$$\begin{aligned} E_z^{dpo1}(\mathbf{r}) = -\frac{e^{-jk_z^i z}}{4j\sqrt{\pi k\rho}} \Bigg(&\frac{T(0)}{s_+ s_-} - \frac{1 - F(k\rho s_+)}{s_+(s_+ - s_-)}\,H(s_+) \\ &- \frac{1 - F(k\rho s_-)}{s_-(s_- - s_+)}\,H(s_-) \Bigg) \end{aligned} \tag{4.28}$$

where $\alpha(0) = \pi - \phi$ and $\mathrm{d}\alpha/\mathrm{d}s(0) = \sqrt{2}\,e^{j\pi/4}/(\sin\theta^i)^{1/2}$. From there, an uniform asymptotic expression of the PO diffracted field can be derived

$$\begin{aligned} E_z^{dpo1}(\mathbf{r}) = -\frac{e^{-j\pi/4 - jk_z^i z - jk_\rho^i \rho}}{\sqrt{8\pi k_\rho^i \rho}} \Bigg(&\tilde{E}_z^{po1}(\pi - \phi) \\ &+ \frac{1 - F(k_\rho^i \rho a^+)}{a_+} - \frac{1 - F(2k_\rho^i \rho a^-)}{a_-} \Bigg) \end{aligned} \tag{4.29}$$

where $a_\pm = \cos\left((\phi \pm \phi^i)/2\right)$ and the Kouyoumjian's transition function generalized to complex arguments [84] is

$$F(z) = 2j\sqrt{z}\, e^{jz} \left(\int_{\sqrt{z}}^{\infty} e^{-jt^2} \mathrm{d}t - e^{-j\pi/4}\, U(\arg\sqrt{z} - \pi/4) \right) \tag{4.30}$$

An expression for the diffracted magnetic field can be obtained following the same procedure and is provided in Appendix 4.6.5.

Away from the shadow boundaries, we roughly have $F \approx 1$ and the HF field (4.29) becomes a cylindrical wave, i.e. with a $(k\rho)^{-1/2}$ decay, whose directivity pattern is $\tilde{E}_z^{po1}(\pi - \phi)$. The same conclusion [72] holds for the asymptotic evaluation of the exact field and of the fringe-wave field. Hence, the comparison between the power levels of $\tilde{E}^{dpo1}$ and of $\tilde{E}^{fw}$ is roughly independent from $k\rho$ and can be made with a simple polar plot.

Near the shadow boundaries, i.e. when $\phi \approx \pi \pm \phi^i$, the field expression (4.29) departs from that of a cylindrical wave since the transition function F varies more rapidly with $k\rho$. At the RSB and ISB, (4.29) is finite since the singular term $\tilde{E}_z^{dpo1}$ is exactly compensated by the two others terms. In addition, the jumps in the transition function F, called Stoke's lines, balance the extinction of incident and reflected fields s.t. the reconstructed scattered field $\mathbf{E}^{po1}$ remains continuous. Neglecting the diffracted field $\mathbf{E}^{dpo1}$ leads roughly to an absolute error of 6 dB at those boundaries since $\mathbf{E}^{dpo1}$ is approximately half of the GO field $\mathbf{E}^{go}$.

It is also interesting to mention that the uniform asymptotic method presented in [85] and used to derive (4.29) remains valid when the incident plane-wave is inhomogeneous, i.e. when the angles ϕ^i and θ^i are complex-valued, provided that the shadow boundaries are rotated w.r.t. their classical locations at $\pi \pm \phi^i$ [84], as detailed in Appendix 4.6.4. This was not possible with the more common formulation of [14] recalled in the expression of the edge-diffracted field in Chapter 3.

Finally, we validate the expression (4.29) when a half-plane is illuminated by an inhomogeneous plane-wave of complex incidence angles $\phi^i = \pi/4 + j0.1$ and $\theta^i = \pi/2 + j0.2$ by a half-plane ($\Phi = 2\pi$) at a distance $\rho = \lambda$. We have decomposed the PO field (solid) into GO (4.20) (dotted) and diffracted (4.29) (dashed) parts in Fig. 4.4. It is important to recall that, since the incident plane wave is inhomogeneous, the incident and reflected fields do not have constant and identical amplitudes and that the RSB and

ISB are rotated by $\delta \approx 5^\circ$ from their initial locations at 135° and 225°, according to the relation (4.46) provided in Appendix 4.6.4. In addition, the diffracted field is inherently discontinuous to compensate for the vanishing GO fields at the shadow boundaries. As expected, one can see that the electric (top) and the magnetic (bottom) PO fields (solid) are continuous and finite at the RSB and ISB.

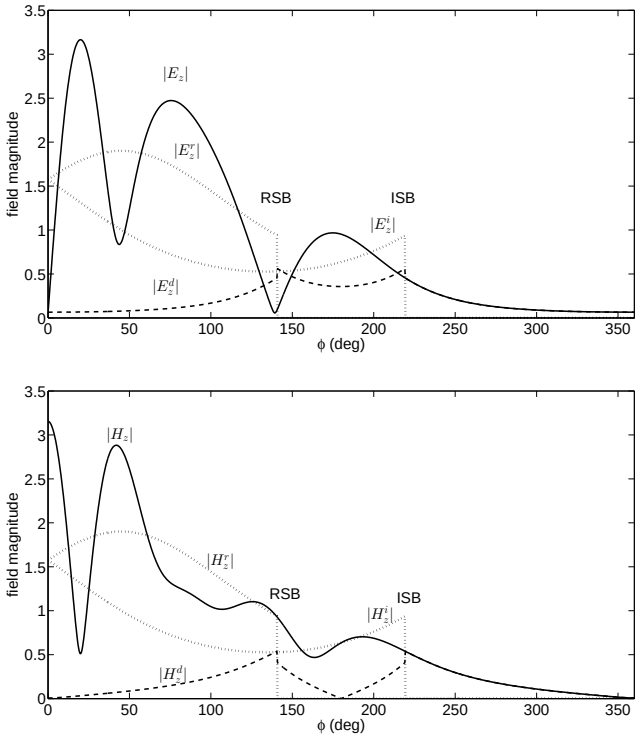

Figure 4.4: Magnitude (in V/m) of z-component of the PO total field (solid), GO fields (dotted) and PO diffracted field (dashed) under complex incidence $\phi^i = \pi/4 + j\,0.1$ and $\theta^i = \pi/2 + j\,0.2$.

4.3.7 Example : fringe-wave vs. PO fields

In this example, we compare the magnitude of the PO and fringe-wave fields when a wedge of exterior angle $\Phi = 7\pi/4$ is illuminated by a plane

wave with $\theta^i = \pi/2$ at normal ($\phi^i = \pi/2$) or grazing ($\phi^i = \pi/10$) incidence. The fields are computed along a circular path of radius $\rho = 5\lambda$ centred on the edge. The results are shown in Fig. 4.5 and Fig. 4.6 with polar plots. The scattered and diffracted electric and magnetic PO fields as well as the fringe wave electric and magnetic fields are, respectively, denoted by E^{po}, H^{po}, E^{dpo}, H^{dpo} and E^{fw}, H^{fw}. The exact diffracted fields E^d, H^d are computed by subtracting the GO fields from the exact scattered fields E^s, H^s.

First, one can see on subfigure (a) that the magnitude of the scattered electric field E_z^s is equal to that of the incident field $E_z^i = 1$ on face 1 and on face 2, i.e. at $\phi = 0^\circ$ and at $\phi = 315^\circ$, respectively, in order to satisfy the PEC boundary conditions. This is not the case for the PO field E_z^{po}. The magnitude of the scattered magnetic field H_z^s is close but not equal to that of the incident field $H_z^i = 1$ on face 1 in the subfigure (b). One can note that the PO field and the scattered one slightly oscillate around 1 in the specular region $\phi \ll \pi - \phi^i$. By comparing subfigures (a) and (b) with (c) and (d), respectively, we conclude that the GO reflected field provides a good approximation and that the diffracted field can be neglected. This conclusion does not hold near the RSB and beyond it where the GO reflected field is null. As one can see in subfigures (c) and (d), the diffracted field is a directive function which is higher near the RSB and the ISB. In contrast, the pattern of the fringe-wave field is rather isotropic. From there, we can say that the fringe fields E_z^{fw}, H_z^{fw} are negligible near the shadow boundaries where the PO diffracted fields E_z^{dpo}, H_z^{dpo} are stronger. In the worst case of normal incidence, the maximum ratio between the level of E_z^{fw}, H_z^{fw} and that of E_z^s, H_z^s is roughly given by 0.1. Those conclusions are expected to hold for any distances from the wedge since the exact, PO and fringe-wave fields are decaying at the same rate.

4.4 Numerical study of the PEC plate

We compare the field back-scattered by a PEC plate computed with Method-of-Moments (MoM) based commercial software, SPO, UTD [15] or GO. In MoM, one tries to directly solve the Maxwell's equations with proper boundary conditions by meshing the surface of the scatterer and by

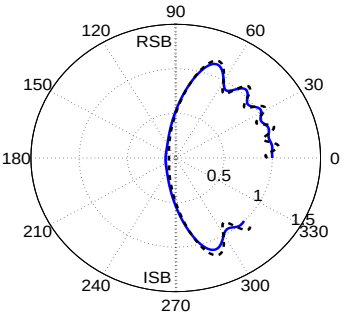

(a) dashed : $|E_z^{po}|$, solid : $|E_z^s|$

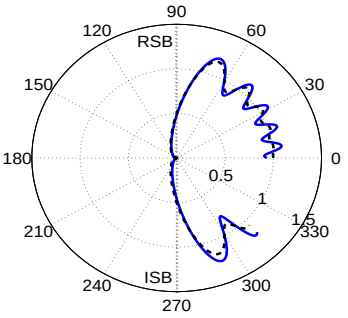

(b) dashed : $|H_z^{po}|$, solid : $|H_z^s|$

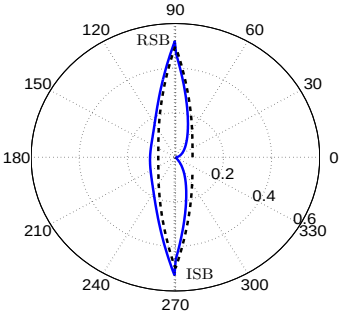

(c) dashed : $|E_z^{dpo}|$, solid : $|E_z^d|$

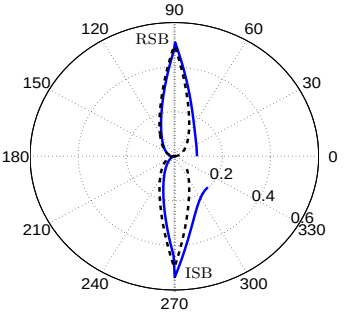

(d) dashed : $|H_z^{dpo}|$, solid : $|H_z^d|$

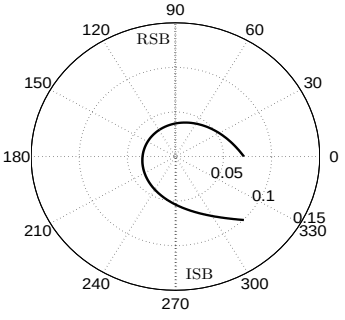

(e) $|E_z^{fw}|$

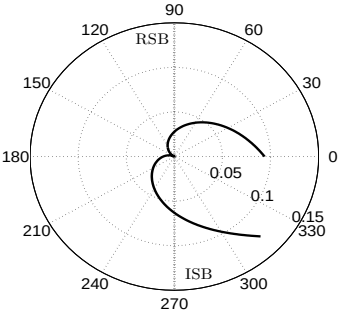

(f) $|H_z^{fw}|$

Figure 4.5: Magnitude (in V/m) of total and diffracted fields for a wedge ($\Phi = 7\pi/4$) illuminated at normal incidence ($\phi^i = \pi/2$).

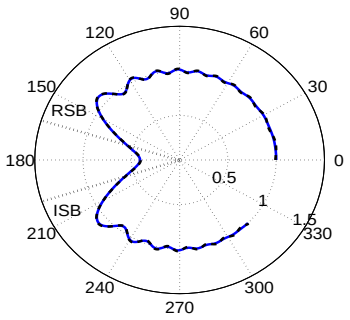

(a) dashed : $|E_z^{po}|$, solid : $|E_z^s|$

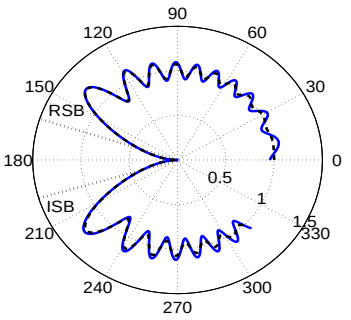

(b) dashed : $|H_z^{po}|$, solid : $|H_z^s|$

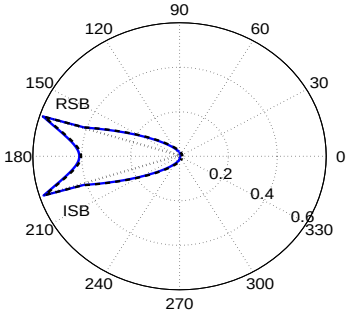

(c) dashed : $|E_z^{dpo}|$, solid : $|E_z^d|$

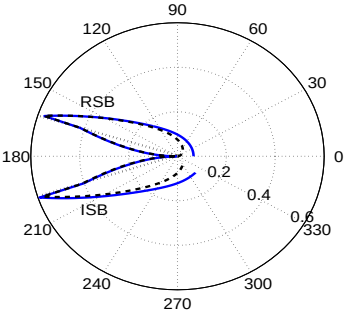

(d) dashed : $|H_z^{dpo}|$, solid : $|H_z^d|$

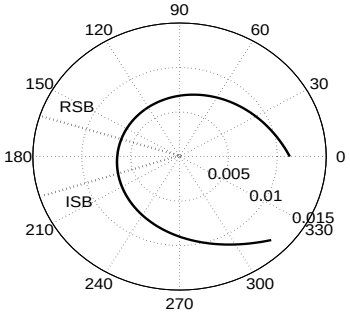

(e) solid : $|E_s^{fw}|$

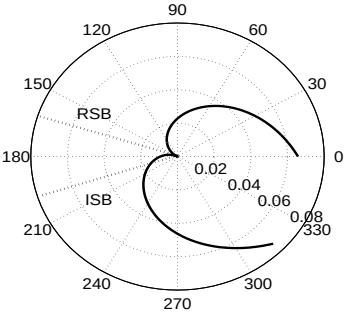

(f) solid : $|H_z^{fw}|$

Figure 4.6: Magnitude (in V/m) of total and diffracted fields for a wedge ($\Phi = 7\pi/4$) illuminated at grazing incidence ($\phi^i = \pi/10$).

decomposing the unknown current distribution in terms of a finite number of basis functions. It requires the numerical inversion of a dense linear system of equations whose unknowns are the coefficients associated to each basis functions. Since MoM is more accurate than HF theories and intrinsically contains all the field contributions, it will serve as a reference. The MoM results have been obtained using RWG basis functions and a minimum mesh size of $\lambda/10$. The UTD only considers the contribution from the edges, as done in most ray-tracing tools. The comparison with GO allows to quantify the magnitude of the diffracted fields. In the following discussions, we will assume that the error of PO w.r.t. MoM is only a consequence of neglecting the singular current term $\mathbf{J}^{fw}$ and that the error of UTD only results from omitting the corner-diffracted field.

In the next examples, we first analyse the angular dependence of the accuracy of near-fields and then, its radial dependence within the specular region.

4.4.1 Example 1 : Near-field scan experiment

Here, we consider the case of a Hertzian electrical dipole placed at $(0, 3\lambda, 3\lambda)$ above a 3.9λ conducting square plate. The back-scattered electrical near-field is computed within circular paths of radius R = 9λ in the E- and H- plane, as illustrated in Fig. 4.7. The MoM results are obtained with the FEKO commercial software [86]. The results have been normalized to the maximum of the MoM field magnitude and are plotted in Fig. 4.8.

First, one can see that the GO reflected field (dots) is null in the E-plane path (bottom plot). In the H-plane, GO overestimates the field magnitude by a factor 2, i.e. 6 dB, near the shadow boundaries around $\theta = 90^\circ$ and $\theta = 150^\circ$. This factor is also predicted in the PEC wedge problem.

Secondly, the PO result is accurate in the specular region of the H-plane path (top plot) where a maximum relative error of $\epsilon = 10^{-1}$ is observed. This also agrees with Fig. 4.5 for the wedge illuminated at normal incidence. The PO field $\mathbf{E}^{po}$ is getting weaker and less accurate when we go away from the RSB and the fringe-wave field $\mathbf{E}^{fw}$ cannot be neglected. However, at low values of θ in the H-plane or over the entire path in the E-plane, the field oscillations seem to be captured by PO. This is explained by the roughly smooth pattern of $\mathbf{E}^{fw}$ shown earlier in Fig. 4.5 and Fig. 4.6.

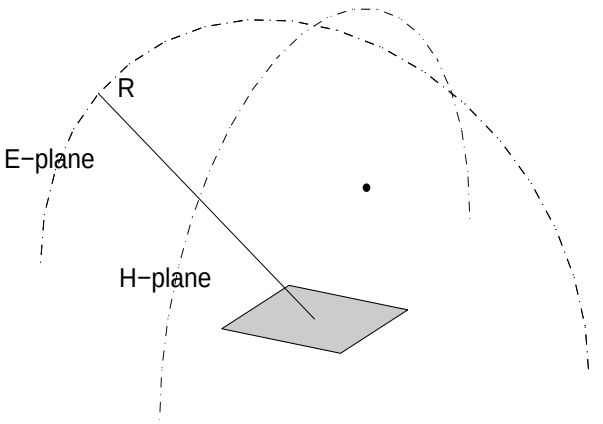

Figure 4.7: Near-field scan experiment above a plate of side 3.9λ with $R = 9\lambda$ and a point source at $(0, 3\lambda, 3\lambda)$.

Finally, UTD is closer to MoM than PO in the H-plane at broadside but underestimates the field magnitude in the specular region by approximately 1 dB. The discontinuities which appear at the shadow boundaries are associated to the sudden vanishing of the diffracted fields originating from the two edges parallel to the H-plane when the diffraction point leaves the plate. In the E-plane, the accuracy of the UTD results degrade even though it seems to capture the mean level of the scattered field. Near the edge shadow boundaries, i.e. at $\theta = 50^\circ$, $\theta = 60^\circ$, $\theta = 120^\circ$ and $\theta = 130^\circ$, the field is overestimated by a factor 2, i.e. 6 dB. We can expect corner-diffracted fields to compensate the vanishing of the edge-diffracted fields with the help of a transition function, similar to used in (3.28) in Chapter 3.

4.4.2 Example 2 : Diffraction as function of distance

In the second example, we evaluate the back-scattered from a plate of side 7λ illuminated by a plane wave at normal incidence. The observation path is a straight line, centred on the plate and perpendicular to it, which starts from a near-field distance $R = 1\lambda$ and ends at the intermediate distance $R = 35\lambda$. The scenario is sketched in Fig. 4.9 and the results are

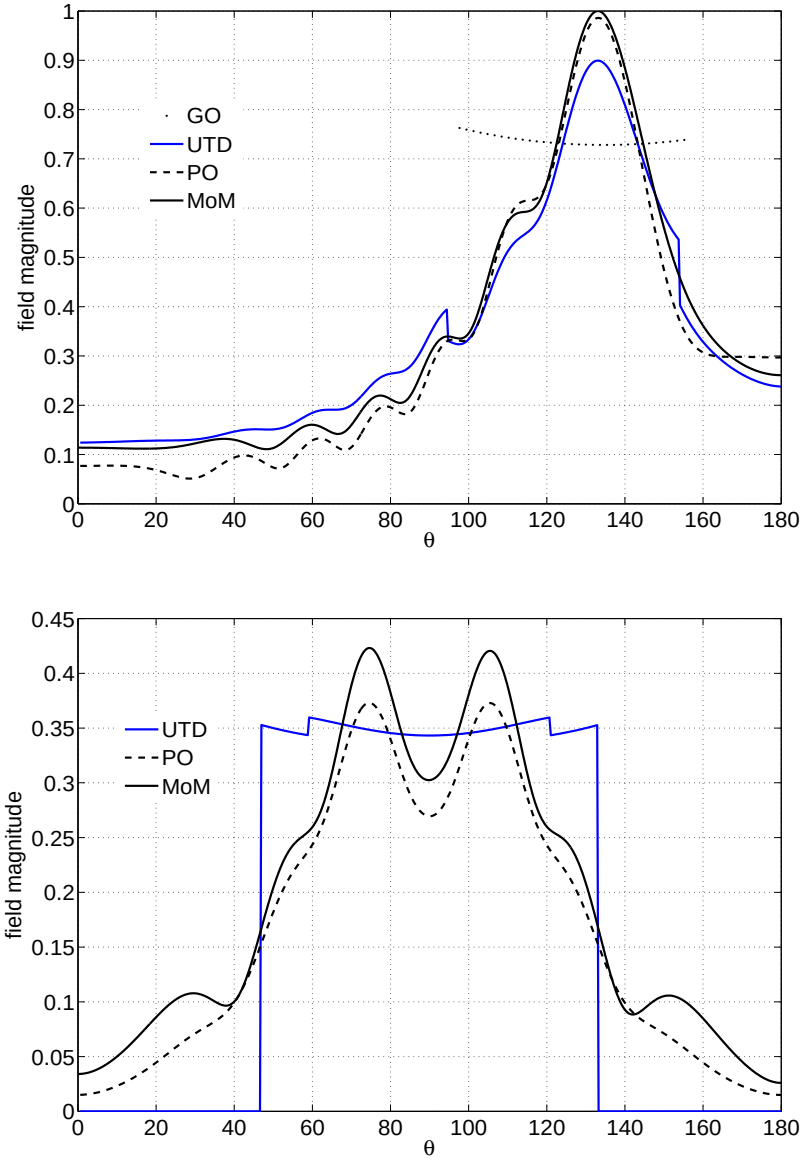

Figure 4.8: Magnitude (in V/m) of the back-scattered electrical field in H-plane (top) and E-plane (bottom) for the scenario depicted in Fig. 4.7.

shown in Fig. 4.10. The MoM curves have been obtained from the IE3D software [87].

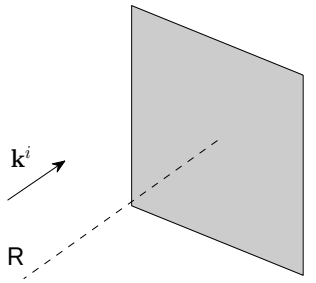

Figure 4.9: A plane-wave illuminating a plate of side 7λ at normal incidence.

Let us start with the analysis of very near-field results, i.e. few λ from the plate. The diffracted field at such small distances is weak since GO is close to MoM. In addition, the PO and GO appears less accurate than the UTD for which the curve is superimposed with that of the MoM.

From $R = 3\lambda$ to $R = 10\lambda$, the UTD and PO solutions agree equivalently well with MoM. Then, in the intermediate-field region, i.e. for distances which starts from the size of the plate $R \approx 7\lambda$, only PO agrees well with MoM. This indicates that the fringe-wave current is negligible. Otherwise, the UTD fails to provide the correct evolution of the field level. This is because the edge-diffracted contributions are cylindrical wave which experiments a $R^{-1/2}$ decay while the magnitude of the scattered field decreases roughly at rate $1/R$. Again, this discrepancy could be corrected by corner-diffracted fields which properly compensate the edge-diffracted fields in intermediate- to far-field regions.

4.5 Conclusion

We analysed both analytically and numerically the error on the scattered field resulting the PO approximation of the induced current. For the PEC wedge, this error, sometimes called the fringe-wave field, originates from singular currents which decreases away from the edge. Those cur-

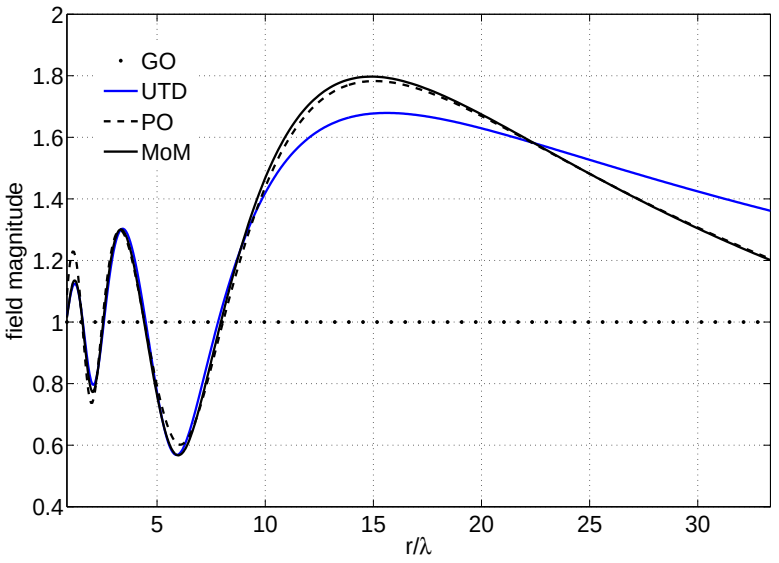

Figure 4.10: Magnitude (in V/m) of the back-scattered electrical field as function of the distance R for the scenario depicted in Fig. 4.9.

rents roughly radiate cylindrical waves with a smooth directivity pattern which can be fairly neglected within the specular region and around the reflection shadow boundary (RSB) where the PO field is stronger. This conclusion was confirmed numerically for the PEC plate by comparison with MoM results. More precisely, we observed a maximum relative error of 10^{-1} near and inside the specular region for the wedge and the plate.

The results could be further improved by adding, to the PO current, a PTD current associated to each edge. In practice, the PTD field can be approximately computed from a line integral along the rim of the plate [79], [80]. The time required to compute this line integral is often considered negligible compared to that required for the two-dimensional PO radiation integral. Another solution could be to derive an analytical expression or an asymptotic approximation of the PWS of the fringe-wave field under inhomogeneous plane-wave incidence, based on the results of [79], and simply add it to the PWS of the PO field, derived in Chapter 3.

The ray-optical representation of scattered fields originates from an

asymptotic evaluation of the exact spectral-domain radiation integrals presented in Chapter 2. If the contributions from the corners and the edges are taken in account, the accuracy of the field representation increases with the electrical size of the plate. However, in most current ray-tracing tools, those contributions are often neglected in the computation of single or multiple interactions due to their complex formulation and the increasing computational cost of tracking those rays within the geometry. Omitting the edge-diffracted or the corner-diffracted leads to an error of roughly 6 dB near the shadow boundaries whatever the frequency. In addition, the uniform edge-diffracted field of UTD used alone fails to provide the $1/R$ decay of the scattered fields from distances above the plate size.

This motivates us to develop a simulation tool based on a direct evaluation of the radiation integral of the Spectral-domain Physical Optics (SPO) developed in Chapter 3 using the sampling rules of Chap 2. Although the computational cost will become frequency-dependent, the truncation effect due to the finite dimension of scatterers will be more precisely and simpler represented by a surface radiation integral rather than by considering explicit edge or corner contributions.

4.6 Appendices

4.6.1 Analytical expression of induced current on a wedge

Using (4.9) and [84], the radial component of the magnetic field can be expressed as

$$\begin{aligned} H_\rho(\mathbf{r}) = &\frac{k_z^i H_{0z}^i}{jk_\rho^{i2}}\, e^{-jk_z^i z}\left(\frac{\partial I}{\partial \rho}(\rho, \phi-\phi^i) + \frac{\partial I}{\partial \rho}(\rho, \phi+\phi^i)\right) \\ &- \frac{kE_{0z}^i}{j\eta k_\rho^{i2}\rho}\, e^{-jk_z^i z}\left(\frac{\partial I}{\partial \phi}(\rho, \phi-\phi^i) - \frac{\partial I}{\partial \phi}(\rho, \phi+\phi^i)\right) \end{aligned} \tag{4.31}$$

From there, we can evaluate the tangential components of the total magnetic field (4.9) and (4.31) on both faces and substitute them within the boundary condition $\mathbf{J} = \hat{\mathbf{n}} \times \mathbf{H}$ in order to obtain the induced current dis-

tributions. For face 1 ($\phi = 0$), this leads to

$$\begin{aligned}\mathbf{J}^1(\rho, z) = -2\Omega\, e^{-jk_z^i z} \sum_{l=0}^{\infty} \epsilon_l\, e^{jl\Omega\pi/2} \Bigg(& H_{0z}^i \cos(\Omega l \phi^i)\, J_{\Omega l}(k_\rho^i \rho)\, \hat{\boldsymbol{\rho}} \\ & + \frac{\Omega l}{j\eta k_\rho^{i2} \rho} \left(k E_{0z}^i \sin(\Omega l \phi^i) - \eta k_z^i H_{0z}^i \cos(\Omega l \phi^i) \right) J_{\Omega l}(k_\rho^i \rho)\, \hat{\mathbf{z}} \\ & + \frac{k_z^i H_{0z}^i}{j k_\rho^i} \cos(\Omega l \phi^i)\, J_{\Omega l+1}(k_\rho^i \rho)\, \hat{\mathbf{z}} \Bigg) \end{aligned} \tag{4.32}$$

Using the symmetry of the problem, the current distribution on face 2 ($\phi = \Phi$) can be obtained from (4.32) by replacing ϕ^i with $\Phi - \phi^i$ and by reversing the sign of z-component.

4.6.2 Plane-wave spectrum of the scattered field

The field PWS is expressed in terms of the following one-sided Fourier integrals,

$$\tilde{\mathbf{J}}^{1,2}(\alpha) = \int_0^{\infty} \mathbf{J}^{1,2}(\rho)\, e^{-jk_\rho \rho \cos\alpha} \mathrm{d}\rho \tag{4.33}$$

where the dependence versus z is omitted since the original problem has been reduced to two dimensions. Considering $\pi \leq \Phi \leq 2\pi$ and $-\pi \leq \alpha_r \leq 0$, the following analytical integrals can be derived,

$$\begin{aligned} \int_0^{\infty} J_\nu(k_\rho^i \rho)\, e^{-jk_\rho^i \rho \cos\alpha}\, \mathrm{d}\rho &= \frac{e^{j\Omega(\alpha - \pi/2)}}{k_\rho^i \sin\alpha} \\ \int_0^{\infty} \frac{\nu J_\nu(k_\rho^i \rho)}{\rho}\, e^{-jk_\rho^i \rho \cos\alpha}\, \mathrm{d}\rho &= \frac{e^{j\Omega(|\alpha| - \pi/2)}}{k_\rho^i} \end{aligned} \tag{4.34}$$

where J_ν is the Bessel's function of the first kind, $\alpha = |w(\alpha)|$ and w is a function that wraps α to $[-\pi, \pi]$. Using those relations, the spectrum of the current (4.32) on face 1 is given by

$$\tilde{\mathbf{J}}^1(\alpha) = 2\Omega \sum_{l=0}^{\infty} \epsilon_l\, e^{j\Omega l \alpha} \left(\frac{H_{0z}^i}{k_\rho^i \sin\alpha} \cos(\Omega l \phi^i)\, \hat{\boldsymbol{\rho}} + \frac{E_{0z}^i}{j k_\rho^i \eta} \sin(\Omega l \phi^i)\, \hat{\mathbf{z}} \right) \tag{4.35}$$

As mentioned in [72], the sums in (4.35) are in geometrical progressions and can be evaluated analytically,

$$\tilde{\mathbf{J}}^1(\alpha) = \frac{2\Omega H^i_{0z}}{k^i_\rho \sin\alpha}\left(\frac{1}{1-e^{j\Omega(\alpha+\phi^i)}} - \frac{1}{1-e^{-j\Omega(\alpha-\phi^i)}}\right)\hat{\boldsymbol{\rho}} + \frac{2\Omega E^i_{0z}}{k^i_\rho \eta}\left(\frac{1}{1-e^{j\Omega(\alpha+\phi^i)}} + \frac{1}{1-e^{-j\Omega(\alpha-\phi^i)}} - 1\right)\hat{\mathbf{z}} \tag{4.36}$$

In addition, it can be easily proven that the expression of $\tilde{\mathbf{J}}^2(\alpha)$ can be obtained by reversing the z-component and substituting α with $\alpha + 2\pi$.

Finally, for an incident E-wave, i.e. $H^i_{0z} = 0$, the PWS of the scattered electric field is expressed using (2.17) as

$$\begin{aligned}\tilde{E}^s_z(\alpha) &= -jk^i_\rho \eta \left(\tilde{J}^1_z(\alpha) + \tilde{J}^2_z(\alpha)\right) \\ &= -2\Omega \sin(\Omega\pi) E^i_{0z}\left(\left(\cos(\Omega\pi) - \cos\left(\Omega(\alpha+\pi-\phi^i)\right)\right)^{-1}\right. \\ &\qquad \left. - \left(\cos(\Omega\pi) - \cos\left(\Omega(\alpha+\pi+\phi^i)\right)\right)^{-1}\right)\end{aligned} \tag{4.37}$$

For an incident H-wave, i.e. $E^i_{0z} = 0$, the PWS of the scattered magnetic field is evaluated using (2.17) with

$$\begin{aligned}\tilde{H}^s_z(\alpha) &= jk^i_\rho \left(\sin\alpha \tilde{J}^1_z(\alpha) - \sin(\Phi-\alpha)\tilde{J}^2_z(\alpha)\right) \\ &= -2\Omega \sin(\Omega\pi) H^i_{0z}\left(\left(\cos(\Omega\pi) - \cos\left(\Omega(\alpha+\pi-\phi^i)\right)\right)^{-1}\right. \\ &\qquad \left. + \left(\cos(\Omega\pi) - \cos\left(\Omega(\alpha+\pi+\phi^i)\right)\right)^{-1}\right)\end{aligned} \tag{4.38}$$

4.6.3 Plane-wave spectrum of the Physical Optics field

Let us start from the decomposition of the incident magnetic field into parallel and perpendicular components, similarly to (4.8),

$$\mathbf{H}^i(\mathbf{r}) = \frac{k}{k^i_\rho}\, e^{-j\mathbf{k}^i\cdot\mathbf{r}}\left(\frac{E^i_{0z}}{\eta}\,\hat{\mathbf{e}}_\perp - H^i_{0z}\hat{\mathbf{e}}_\parallel\right) \tag{4.39}$$

Using (4.7), we can find the following relations,

$$\begin{aligned}\hat{\mathbf{y}}\times\hat{\mathbf{e}}_\perp &= -\sin\phi^i\,\hat{\mathbf{z}} \\ \hat{\mathbf{y}}\times\hat{\mathbf{e}}_\parallel &= -\frac{k^i_\rho}{k}\,\hat{\mathbf{x}} - \frac{k^i_z}{k^i_\rho}\cos\phi^i\,\hat{\mathbf{y}}\end{aligned} \tag{4.40}$$

With the help of (4.39), (4.40) and the PO ansatz of the induced current (4.3) with $\hat{\mathbf{n}} = \hat{\mathbf{y}}$, we have

$$\mathbf{J}^{po}(\mathbf{r}) = 2\left(-\frac{k}{k_\rho^i}\,\sin\phi^i\,\frac{E_{z0}^i}{\eta}\,\hat{\mathbf{z}} + H_{z0}^i\,\hat{\mathbf{x}} + \cos\phi^i\,\frac{k_z^i}{k_\rho^i}\,H_{z0}^i\,\hat{\mathbf{z}}\right)\,e^{-j\mathbf{k}^i\cdot\mathbf{r}} \quad (4.41)$$

The two-dimensional PWS is expressed from the Fourier transform of the induced current over face 1. This is written as

$$\tilde{\mathbf{J}}^{po}(\alpha, k_z) = \int_0^\infty e^{-jk_\rho\rho\cos\alpha}\int_{-\infty}^\infty \mathbf{J}^{po}(\rho, z)\,e^{jk_z z}\,\mathrm{d}z\mathrm{d}\rho \quad (4.42)$$

After substituting (4.41) into (4.42), the spatial integrals are evaluated analytically with

$$\tilde{\mathbf{J}}^{po}(\alpha, k_z) = \frac{-4j\pi\delta(k_z - k_z^i)}{\cos\alpha - \cos\phi^i}\left(\frac{H_{z0}^i}{k_\rho^i}\,\hat{\mathbf{x}} + \left(k_z^i\cos\phi^i H_{z0}^i - k\sin\phi^i\frac{E_{z0}^i}{\eta}\right)\frac{\hat{\mathbf{z}}}{k_\rho^{i2}}\right) \quad (4.43)$$

The PWS of the electric field is obtained using (**??**) with

$$\begin{aligned}\tilde{E}_z^{1po}(\alpha) &= -jk\eta\left(\tilde{J}_z\frac{k_\rho^{i2}}{k^2} - \tilde{J}_x k_\rho^i\cos\alpha\frac{k_z^i}{k^2}\right)\\ &= \frac{2\sin\phi^i E_{z0}^i}{\cos\alpha - \cos\phi^i} - \frac{2\eta k_z^i H_{z0}^i}{k}\end{aligned} \quad (4.44)$$

The PWS of the magnetic field is obtained using (**??**) with

$$\begin{aligned}\tilde{H}_z^{1po}(\alpha) &= jk_\rho^i\,\sin\alpha\,\tilde{J}_z^{po}(\alpha)\\ &= \frac{-2\sin\alpha H_{0z}^i}{\cos\alpha - \cos\phi^i}\end{aligned} \quad (4.45)$$

4.6.4 Rotation of the shadow boundaries for an inhomogeneous incident plane wave

According to [84], the GO fields resulting from an inhomogeneous plane wave is given by

$$E_z^{go}(\mathbf{r}) = -E_{z0}^i\,e^{-j(k_x^i x + \epsilon_y k_y^i y + k_z^i z)}\,H\left(\epsilon_z(\pi - \phi) - \phi_r^i - \delta\right)$$

where δ results from a rotation of those shadow boundaries w.r.t. their classical optical location at $\pi \pm \phi_r^i$ [84]. Precisely, it has been proven in [83]

and [84] that the poles leave the closed contour Γ-SDP at $\alpha_r = \phi \pm \delta$ where δ is analytically given by

$$\delta = 2\ \text{atan2}\left(\tan\left(\pi/4 - \psi/2\right), \tanh(\phi_i^i/2)\right) - \pi \tag{4.46}$$

where $k_\rho^i = ksin\theta^i$ and $\psi = \arg(\sin\theta^i)$.

4.6.5 Uniform asymptotic expression of the PO magnetic field

The uniform expression of the PO magnetic field is derived from (4.28) by substituting $\tilde{H}_z^{1po}$ with $\tilde{E}_z^{1po}$ in the definition of the function H (4.25). This leads to

$$\begin{aligned} H_z^{dpo1}(\mathbf{r}) = -\frac{e^{-j\pi/4 - jk_z^i z - jk_\rho^i \rho}}{\sqrt{8\pi k_\rho^i \rho}} \Bigg(& \tilde{H}_z^{dpo1}(\pi - \phi) \\ & - \frac{1 - F\left(2k_\rho^i \rho a_+^2\right)}{a_+} - \frac{1 - F\left(2k_\rho^i \rho a_-^2\right)}{a_-} \Bigg) \end{aligned} \tag{4.47}$$

where $a_\pm = \cos\left((\phi \pm \phi^i)/2\right)$ and F is the Kouyoumjian's transition function given by (4.30).

Simulating urban radio propagation with SPO

5

5.1 Introduction

Decidedly, Physical Optics (PO) is a step forward towards accurate radio channel prediction in large and complex environments. While ray-based methods implementing UTD are widely applied thanks to their intuitiveness and computational efficiency, their ability to accurately represent scattered fields has been questioned in Chapter 4. Currently, it is well known that the higher-order reflections help to capture the canyon effect in narrow streets of a densely built environment [88] and that the diffraction contributions model the extended coverage when the base stations are placed above the rooftops or near the ground level [89].

In many ray-tracing tools, the diffracted field is only taken into account as first or last interaction within the multiple scattering chain. The intermediate interactions of this chain are thus evaluated with Geometrical Optics (GO). In fact, modelling and tracking multiple edge- and corner-diffracted rays is a complicated task [90], [91]. As highlighted in Chapter 4, the GO and edge-diffracted fields fail to provide the correct angular dependence as well as the $1/R$ decay of scattered fields in intermediate- to far-field regions, i.e. roughly for distances R ranging from the size of scatterer. This paves the way to an approach which directly starts from the radiation integral rather than from its asymptotic evaluation.

The radio-coverage simulators presented in [20], [92] evaluate the mul-

tiple interactions using the PO radiation integral. As expected, the computation time becomes frequency-dependent and is thus much higher than that of ray-tracers. However, they are expected to be more accurate since the diffraction is inherently taken into account within the radiation integrals. In [20], the PO currents and the scattered fields are, respectively, only evaluated, within and from the lit surfaces, i.e. the parts of the polygons which are illuminated by successive specular reflections. This approximation allows to reduce, for a given source domain, the computation of radiation integrals to fewer observation domains.

Besides, at UHF frequencies, the computation of the surface integral is extremely time-consuming since the building walls are about tens of wavelength wide. In [20], the calculations are performed using a brute force spatial-domain integration and a computation time of 15 min per receiver is mentioned for a two-dimensional scenario of medium size at 900 MHz. In [92], the integrals are analytically computed over triangles of fixed size assuming that the far-field approximation holds. The computation times observed for densely-built urban scenario of 1km wide at 100 MHz are in tens of hours. Hence, those two methods do not benefit from the long-standing effort made in the CEM field to develop fast computational methods which accelerate the computation of radiation integrals.

In this chapter, we explain how multiple scattering interactions could be evaluated with SPO. Particularly, the PO radiation integral can also be used to be evaluate the field behind the scatterer. In a scenario containing many facets, this approach will be time-consuming. In order to accelerate the computations, we will assume that we can only compute the interactions for which the observation plate lies nearby the region illuminated by GO specular reflections on the source plate. Indeed, those interactions are expected to produce the dominant field contributions. Hence, we need to determine the polygons illuminated by GO fields, i.e. the lit polygons. First, the lit polygons are rapidly determined using a Binary-Space Partitioning (BSP) tree. This tree was widely used for ray-tracing applications in the Computer Graphics field [94], [95] since it simultaneously provides a representation of the geometry and a hierarchical search structure which can be used to greatly simplify the determination of the lit surfaces and to decrease, with a high probability [96], its computational complexity from

quadratic $O(N_f^2)$ to linear $O(N_f)$ with N_f the number of facets of the scene. Then, we extend the SPO formulation to evaluate multiple scattering interactions between the lit polygons.

This chapter is organized as follows. In Section 5.2, we first explain how shadows are produced behind the scatterer from the PO radiation integral. In Section 5.3, we present the fast visibility method used to determine the lit surfaces. In Section 5.4, we apply the SPO to evaluate the multiple interactions. Finally, conclusions are drawn in Section 5.5.

5.2 Physical Shadowing

As already discussed in Chapter 3, the PO scattered fields are defined everywhere in space. Behind a plate, the scattered field $\mathbf{H}^s$ compensates the incident field $\mathbf{H}^i$ s.t. the magnitude of the total field $\mathbf{H}^t = \mathbf{H}^i + \mathbf{H}^s$ remains low. This forward-scattering effect is called physical shadowing [72], [93] and differs from the geometrical shadowing in which one must check whether the ray linking source and observation points is blocked or not by the scatterer.

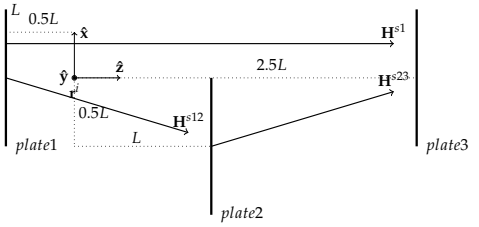

Figure 5.1: Shadowing scenario : a point source illuminates *plate*1. The back-scattered field from *plate*1 is evaluated on *plate*3 after being partially occluded by *plate*2.

Let us consider the example depicted in Fig. 5.1 in which a point source, located at the origin of the CS $(\hat{\mathbf{x}}, \hat{\mathbf{y}}, \hat{\mathbf{z}})$, illuminates *plate*1, of length $L = 30\lambda$ and centred at $-0.5L\hat{\mathbf{z}}$, and we want to evaluate the magnetic field $\mathbf{H}^s$ back-scattered from *plate*1 onto *plate*3, centred at $2.5L\hat{\mathbf{z}}$, after being partially occluded by *plate*2, centred at $L\hat{\mathbf{z}} - 0.5L\hat{\mathbf{x}}$. This can be done as follows. First, we compute the field $\mathbf{H}^{s13}$ and $\mathbf{H}^{s12}$, scattered from *plate*1 onto *plate*3 and

from *plate*1 onto *plate*2, respectively. Then, we evaluate the PO currents induced by $\mathbf{H}^{s12}$ on *plate*2 and the shadowing field $\mathbf{H}^{s23}$ radiated by those currents on *plate*3. Finally, the scattered field on *plate*3 is obtained with $\mathbf{H}^{s} = \mathbf{H}^{s13} + \mathbf{H}^{s23}$. The magnitude of $\mathbf{H}^{s13}$, $\mathbf{H}^{s23}$ and $\mathbf{H}^{s}$ are plotted in Fig. 5.2. One can observe that, as expected, $\mathbf{H}^{s}$ is weaker in the shadow created by *plate*2 on *plate*3 since $\mathbf{H}^{s23}$ partially compensates $\mathbf{H}^{s13}$.

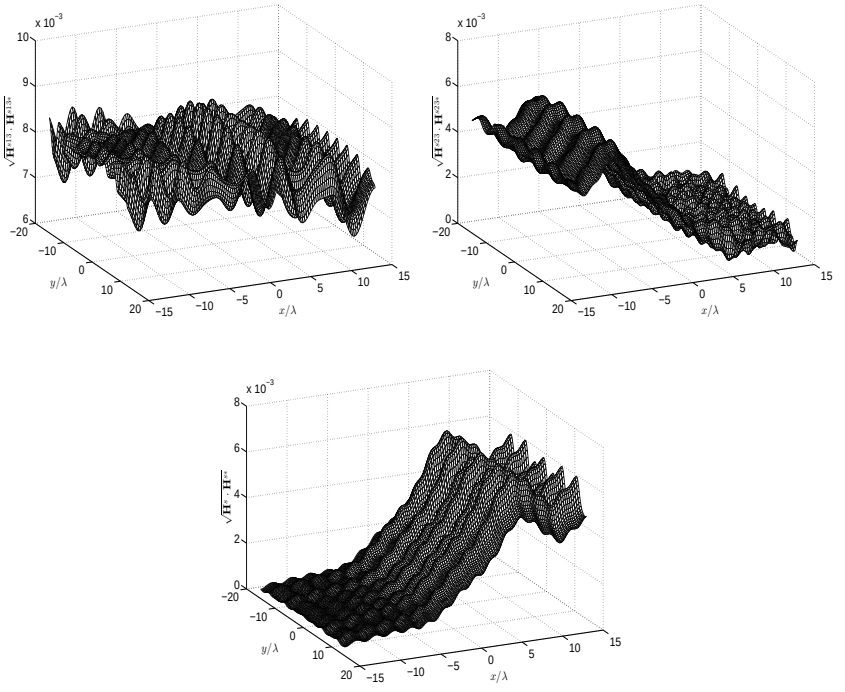

Figure 5.2: Magnitude of the magnetic field $\mathbf{H}^{s13}$ (top left), $\mathbf{H}^{s23}$ (top right) and $\mathbf{H}^{s}$ (bottom) for the scenario sketched in Fig. 5.1.

When the number N of observation plates increases, this iterative method becomes time-consuming since the number of shadowing interactions to be computed grows quadratically w.r.t. N. Hence, in order to accelerate the computations, we can assume that the interactions between a source plate and an observation plate which is not illuminated by a specular reflection are negligible at high frequencies. This assumption can be

understood by noting the fast decay of the electric field $\mathbf{E}^s$ on *plate*3 when moving in the shadow created by *plate*2. This selection of the interacting plates requires the determination of the lit surfaces as well as their front-to-back ordering from the source plate.

5.3 Fast visibility method

We present a three-step fast method which uses a tree structure to accelerate the determination of the lit surfaces. First, as an off-line step, a Binary Space Partitioning (BSP) tree having N_t nodes is constructed from a given set of N_f facets representing the scene independently from the position of transmitters and receivers. Secondly, the lit surfaces are rapidly determined using the tree and stored up to a maximum order of interactions for a given transmitter Tx. Finally, the visibility of the last interactions reaching the receivers Rx is tested.

5.3.1 Step 1 : Binary Space Partitioning

In Computer Graphics field, the Binary Space Partitioning (BSP) is a well-known tree structure [94] which simultaneously provides a representation of the geometry and a hierarchical search structure. It is built from an initial space that is recursively partitioned with a set of planes that intersects its interior. The BSP tree can be viewed as a generalisation to higher dimensions of binary search trees [95] and encompasses quadtrees and octrees in which the partition planes have fixed orientations. Such trees have been used for ray-tracing applications along with a Divide-and-Conquer algorithm to greatly simplify and accelerate the ordering of the potentially visible surfaces for a given view-point.

Generally, a BSP tree is built using an auto-partition scheme as follows. It is initially assumed that the polygons are listed and that their normals are outgoing to the related polyhedron.

1. A particular polygon is removed from the list and linked to the first node of the tree, the root node. The plane containing this polygon, called the cutting plane, is calculated using its normal and its corners.

2. The other polygons of the list are classified into two sub-lists, i.e.

front and back lists, depending on whether they are in the front or in the back of the cutting plane. For instance, the corners $\mathbf{r}_q$ of a polygon in front satisfies

$$\hat{\mathbf{n}} \cdot (\mathbf{r}_q - \mathbf{p}) > 0 \tag{5.1}$$

where $\hat{\mathbf{n}}$ is the normal of the cutting plane and $\mathbf{p}$ is a point on the plane. If the corners $\mathbf{r}_q$ are not all lying on the same side, this polygon is split into a front polygon and a back polygon using the cutting plane.

3. Two child nodes, denoted as front and back childrens, are added to the tree and linked to the root node. The sorting method is then restarted from 2) for the front and for the back children, separately, with their respective sub-lists of polygons.

This procedure ends when all the polygons are linked to a node of the tree.

Many trees of different sizes and shapes can represent a given set of N_f facets depending on how the cutting planes are selected at step 1). Finding an optimal tree having least depth and fewer nodes is a NP-hard problem. However, heuristic approaches already provide satisfactory results [94], [95]. We decide to select, among maximum 10 randomly-chosen polygons of the list, the cutting plane which minimizes the cost function

$$C = |N_{ba} - N_{fr}| + 2N_c \tag{5.2}$$

where N_{fr} and N_{ba} are the number of polygons in the front and in the back of a given cutting plane, respectively, and N_c is the number of polygons to be cut. In practice, it was observed [94], [96] that the tree size has a high probability to lie in between $N_t = O(N_f)$ and $N_t = O(N_f \log_2 N_f)$.

5.3.2 Step 2 : Determination of the lit polygons

The problem is stated as follows. Given a view-point and a polygonal screen, we need to determine which parts of the geometry are seen by the view-point through the screen. In a propagation context, the view-point and the polygonal screen are, respectively, an image of the transmitter

$$Tx$$

and the source polygon associated to the image of

$$Tx$$

. This is illustrated in Fig. 5.3 where the black point, the black surface and the grey surfaces are the view-point, the screen and the lit polygons, respectively.

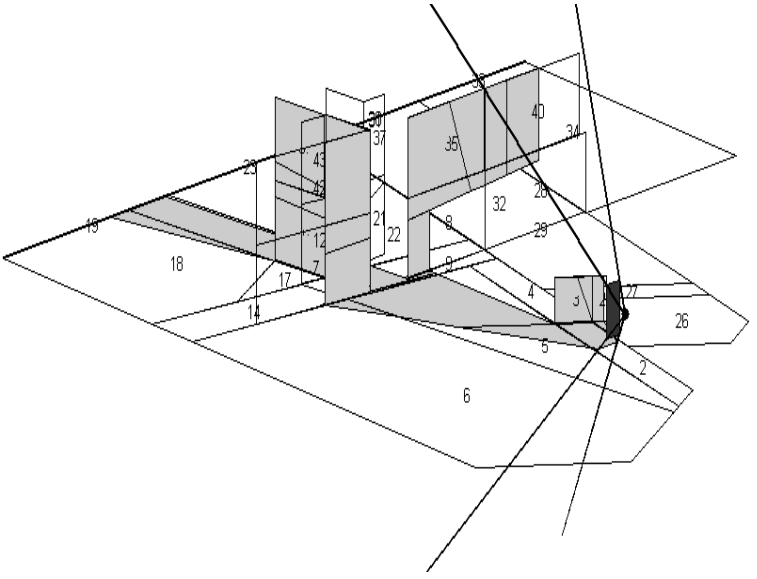

Figure 5.3: Illustration of the lit surfaces (grey) seen by a view point (black dot) through a source polygon (black).

The method starts from a small cube centred on Tx at $\mathbf{r}^i$. The lit polygons which are seen by Line-of-Sight (LoS) through one of the 6 cube faces are determined. At the next iteration, each of those lit surfaces becomes a source polygon for which the view-point is the image of Tx transmitter computed with

$$\mathbf{r}^{im} = \mathbf{r}^i + 2\left((\mathbf{r}_q - \mathbf{r}^i)\cdot\hat{\mathbf{n}}\right)\hat{\mathbf{n}} \tag{5.3}$$

where $\hat{\mathbf{n}}$ and $\mathbf{r}_q$ are the outgoing normal and a corner of the lit polygon, respectively. The lit surfaces seen by first-order reflections are then founded.

This procedure is repeated up to a maximum reflection order. The hierarchical relations between the lit surfaces are generally stored in another tree structure, called the reflection tree.

5.3.2.1 Back-face and view-frustum culling

Culling is a simple operation which rapidly reduces the set of polygons to be tested. The back-face culling selects the polygons which are not facing toward the source at $\mathbf{r}^{im}$ thanks to the following dot product

$$(\mathbf{r}_q - \mathbf{r}^{im}) \cdot \hat{\mathbf{n}} \geq 0 \tag{5.4}$$

where $\mathbf{r}_q$ and $\hat{\mathbf{n}}$ are the vertices and the normal of the polygon, respectively. Another culling method uses a view-frustum, i.e. a pyramid of square section as illustrated in Fig. 5.3, which encompasses the volume illuminated by a reflected field. The polygons which lie outside the frustum will never be seen by the source.

5.3.2.2 Fast front-to-back ordering

As highlighted in Fig. 5.3, the determination of the lit surfaces requires the ordering of the polygons from the nearest to the farthest w.r.t. the source point. Indeed, the near surfaces can occlude the visibility of the distant ones. A brute force computation of the spatial relations between N_f polygons entails a comparison between N_f^2 pairs and is time-consuming. The use of BSP trees greatly accelerate and simplify the visibility problem since the polygons are sorted by simply traversing the tree. This is explained [95] by noting that the polygons which are on the same side of a cutting plane as the source will never be occluded by the polygons on the opposite side.

The sorting procedure is described as follows. We start by traversing the tree from top to bottom by always choosing the child node which contains the source, i.e. either in the front or in the back of cutting planes. We should end up in a node which does not have a front child. Then, the following rules are applied. Each time a node is visited, its labelled polygon is inserted into a sorted list. If the two childrens of a node have not yet been explored, one must priorly visit the child node which contains the

source point. If both childrens have already been visited, we go to the parent node. This is repeated until all the nodes of the tree have been visited.

The computation times is thus proportional to the number of nodes N_b. Following the discussions in Section 5.3.1, the mean computational complexity is either $\mathcal{O}(N_f)$ or $\mathcal{O}(N_f \log N_f)$.

5.3.2.3 Perspective projection

One can equivalently consider that the source point is the pinhole of a camera, the source polygon is its display screen and that rays propagates backward from the scene toward the pinhole, such as sun rays. When a camera displays the scene onto the screen, the polygons at far distances appears smaller than those nearby. This effect is called perspective. The polygons displayed on the screen can be obtained using a perspective projection of the corners $\mathbf{r}_q$ of the real polygons, as illustrated in Fig. 5.4. This transformation is necessary to perform later the clipping operations.

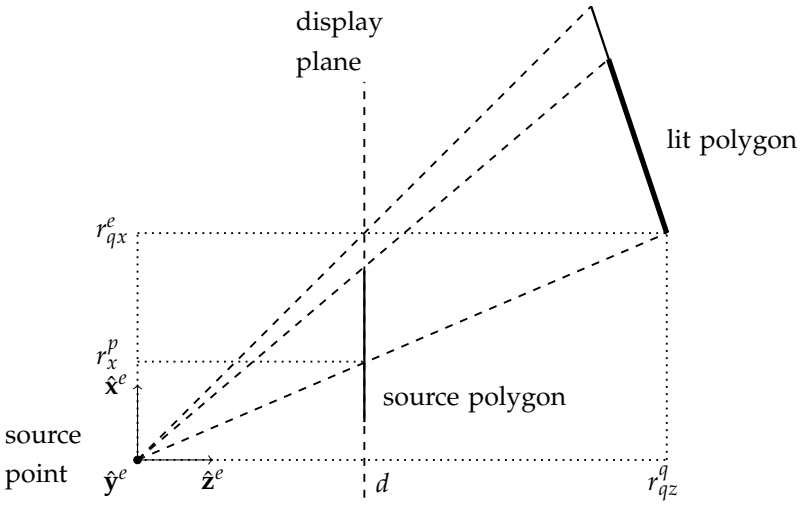

Figure 5.4: Two-dimensional illustration of the perspective projection of a PV polygon onto the image plane for a given source point.

Let us define an eye CS $(\hat{\mathbf{x}}^e, \hat{\mathbf{y}}^e, \hat{\mathbf{z}}^e) = (\hat{\mathbf{v}}, \hat{\mathbf{n}} \times \hat{\mathbf{v}}, \hat{\mathbf{n}})$ attached to the source polygon with edge $\hat{\mathbf{v}}$, centred on the image point $\mathbf{r}^{im}$. From 5.4, the pro-

jected coordinates of a corner $\mathbf{r}_q$ is obtained using similar triangles with

$$\begin{aligned} r_x^p &= d\, r_{qx}^e / r_{qz}^e \\ r_y^p &= d\, r_{qy}^e / r_{qz}^e \end{aligned} \tag{5.5}$$

where superscript p stands for projected, $d = \hat{\mathbf{n}} \cdot (\mathbf{r}^{im} - \mathbf{p})$ is the distance from the source point to the display plane containing a point $\mathbf{p}$, the coordinate of a corner in the eye CS is $\mathbf{r}_q^e = \mathbf{R} \cdot (\mathbf{r}_q - \mathbf{r}^{im})$ with $\mathbf{R}$ the rotation matrix to pass from the global CS to the eye CS.

5.3.2.4 Polygonal Clipping

Once the polygons have been culled, classified and projected, the projected coordinates of the lit surfaces are obtained by recursively performing intersections between the source polygon with the projected polygons. After each non-null intersections, the projected lit polygon must be subtracted from the source polygon since this part occludes the visibility to the next polygons. An example is shown in Fig. 5.5. Starting from top left to bottom right, one can distinguish the intersection polygon (grey), the clipped source polygons (grey+white) and the projected polygons (black+white) at each iteration. The clipping is repeated until all the polygons have been tested or when the source polygon is empty. Finally, the lit polygons are obtained by projecting back the intersection polygons.

One can also infer from Fig. 5.5 that the computation time of a clipping operation grows after each iteration since the number of edges of the clipped source polygon (grey+white) increases. Again, this is accelerated using a BSP representation of the source polygon [95] using the lines associated to its edges to recursively partition the two-dimensional space, in a similar way as for the three-dimensional case. The clipping operations are then performed by bursting the projected polygon through this two-dimensional BSP tree following the algorithms detailed in [97].

5.3.3 Step 3 : Last interactions

The last interaction corresponds to the evaluation of the field scattered from a lit polygon at a given observation point, i.e. a Rx receiver. The field can also be computed for an observation point which lies outside the

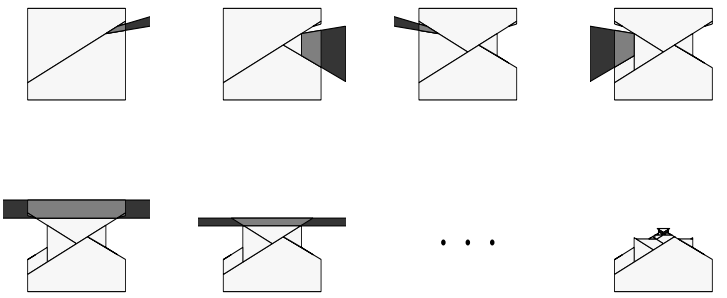

Figure 5.5: Clipping operations used for the determination of the lit surfaces. The intersection polygon (grey), the clipped source polygons (grey+white) and the projected polygons (black+white) are shown at each iteration starting from top left and ending at bottom right.

specular region. It may also happen that a receiver does not see the lit polygon in its entirety. In order to keep the computation costs low, this issue is resolved using the following simplified decision rule. A receiver is considered invisible only if the rays which link the image point and the corners to Rx are all blocked.

This method is still time-consuming since the number of ray-polygon intersection tests rapidly increases with the number of receivers. Again, the BSP tree helps to reduce this number by traversing the tree as follows. Each time a node is visited, the intersection between the ray and its labelled polygon is tested. If the ray extremities lie on the same side of the polygon, then the child node corresponding to the opposite side does not have to be visited since the polygons of this branch will never block the ray. When the observation point is close to the lit polygon, there is a high probability that the end points lie on the same of side of a cutting plane. Conversely, when the points are far from each other, the probability decreases. This acceleration thus exploits a principle of locality [95].

5.3.4 Numerical results

Two examples of BSP tree and related geometries of regions in Koekelberg and around the Flagey place in Brussels are shown in Fig. 5.6 and in Fig. 5.7, respectively. The number of polygons in the scene are around $N_f = 200$ and $N_f = 720$ and the number of nodes of each tree is $N_t = 568$ and $N_t = 2111$, respectively, for Koekelberg region and Flagey place. One can infer that both trees are compact since the number of nodes N_t is only around 3 times the number of facets N_f. In addition, they appear well-balanced with maximum depths of 12 and 17, respectively. Around 500 and 800 receivers are placed in a grid lying at 1.5m above the ground level for Koekelberg and Flagey, respectively.

The first-order and second-order lit polygons (grey) are shown in Fig. 5.8 for a given Tx position (black dot) in Koekelberg. The receivers seen by LoS (top) and after a single reflection (bottom) are also plotted in Fig. 5.9. Finally, the computation times for the three steps of the visibility algorithm considering up to 2 reflections are given in Table 5.1. One can note that the visibility computations are carried out in few minutes even for the large scenario (Flagey).

	Koekelberg	Flagey
Step 1	2 sec	9 sec
Step 2	35 sec	367 sec
Step 3	15 sec	151 sec

Table 5.1: Computation times for each step of the fast visibility.

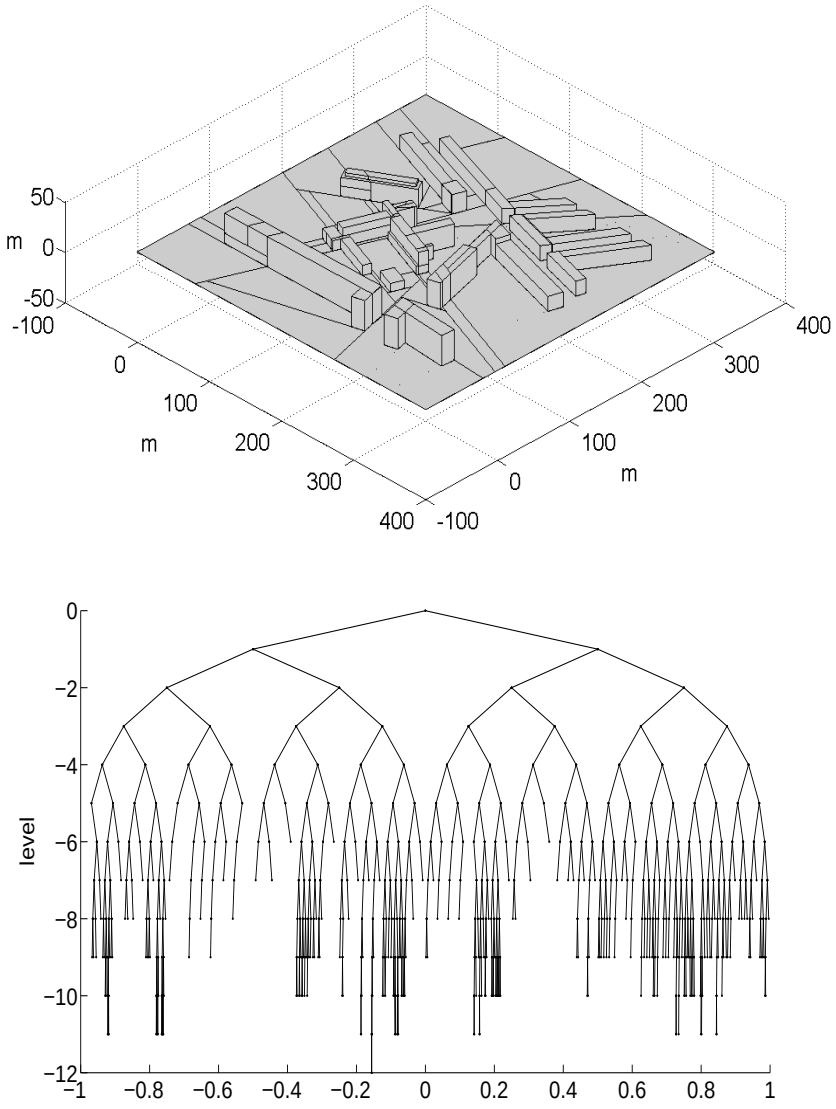

Figure 5.6: Mesh (top) and associated BSP tree (bottom) of Koekelberg region in Brussels.

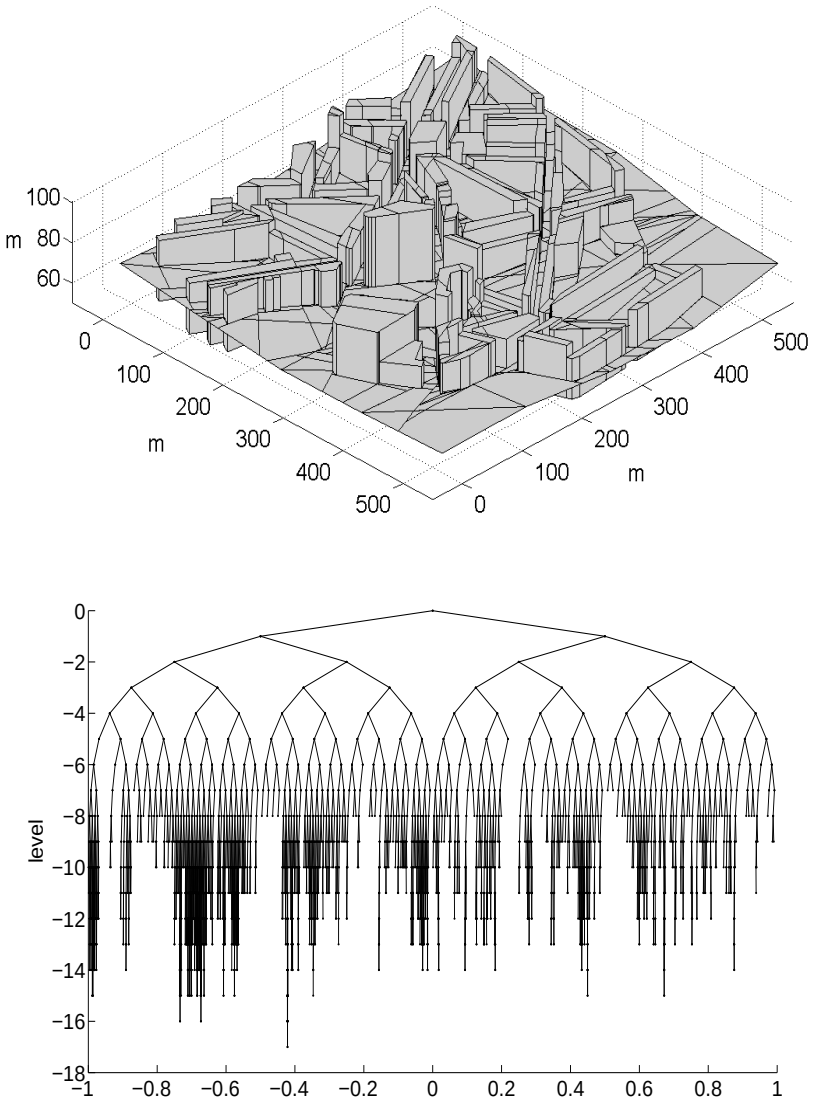

Figure 5.7: Mesh (top) and associated BSP tree (bottom) of Flagey place in Brussels.

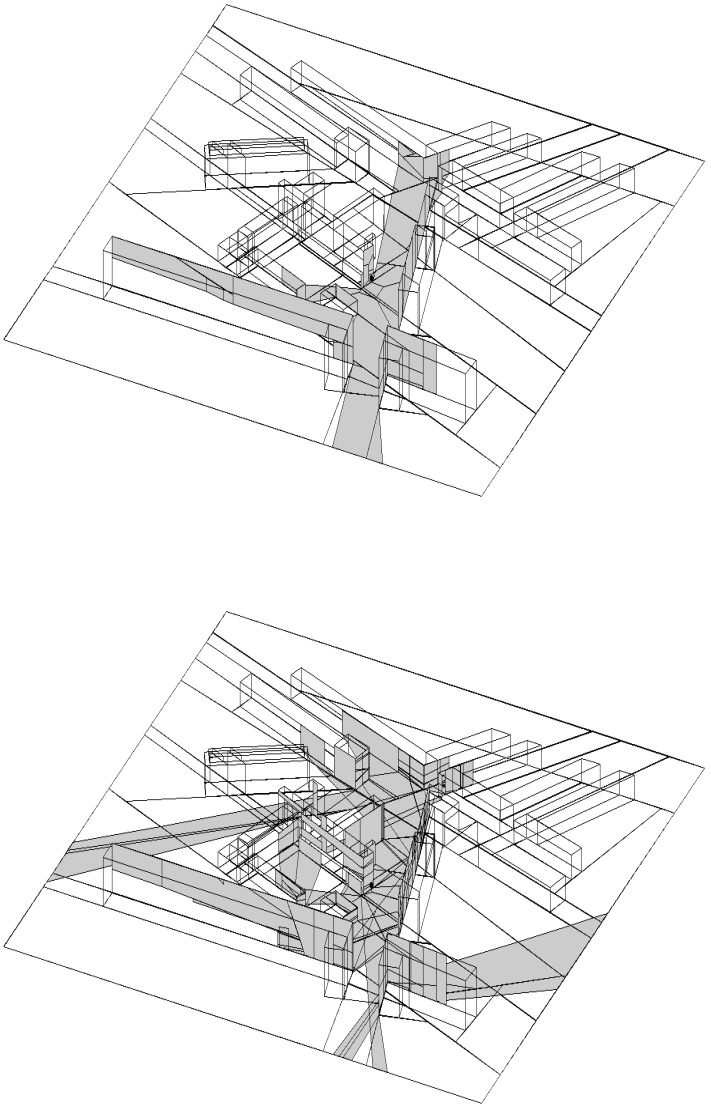

Figure 5.8: First-order (top) and second-order (bottom) lit polygons for a given Tx position (black dot) in Koekelberg region in Brussels.

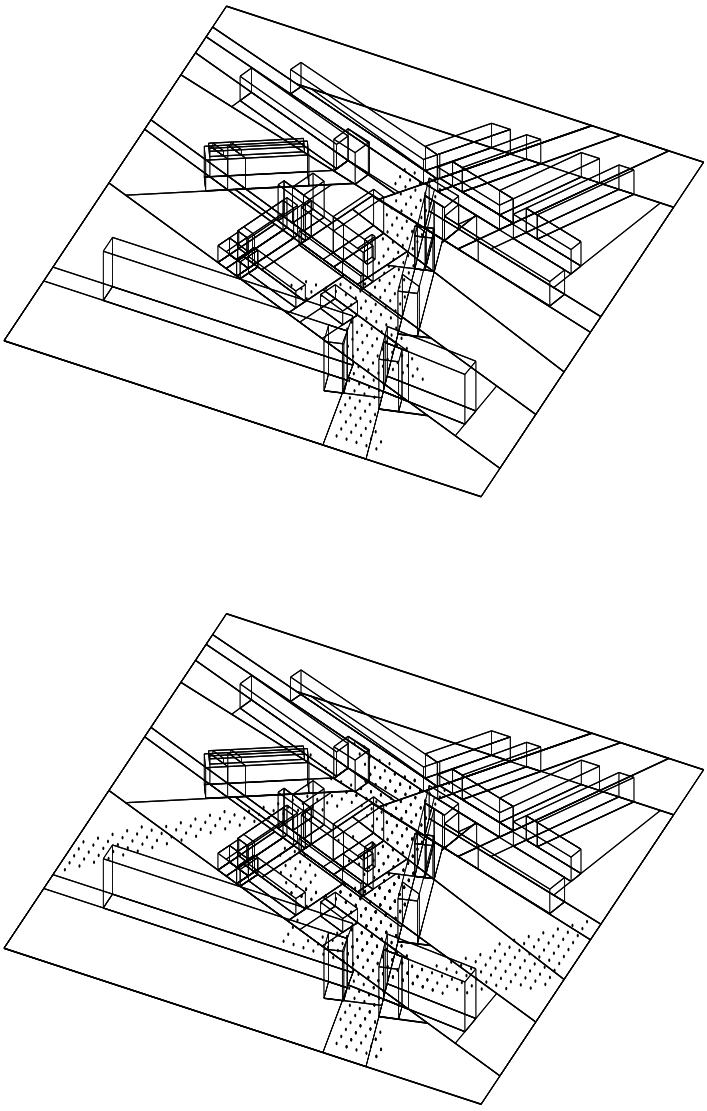

Figure 5.9: Receivers seen by LoS (top) and after a single reflection (bottom) for Koekelberg region in Brussels.

5.4 Multiple scattering interactions

We now explain with the simple example sketched in Fig. 5.10 how the fields resulting from multiple scattering are computed using the Spectral Physical Optics (SPO). Let us assume that a second-order interaction has been identified by the visibility algorithm. Precisely, it is found that a transmitter Tx located at $\mathbf{r}^i$ illuminates *polygon*1 by LoS and then *polygon*2 after reflection on *polygon*1. Finally, a last interaction is determined from *polygon*2 to a receiver Rx at $\mathbf{r}^o$.

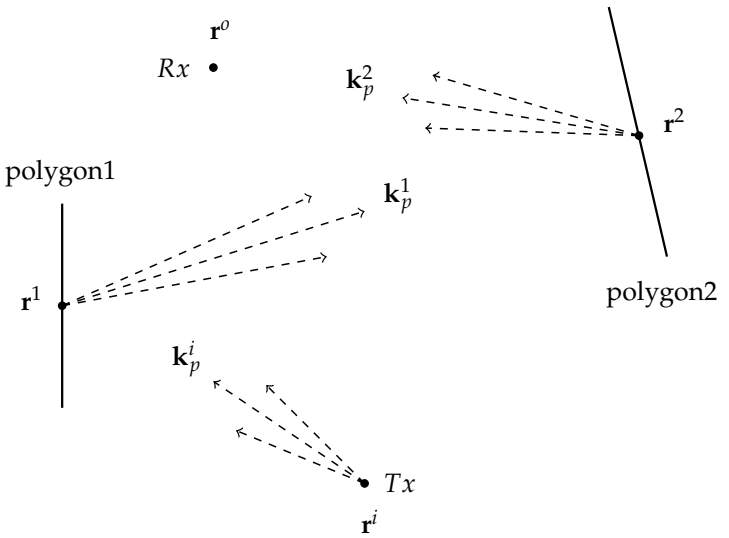

Figure 5.10: Two-dimensional illustration of the computation of multiple interactions with SPO.

The following methodology is used to compute the scattered field at Rx after two interactions. All vectorial quantities are expressed in a global CS.

1. A set $\mathbf{k}_p^i$ of P^i IPWs incident on *polygon*1 is defined using the sampling rules of Chapter 2. Then, the PWS of a point source antenna of orientation $\hat{\mathbf{p}}$ is evaluated analytically with

$$\tilde{\mathbf{H}}_p^i = -j\, \mathbf{k}_p^i \times \hat{\mathbf{p}} \tag{5.6}$$

For a more complex antenna, one could use an analytic continuation of its far-field pattern [21].

2. The incident spectrum is translated from $\mathbf{r}^i$ to the center $\mathbf{r}^1$ of *polygon*1 with

$$\tilde{\mathbf{H}}_p^{it} = w_p^i \, \tilde{\mathbf{H}}_p^i \, e^{-j\mathbf{k}_p^i \cdot (\mathbf{r}^1 - \mathbf{r}^i)} \tag{5.7}$$

where w_p^i is the spectral weight defined in (2.20) and the superscript t stands for translated.

3. A set $\mathbf{k}_p^1$ of P^1 IPWs is generated with the sampling rules considering that *polygon*1 is the source domain and *polygon*2 is the observation domain. Then, the PWS of the first-order scattered field from *polygon*1 is evaluated using SPO with

$$\tilde{\mathbf{H}}_q^1 = -2j \sum_p^{P^i} \mathbf{k}_q^1 \times \left(\hat{\mathbf{n}}^1 \times \tilde{\mathbf{H}}_p^{it} \right) \, W^1(\mathbf{k}_q^1 - \mathbf{k}_p^i) \tag{5.8}$$

where $\hat{\mathbf{n}}^1$ is the outgoing normal of *polygon*1 and W^1 is its associated window function computed with (3.6).

4. The PWS is translated from $\mathbf{r}^1$ to the center $\mathbf{r}^2$ of *polygon*2,

$$\tilde{\mathbf{H}}_p^{1t} = w_p^1 \, \tilde{\mathbf{H}}_p^1 \, e^{-j\mathbf{k}_p^1 \cdot (\mathbf{r}^2 - \mathbf{r}^1)} \tag{5.9}$$

5. A set of IPWs $\mathbf{k}_p^2$ is created from *polygon*2 toward the observation point $\mathbf{r}^o$. The PWS of the second-order scattered field is computed with

$$\tilde{\mathbf{H}}_q^2 = -2j \sum_p^{P^1} \mathbf{k}_q^2 \times \left(\hat{\mathbf{n}} \times \tilde{\mathbf{H}}_p^{1t} \right) \, W^2(\mathbf{k}_q^2 - \mathbf{k}_p^1) \tag{5.10}$$

where W^2 is the window function of *polygon*2.

6. Finally, the scattered magnetic field is evaluated at $\mathbf{r}^o$ with

$$\mathbf{H}^s(\mathbf{r}^o) = \sum_p^{P^2} w_p^2 \, \tilde{\mathbf{H}}_p^2 \, e^{-j\mathbf{k}_p^2 \cdot (\mathbf{r}^o - \mathbf{r}^2)} \tag{5.11}$$

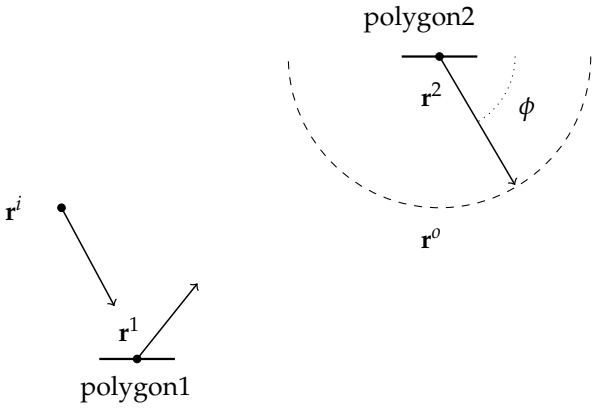

Figure 5.11: Double scattering scenario with $\mathbf{r}^i = (-L, 2L, 0)$, $\mathbf{r}^1 = (0, 0, 0)$, $\mathbf{r}^2 = (4L, 4L, 0)$. The observation path is a semi-circle of radius $R = 2L$ centred on $\mathbf{r}^2$.

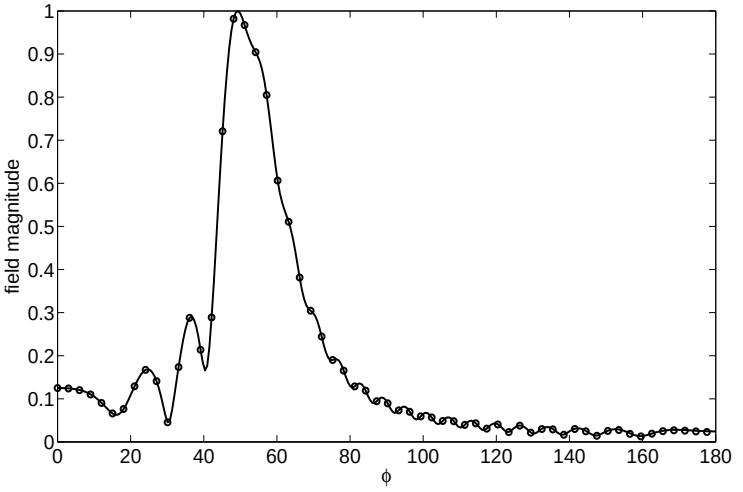

Figure 5.12: Comparison of the magnitude of the scattered magnetic field $\mathbf{H}^s$ for the scenario depicted in Fig. 5.9 obtained with SPO (solid) and with a brute-force spatial-domain integration (circles).

The costly computations are related to (5.8) and (5.10). Their number of operations are, respectively, $\mathcal{O}(P^i P^1)$ and $\mathcal{O}(P^1 P^2)$ and decrease substantially with the field of view between the source and *polygon*1 and between *polygon*1 and *polygon*2, as already discussed in Chapter 2.

This method is now validated for the double interaction sketched in Fig. 5.11. In this example, a first plate of length $L = 10\lambda$ centred at $\mathbf{r}^1 = (0,0,0)$ is illuminated by a point source located at $\mathbf{r}^i = (-L, 2L, 0)$. Then, the field scattered from the first plate illuminates a second plate of same width L centred at $\mathbf{r}^2 = (4L, 4L, 0)$. The magnitude of the magnetic field scattered from the second plate is then computed at observation points $\mathbf{r}^o$ lying within a semi-circular path of radius $R = 2L$ centred on $\mathbf{r}^2$, as shown in Fig. 5.11. One can see in Fig. 5.12 that the field obtained with SPO (solid) coincides with the one (circles) obtained with a brute force spatial-domain numerical integration using a mesh size $\lambda/4$. For this case, the computation times are, respectively, 2 sec and 0.3 sec for the spatial method and for SPO.

5.4.1 Discussions

We explain here some computational issues arising when one evaluates the scattered fields with SPO at close distances.

First, one can infer that, at a relative distance smaller than the size of the scattering domains, the IPW decomposition can diverge since the sampling rules of Chapter 2 do not anymore guarantee a reconstruction down to the target error level ϵ. A solution to this problem could consist of approximating the PO spectrum (5.8), (5.10) with the GO ones since the diffracted fields are less important close to the source.

Then, when the relative distances are above and close to the size of the plates, the number of plane waves P becomes roughly equal to the number of spatial samples N of a direct brute-force numerical integration, as seen in Chapter 3. Hence, in that case, the computation time of SPO is too high.

Finally, the evaluation of the scattered field with (5.11) requires the recomputation of the PWS with (5.10) for every observation point $\mathbf{r}^o$. This becomes particularly time-consuming when the number of Rx receivers increases, as it is the case in radio-coverage simulations. In contrast to SPO, an advantage of the spatial-domain integration is that, once the currents

have been computed on the polygons, they can be reused to compute the scattered field at another Rx observation point.

5.5 Conclusion

We presented an iterative method which uses the PO radiation integral to compute multiple scattering interactions with shadowing inherently taken into account. In order to lower the number of interactions to be computed, we have assumed that the PO currents are only defined over the facets which are lying inside the specular regions.

Hence, a three-step fast visibility method based on a Binary Space Partitioning (BSP) representation of the geometry was developed. It allows to lower the computational complexity for determining the lit surfaces from a given view-point from quadratic $O(N_f^2)$ down to linear $O(N_f)$ with N_f the number of facets. This method appears well-suited to scenarios with a static emitter and many receivers as is the case for a radio-coverage analysis or for a mobile receiver. It was shown through numerical results that the visibility computations up to 2 consecutive reflections are performed within few minutes even for a large urban environment.

Then, the computation of radiation integrals have been accelerated with the SPO by benefiting from the decreasing number of IPWs with the field of view between source and observation plates, as described in Chapter 2. However, it was explained that the computational costs are still too high for interactions at close distances or when the scattered field must be computed at many receivers. Hence, in the next chapter, we propose a fast method which overcome those issues by computing the interactions between the plates with FFTs and IPWs.

NFFT-based computation of radiation integrals over tilted source and observation plates

6

6.1 Introduction

The Fast Fourier Transform (FFT) algorithm [98] has played a key role in the development of fast computational methods for high-frequency electromagnetics. *Inter alia*, it has accelerated the simulations of large dielectric antennas [48], irregular arrays of antennas [47], inhomogeneous objects [99], radio-channels in urban environment [17], focal fields in microscopy [100] and inverse scattering problems [51].

Most FFT-based acceleration techniques inherently benefit from the convolution structure of the radiation integral which transforms current distributions into scattered fields [54]. This is generally reflected through a round trip from spatial to spectral domains accelerated with FFT's. We can still distinguish two main approaches. In the first one, the space is discretized with a volumetric grid and three-dimensional FFT's are used

to expedite the discrete convolution in the manner of [102]. The transition from spatial to spectral domain results from purely algebraic operations. For instance, this has been implemented in the Adaptive integral Method (AIM) [103] and the Precorrected-FFT (p-FFT) algorithm [104] for solving integral equations. The second approach uses two-dimensional closed-form expressions for the spectral Green's functions [51]. The computation of the source patterns and the vector fields is then accelerated with two-dimensional FFT-based methods. Compared to the first approach, important time savings could be expected from the reduction of the problem dimensionality. However, the spectral integration must be performed carefully along with a contour deformation, as discussed in the previous chapter. The combination of the efficiency of the FFT with the simplicity of an integral contour deformation in the complex plane is an important challenge.

In the context of scattering from layered media, the spectral integrals, often named Sommerfeld integrals, are computed with a contour deformation to circumvent the numerous singularities potentially appearing on and below the real axis. For electrically large domains and/or near-field distances, their computation becomes intensive. Moreover, the FFT cannot be directly used since the spectral integrals no longer have the structure of a Fourier transform. Hence, the Chirp z-transform (CZT) [109] was used in [106] to evaluate layered-media Green's functions in the far-field. This algorithm re-expresses Fourier transforms along a linear contour in terms of a convolution which can be computed with FFT's. Afterwards, it was implemented in [48] with a triangular contour, i.e. piecewise linear, to compute fields close to a two-dimensional aperture as well as patterns of a leaky-wave dielectric antenna. The ability of the CZT to decouple the spatial and spectral sampling can be particularly useful when the number of spatial samples is much larger than the required number of plane waves, i.e. spectral samples. However, it was not extended to the evaluation of three-dimensional very near and on-plane fields due to its limitation to linear contours. Later on, the contour-FFT (CFFT) [47] overcame this issue by rapidly evaluating the spectral integrals over arbitrary contour shapes with a truncated series of FFT's. The method has shown promising results in a Method-of-Moments analysis of very large irregular arrays of antennas

by computing the interactions between Macro Basis Functions [47] or in the direct evaluation of the scattered field, as part of an iterative solver [61]. A model of the error resulting from the truncation of the series in the CFFT has been derived in [32] and can be easily inverted to find the expansion order for given error level, contour height and domain size. The rapid increase of this order w.r.t. the contour height indicates that CFFT is less efficient than CZT to evaluate intermediate or far fields.

Recently, [107] analysed another fast method, called in [23] the unequally-spaced fast Laplace transform (USFLT), which basically extends the Non-equispaced Fast Fourier Transform (NFFT) [118] to efficiently evaluate discrete Fourier transforms with a contour deformation, i.e. Laplace sums. It involves the computation of a discrete complex convolution with a rapidly-decaying function and a single FFT. As for the CZT, the spatial and spectral grids are not linked. Hence, it is possible to benefit from the decrease of the number of plane waves with the size of the field of view in the intermediate-field region, as discussed in the previous chapter. A fast method combining IPW's and USFLT for the scattering analysis of arbitrarily oriented planes was presented in [107]. The case of arbitrarily oriented source and observation domains is more difficult and has not yet been addressed since it cannot be directly handled with CZT or CFFT. Indeed, even though the real-parts of the spectral samples are regularly defined in the local system of coordinates linking the centers of the domains, they are non-uniformly spread over the spectral domain in the reference systems of coordinates attached to source and observation planes in which the FFT's are performed. It was illustrated in [107] on the free-space Green's function through an example for which an important speed-up factor was observed, compared to a direct spectral integration, as done in the previous chapter to evaluate the Green's function. This method finds applications in scattering problems in which multiple interactions between electrically large facets must be computed. Typically, this is encountered in the simulations of channels inside a building or in an urban environment with iterative physical optics (IPO) or full-wave methods [17].

This chapter is organized as follows. In Section 6.4, we first describe the computational problem arising when one evaluates the free-space three-dimensional Green's function from its plane-wave decomposition with a

contour deformation at a large number of observation points. Then, in Section 6.3, we present a fast algorithm based on the unequally-spaced fast Laplace transform (USFLT). In Section 6.4, we present two other existing techniques, namely the CZT and the CFFT, and compare them to the USLFT. The vectorial extension of the fast method which rapidly evaluates vector fields on an observation plate from the currents lying on a source plate is presented in Section 6.5. Finally, results are summarized and conclusions are drawn in Section 6.7.

6.2 Statement of the scalar problem

We first describe the numerical problem arising when one evaluates the free-space three-dimensional Green's function from its plane-wave decomposition with a contour deformation at a large number of observation points. The extension of this problem to vector fields will be treated later.

Let us recall the plane-wave representation of the scalar free-space three-dimensional Green's function,

$$G(r) = \frac{1}{4\pi^2} \iint_{-\infty}^{\infty} \tilde{G}(k_\rho)\, e^{-jk_x x - jk_y y}\, \frac{k_\rho}{k_{\rho r}}\, \frac{\mathrm{d}k_\rho}{\mathrm{d}k_{\rho r}}\, \mathrm{d}k_{xr}\mathrm{d}k_{yr} \tag{6.1}$$

with the singular spectral Green's function known analytically,

$$\tilde{G}(k_\rho) = \frac{e^{-jk_z|z|}}{2jk_z} \tag{6.2}$$

As discussed in the previous chapter, the contour deformation along the radial spectral coordinate k_ρ is used to circumvent the free-space singularity of $\tilde{G}$ at $k_\rho = k$ and thus improve the accuracy of the forthcoming numerical integration. The discrete evaluation of the spectral integrals in (6.1) yields

$$G(r) = \frac{\Delta k^2}{4\pi^2} \sum_p \sum_q c_{pq}\, \tilde{G}(k_{\rho,pq})\, e^{-jk_{x,pq}x - jk_{y,pq}y} \tag{6.3}$$

where the coefficient $c_{pq} = k_{\rho,pq}/k_{\rho r,pq}\, \mathrm{d}k_{\rho,pq}/\mathrm{d}k_{\rho r,pq}$ accounts for the contour deformation. Next, we consider square observation domains of extent L discretized with $N = N_x^2 = N_y^2$ samples at rates $\Delta x = \Delta y$. Similarly, the spectral integrals are truncated at $k_{xmr} = k_{ymr} = k_{mr}$ and discretized with

$P = P_x^2 = P_y^2$ samples at a constant rate Δk using the sampling rules derived earlier. Those grids are illustrated in Fig. 6.1. This important loss of generality is only aimed at alleviating the further notations. The extension to rectangular domains with different sampling rates is straightforward.

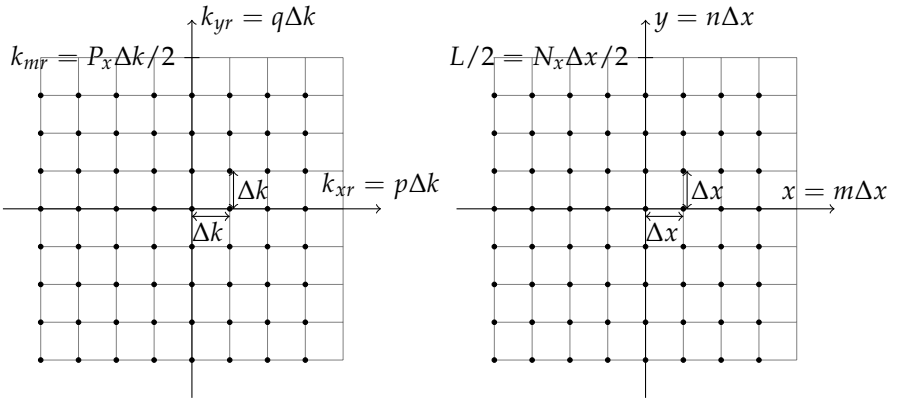

Figure 6.1: Spectral (left) and spatial (right) grids.

In the specific case when the observation points are located at a fixed distance z, the direct evaluation of the plane-wave decomposition with (6.3) on the gridded spatial domain can be rewritten as

$$G(r_{mn}) = \frac{\Delta k^2}{4\pi^2} \sum_p \sum_q c_{pq}\, \tilde{G}(k_{\rho,pq}) \; e^{\Delta x(k_{xi,pq}m + k_{yi,pq}n)}\; e^{-j\Delta k\Delta x(pm+qn)} \tag{6.4}$$

where $r_{mn} = \left(\Delta x^2(m^2+n^2) + z^2\right)^{1/2}$ is the distance from the origin. The direct computation of the sums in (6.4) requires NP operations. For large domains (from few tens of wavelengths) and/or for near-to-intermediate distances z, P and N increases and the computation becomes intensive. Hence, it is highly desirable to accelerate the computations with the Fast Fourier Transform (FFT) algorithm. However, (6.4) does not have the standardized structure required to apply FFT. This has been clearly highlighted in (6.4) by factorizing the terms into exponentials with purely real and imaginary arguments. Basically, the issue results from the use of a contour deformation in (6.1) which leads to non-null imaginary parts $k_{xi,pq}$ and $k_{yi,pq}$ in (6.4).

Finally, we consider a straight real-axis integration of the Green's function, i.e. $k_{\rho i} = k_{xi} = k_{yi} = 0$, in order to introduce the notations and symbols used later to compute Fourier transforms with the FFT algorithm. After a simple change of variables, as detailed in Appendix 6.8.1, the relation (6.4) can be computed with FFT provided that $\Delta x = \pi/k_{mr}$ and $L/2 = \pi/\Delta k$. The application of the FFT is denoted as

$$G(r_{mn}) \approx \frac{\Delta k^2}{4\pi^2} \, FFT\{\tilde{G}(k_{\rho,pq})\} \tag{6.5}$$

The number of basic operations performed when using a FFT is $N_{op} \approx c_1 N \log_2 N$ with $c_1 \approx 5$ [119]. Obviously, this numerical integration is strongly inaccurate since it does not circumvent the free-space singularity, as proven in [61]. Hence, a more sophisticated approach is seeked for.

6.3 NFFT-based acceleration

We present here a fast method which combines a contour deformation technique with the FFT algorithm to rapidly evaluate the plane-wave decomposition of the three-dimensional free-space Green's function over a large planar observation domain. It is based on an extension of the Nonequispaced Fast Fourier Transform (NFFT) algorithm [118] to deal with Laplace's transforms, i.e. Fourier transforms with a contour deformation, which was first presented in [23] and called the unequally-spaced fast Laplace transform (USFLT). In this section, we first recall and redemonstrate the NFFT algorithm. Then, we explain how the USFLT was derived from the NFFT to compute Fourier transforms with a contour and apply it to the evaluation of the Green's function. This generalizes the results of [23] to the two-dimensions.

6.3.1 The nonequispaced fast Fourier transform

By performing direct and inverse Fourier transforms of the product between the Green's function and an arbitrary window function ψ, we have

$$G(r) = \frac{1}{\psi(x,y)} \iint_{-\infty}^{\infty} \tilde{F}(k'_x, k'_y) \, e^{-jk'_x x - jk'_y y} \, \mathrm{d}k'_x \mathrm{d}k'_y \tag{6.6}$$

where the primed spectral coordinates k'_x and k'_y are real-valued. The inverse Fourier transform is given by

$$\tilde{F}(k'_x, k'_y) = \frac{1}{4\pi^2} \iint_{-\infty}^{\infty} G(r)\ \psi(x,y)\ e^{jk'_x x + jk'_y y}\ \mathrm{d}x\mathrm{d}y \tag{6.7}$$

If we assume that the spectral integrals (6.1) are performed on the real axis, i.e. without any contour, we can substitute them into (6.7) and swap spatial and spectral integrals,

$$\tilde{F}(k'_x, k'_y) = \frac{1}{16\pi^4} \iint_{-\infty}^{\infty} \tilde{G}(k_{\rho r})\ \iint_{-\infty}^{\infty} \psi(x,y) \\ e^{-j(k_{xr}-k'_x)x - j(k_{yr}-k'_y)y}\ \mathrm{d}x\mathrm{d}y\ \mathrm{d}k_{xr}\mathrm{d}k_{yr} \tag{6.8}$$

The inner spatial integral corresponds to the two-dimensional Fourier transform $\tilde{\psi}$ of the function ψ. Hence, we can write

$$\tilde{F}(k'_x, k'_y) = \frac{1}{4\pi^2} \iint_{-\infty}^{\infty} \tilde{G}(k_{\rho r})\ \tilde{\psi}(k_{xr} - k'_x, k_{yr} - k'_y)\ \mathrm{d}k_{xr}\mathrm{d}k_{yr} \tag{6.9}$$

This relation proves that the spectral integral (6.1) is mathematically equivalent to a normalized Fourier transform of the convolution between the spectral Green's function (6.2) and an arbitrary function $\tilde{\psi}$. The function $\tilde{\psi}$ is often selected to be rapidly decaying in order to accelerate the computation of the convolution (6.9). The following, properly truncated, Gaussian functions are often used [118], [23]

$$\begin{aligned} \psi(x,y) &= e^{-\mu(x^2+y^2)} \\ \tilde{\psi}(k_x, k_y) &= \frac{\pi}{\mu}\, e^{-(k_x^2+k_y^2)/(4\mu)} \end{aligned} \tag{6.10}$$

where μ is the variance. The discrete evaluation of the convolution (6.9) between the spectral Green's function $\tilde{G}$ and the rapidly-decaying Gaussian function $\tilde{\psi}$ is sketched in Fig. 6.2 in the one-dimensional case. One can infer from this figure that only few values of k'_x will be affected for each plane-wave sample $k_{xr,pq}$. Hence, the convolution can be rapidly computed. This algorithm is called the unequispaced fast Fourier transform (NFFT). A fundamental property of the NFFT formulation exploited in the pioneering work of [118] is that it remains valid when the spectral samples are irregularly spaced.

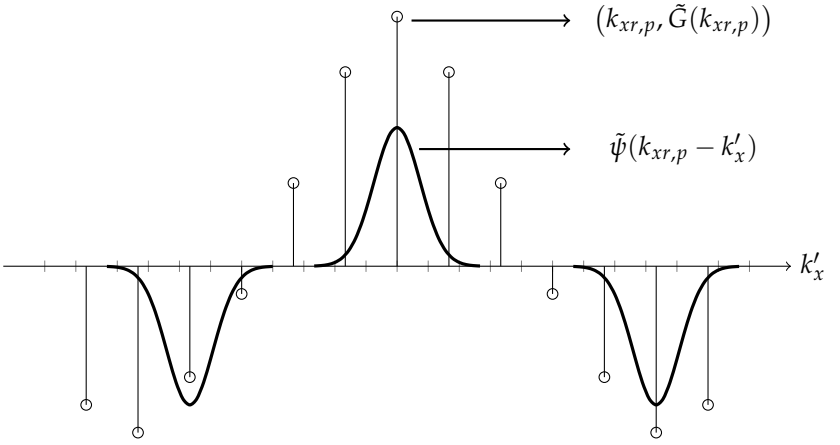

Figure 6.2: Unidimensional illustration of three efficient convolutions between the spectral Green function $\tilde{G}$ (circle) and the window function $\tilde{\psi}$ (solid).

6.3.2 The unequally-spaced fast Laplace transform

The fundamental observation implicitly exploited in [23] is that a similar transition as that from (6.8) to (6.9) in the derivation of the classical NFFT can be used when the inner spectral integral is evaluated with a contour deformation. To prove this statement, let us start again from (6.8) when the spectral integrals (6.1) evaluated with an arbitrary contour have been substituted in (6.7),

$$\tilde{F}(k'_x, k'_y) = \frac{1}{16\pi^4} \iint_{-\infty}^{\infty} \tilde{G}(k_{\rho r}) \, \frac{dk_\rho}{dk_{\rho r}} \, \frac{k_\rho}{k_{\rho r}} \iint_{-\infty}^{\infty} \psi(x,y) \, e^{-j(k_x - k'_x)x - j(k_y - k'_y)y} \, \mathrm{d}x\mathrm{d}y \, \mathrm{d}k_{xr}\mathrm{d}k_{yr} \tag{6.11}$$

One must note that the spectral variables k_x and k_y are now complex-valued due to the contour while the primed variables k'_x and k'_y remain real. The inner integral now corresponds to the Laplace transform of the function ψ since $k_x - k'_x$ and $k_y - k'_y$ are complex numbers. It can be evaluated from an analytical continuation of the real-axis Fourier transform,

$$\tilde{F}(k'_x, k'_y) = \frac{1}{4\pi^2} \iint_{-\infty}^{\infty} \tilde{G}(k_\rho) \, \tilde{\psi}(k_x - k'_x, k_y - k'_y) \, \frac{dk_\rho}{dk_{\rho r}} \, \frac{k_\rho}{k_{\rho r}} \, \mathrm{d}k_{xr}\mathrm{d}k_{yr} \tag{6.12}$$

Comparing (6.9) with (6.12), we can conclude that the convolution is now computed with a contour deformation which is identical to the one used in the initial spectral decomposition of the Green's function (6.1). Intuitively, we can assume that the contour deformation produces spectral samples irregularly spaced over the complex plane. The Gaussian window was selected in the one-dimensional numerical analysis of [23]. As clearly mentioned, this function becomes slightly modulated when evaluated at complex arguments, as sketched in Fig. 6.3. Hence, compared to the real case, it must be sampled at a higher rate when the convolution is computed numerically. Using $x^2 + y^2 = \rho^2$ and $k_x^2 + k_y^2 = k_\rho^2$, we can further expand them into

$$\begin{aligned} \psi(x,y) &= e^{-\mu\rho^2} \\ \tilde{\psi}(k_x - k'_x, k_y - k'_y) &= \frac{\pi}{\mu}\, e^{-(k_\rho^2 + k_\rho'^2)/(4\mu)}\; e^{(k_x k'_x + k_y k'_y)/(2\mu)} \end{aligned} \tag{6.13}$$

where $k_\rho'^2 = k_x'^2 + k_y'^2$. In the following considerations, the numerical half-width of $\tilde{\psi}$ will be denoted by M.

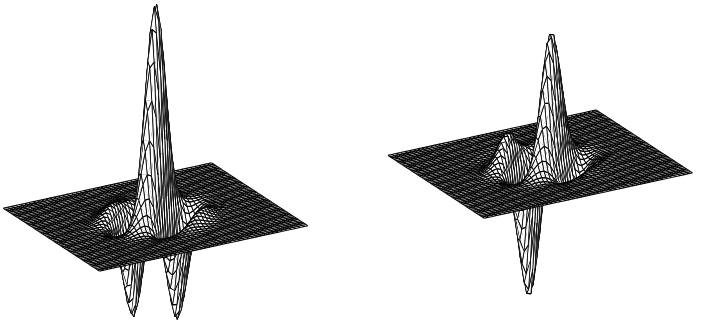

Figure 6.3: Real (left) and imaginary (right) parts of $\tilde{\psi}(k'_x - k_x, k'_y - k_y)$ with $k_x = k_y = 0.3kj$.

According to [23], the convolution must be discretized at a Nyquist rate

$\Delta k' = \pi/(\nu L/2)$ where ν is the oversampling ratio. This yields

$$\tilde{F}\left(k'_{x,u}, k'_{y,v}\right) = \frac{\pi}{\mu} \frac{e^{-k'^2_{\rho,uv}/(4\mu)}}{(\nu L)^2} \sum_p \sum_q c_{pq}\, \tilde{G}(k_{\rho,pq})\, e^{-k^2_{\rho,pq}/(4\mu)} \\ e^{(k_{x,pq}k'_{x,u} + k_{y,pq}k'_{y,v})/(2\mu)} \tag{6.14}$$

and $k'_{x,u} = \pi u/(\nu L/2)$ and $k'_{y,v} = \pi v/(\nu L/2)$ are the sampled real-valued spectral prime coordinates. An additional condition provided in [23] is that $|k_{xr}|, |k_{yr}| < \pi/\Delta x - \pi M/(\nu L/2)$. It is important to recall that only $(2M+1)^2$ values of $\tilde{F}$ are modified by each term of indices (p, q) in (6.14) since the function $\tilde{\psi}$ can be truncated at argument values $k'_x = k_{xr} \pm M\Delta k'$ and $k'_y = k_{yr} \pm M\Delta k'$. Symbolically, the USFLT algorithm can be formulated as

$$\begin{aligned} G(r_{mn}) &\approx \frac{\Delta k^2}{4\pi^2}\, USFLT\{\tilde{G}(k_{\rho,pq})\} \\ &\triangleq \frac{\Delta k^2}{4\pi^2}\, e^{\mu\rho^2_{mn}}\, FFT\{\tilde{F}(k'_{x,u}, k'_{y,v})\} \end{aligned} \tag{6.15}$$

where $\rho^2_{mn} = \Delta x^2(m^2 + n^2)$ and the FFT is performed on an oversampled $\nu N_x \times \nu N_x$ grid. It is interesting to point out that only a single two-dimensional FFT is involved in the USFLT algorithm.

The error models have been developed and inverted in [23] for the one-dimensional case considering a reference complex exponential and a given error level $|\epsilon|$. Those can be fairly used in this two-dimensional extension. In addition, for the sake of simplicity, we decide to fix the oversampling ratio to $\nu = 2$. From [23], the variance of the Gaussian functions (6.13) can be selected with

$$\mu = \frac{a_{im}}{L} + \frac{-\ln|\epsilon|}{2L^2} \tag{6.16}$$

where $a_{im} = \max(k_{xi,pq}, k_{yi,pq})$. In addition, the width M of $\tilde{\psi}$ can be obtained from [23] by rounding

$$M = \frac{1}{\pi}\left(a^2_{im}L^2 + 9/4\,(-\ln|\epsilon|)^2 - 5\ln|\epsilon|\; a_{im}L\right)^{1/2} \tag{6.17}$$

The Green's function and its associated relative error considering a parabolic contour are illustrated in Fig. 6.4 over a square domain of side 20λ at a distance $z = \lambda$. The target error has been set to $\epsilon_{tar} = 10^{-2}$. One

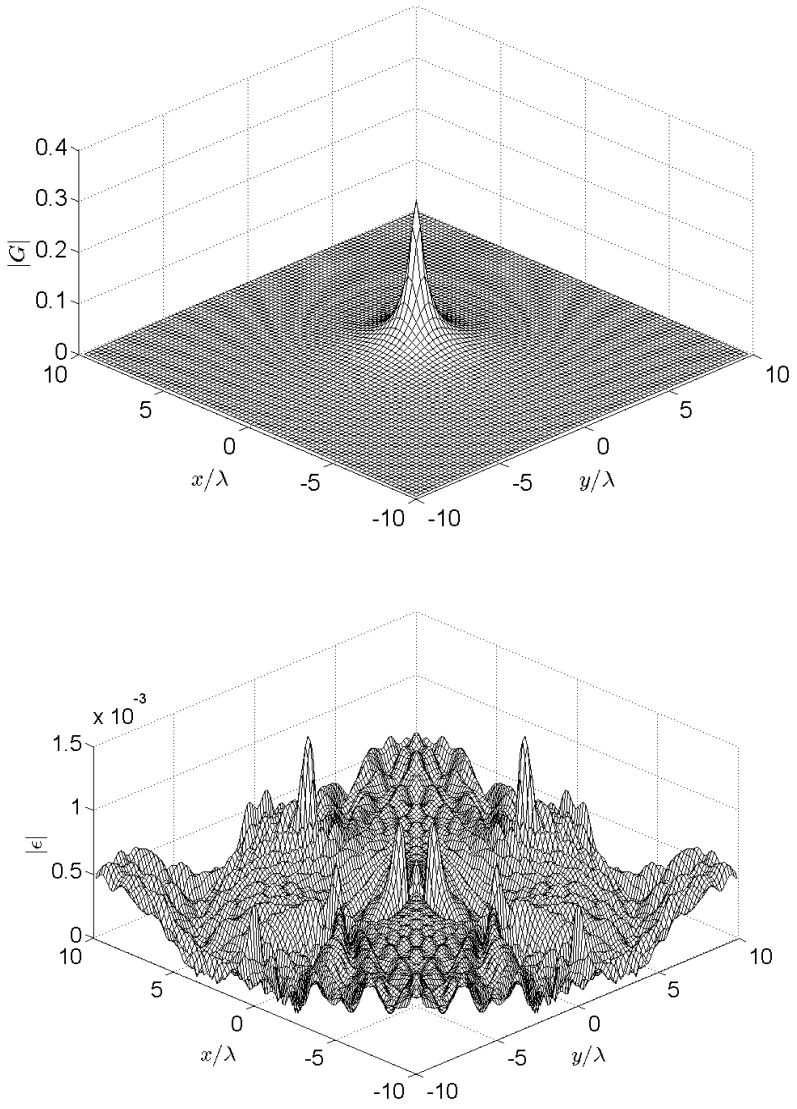

Figure 6.4: Green's function and relative error of USFLT for $z = 0.25\lambda$, $a = 0.03$, $L = 40\lambda$, $\epsilon_{tar} = 10^{-2}$, $M = 4$ and a parabolic contour.

can observe that the error is below 10^{-2} over the observation domain. This validates the formulas (6.16) and (6.17).

It is now fundamental to note that the cost of the convolution depends on the number of plane waves P and not on the number of spatial samples N. Since the convolution (6.14) is not separable due to the contour which links k_{xi} and k_{yi}, it costs $(2M+1)^2 P$ operations. Generally speaking, the number of operations is thus given by

$$N_{op} = 4\, c_1 N \log_2 N + (2M+1)^2 P \tag{6.18}$$

for $\nu = 2$. In the following discussions, we will thus emphasize the comparison between $(2M+1)^2$ and $4c_1 \log_2 N$.

6.4 Other FFT-based methods

In this section, we first present the Chirp z-transform (CZT) [109] and the Contour-FFT [47] algorithms along with its error model and explain how they allow a fast evaluation of the radiation integral on a planar observation domain at fixed distance z. Then, we compare them with the USFLT.

6.4.1 The chirp z-transform

Let us rewrite the spectral integral (6.1) for a linear contour of slope a with

$$G(r) = \frac{(1+ja)^2}{4\pi^2} \int_{-\infty}^{\infty} e^{-j(1+ja)k_{yr}y} \int_{-\infty}^{\infty} \tilde{G}(k_\rho)\, e^{-j(1+ja)k_{xr}x}\, \mathrm{d}k_{xr}\mathrm{d}k_{yr} \tag{6.19}$$

This separable formulation indicates that the integration with a linear contour along k_ρ can be numerically performed by consecutively integrating along k_x and k_y with a contour of the same slope.

Let us start by discretizing (6.19) in the same manner as for (6.4),

$$G(r_{mn}) = \frac{\Delta k^2}{4\pi^2} (1+ja)^2 \sum_p \sum_q \tilde{G}(k_{\rho,pq})\, e^{-j\Delta k \Delta x (1+j\alpha)(pm+qn)} \tag{6.20}$$

Then, we define the following quantities

$$W = e^{-j(1+ja)\Delta x \Delta k}$$
$$z_p = W^p \tag{6.21}$$

This allows to express (6.20) in the form of a two-dimensional z-transform,

$$G(r_{nm}) = \frac{\Delta k^2}{4\pi^2}\,(1+ja)^2 \sum_p \sum_q \tilde{G}(k_{\rho,pq})\, z_p^m z_q^n \tag{6.22}$$

The z-transform is the discrete version of the Laplace transform, as the discrete Fourier transform (DFT) is that of the Fourier transform. Next, we can insert the Bluestein's substitutions [109],

$$mp = \left(p^2 + m^2 - (p-m)^2\right)/2$$
$$nq = \left(q^2 + n^2 - (q-n)^2\right)/2 \tag{6.23}$$

into (6.22) to rewrite it in the form of a convolution,

$$G(r_{nm}) = \frac{\Delta k^2}{4\pi^2}\,(1+ja)^2\, W^{(m^2+n^2)/2} \sum_p \sum_q \tilde{G}(k_{\rho,pq})\, W^{(p^2+q^2)/2}\, W^{-(p-m)^2-(q-n)^2} \tag{6.24}$$

Within the sums of (6.24), one can clearly identify a first factor which only depends on p and q and a second factor which is a function of $p-m$ and $q-n$. This corresponds to the discretization of a convolution integral. Mathematically, such integral can be efficiently evaluated by multiplying the spectra of both factors in the Fourier domains of $k_{xr} = p\Delta k$ and $k_{yr} = q\Delta k$ and by using FFT's to perform the direct and inverse Fourier transforms [102]. After few simple algebraic operations, the CZT algorithm can be symbolically defined from (6.24) by

$$G(r_{mn}) \approx (1+ja)^2\, \frac{\Delta k^2}{4\pi^2}\, CZT\{\tilde{G}(k_{\rho,pq})\} \tag{6.25}$$

with

$$CZT\{\tilde{G}(k_{\rho,pq})\} \triangleq FFT^{-1}\{FFT\{\tilde{G}(k_{\rho,pq})\, e^{-j(1+ja)k^2_{\rho r,pq}/2}\} FFT\{e^{-j(1+ja)(k^2_{xr,p}+k^2_{yr,q})/2}\}\} \tag{6.26}$$

where the symbolic operation FFT has been defined in (6.5) and FFT^{-1} stands for the inverse Fast Fourier Transform. It is clear from (6.21) that, in contrast to the standard FFT algorithm, the CZT allows us to use decoupled spatial and spectral grids. In addition, it is important to recall that the CZT algorithm is purely algebraic and that it only produces an additional round-off error which results from the multiplication with increasing exponentials in (6.26). The CZT has been implemented in a built-in Matlab function *czt* [112].

When $P \ll N$ and P is small enough, a direct summation of (6.22) is more efficient. Indeed, we can benefit from the separability of the exponentials in (6.19) to reduce its number of operations down to $PN_x + NP_x$ instead of PN. On the contrary, when P becomes large enough, the CZT algorithm (6.25) is faster. The convolution in (6.24), carried out using FFTs in (6.25), is the most time-consuming part and its operation count, when $N = P$, is given in [102] by

$$N_{op} = 3\, c_1 N \log_2 N \tag{6.27}$$

where c_1 is the constant appearing in a single FFT.

When $P \ll N$ and P remains large, e.g. for intermediate fields, one can implement the sectioning method [102] to use smaller FFTs and further accelerate the computation of the convolution. When P_x divides N_x exactly, the number of operations is reduced to [102]

$$N_{op} \approx 2\,(2N + P)\, c_1 \log_2 P \tag{6.28}$$

6.4.2 The contour-FFT algorithm

Let us expand the exponentials in the integrand of (6.1) into

$$G(r) = \frac{1}{4\pi^2} \iint_{-\infty}^{\infty} \tilde{G}(k_\rho)\, e^{k_{xi}x + k_{yi}y} \\ e^{-jk_{xr}x - jk_{yr}y}\, \frac{k_\rho}{k_{\rho r}}\, \frac{\mathrm{d}k_\rho}{\mathrm{d}k_{\rho r}}\, \mathrm{d}k_{xr}\mathrm{d}k_{yr} \tag{6.29}$$

The authors of [47] then decided to approximate the real exponentials in (6.29) with a two-dimensional Taylor series,

$$e^{k_{xi}x + k_{yi}y} = \sum_{t=0}^{T} \sum_{s=0}^{t} \frac{P_{ts}}{t!}\, \gamma^t\, (k_{xr}x)^t\, (k_{yr}y)^{t-s} \tag{6.30}$$

where $\gamma = k_{\rho i}/k_{\rho r}$, P_{ts} is the (t,s) entry of the Pascal triangle and T is the expansion order of the Taylor series. This allowed them to factorize each power of xy resulting from this series out of the integral and to re-express the contour integral (6.29) with a series of Fourier transforms,

$$G(r) = \frac{1}{4\pi^2}\sum_{t=0}^{T}\sum_{s=0}^{t}\frac{P_{ts}}{t!}\,x^t y^{t-s}\iint_{-\infty}^{\infty}\gamma^t\,k_{xr}^t\,k_{yr}^{t-s}\,\tilde{G}(k_\rho) \\ e^{-jk_{xr}x-jk_{yr}y}\,\frac{k_\rho}{k_{\rho r}}\,\frac{\mathrm{d}k_\rho}{\mathrm{d}k_{\rho r}}\,\mathrm{d}k_{xr}\mathrm{d}k_{yr} \tag{6.31}$$

The FFT algorithm can now be used to compute the Fourier transforms in each term of (6.31). This technique has been called the Contour-FFT (CFFT) [47] and is symbolically written as [61]

$$\begin{aligned} G(r_{mn}) &\approx \frac{\Delta k^2}{4\pi^2}\,CFFT\{\tilde{G}(k_{\rho,pq})\} \\ &\triangleq \frac{\Delta k^2}{4\pi^2}\sum_{t=0}^{T}\sum_{s=0}^{t}\frac{P_{ts}}{t!}\,x_m^t y_n^{t-s} \\ &\qquad FFT\{\gamma^t\,k_{xr,p}^t\,k_{yr,q}^{t-s}\,c_{pq}\,\tilde{G}(k_{\rho,pq})\} \end{aligned} \tag{6.32}$$

One can note that the CFFT is subject to the same restrictions (6.51) in Appendix 6.8.1 as those of the FFT.

In view of (6.32), one can infer that an error originates from the truncation of the Taylor series. Hence, we next derive a mathematical model of this error for the two-dimensional Green's function. The exact remainder of the Taylor series of an exponential can be identified as an incomplete lower gamma function p times an exponential [108]. Finding a closed-form expression of the error on the Green's function after integration is more challenging. Since this error is mostly influenced by the contour height, we will consider a straight path of constant height ak which corresponds to the maximum value taken by k_{xi} along the exact path, as sketched in Fig. 6.5.

The contour integral is then given by

$$\epsilon = \frac{1}{2\pi G(r)}\int_{-\infty}^{\infty}\tilde{G}(k_x)\;p(T+1,k_{xi}x)\;e^{-jk_x x}\,\mathrm{d}k_{xr} \\ +\frac{j}{2\pi G(r)}\int_{-ak}^{ak}\tilde{G}(jk_{xi})\;p(T+1,k_{xi}x)\;e^{k_{xi}x}\,\mathrm{d}k_{xi} \tag{6.33}$$

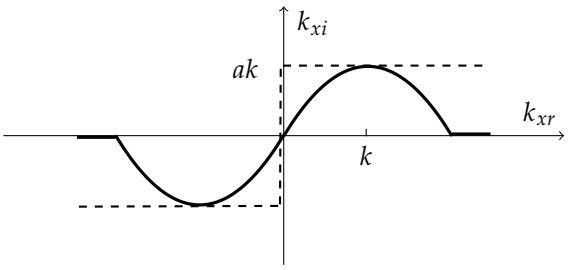

Figure 6.5: Illustration of a straight path (dashed) for the estimation of the Taylor series error when evaluating the two-dimensional Green's function.

where p is the incomplete lower gamma function, $k_{xi} = ak$ for $k_{xr} \geq 0$ and $k_{xi} = -ak$ for $k_{xr} < 0$. For a low contour, we can neglect the integral on the imaginary axis and evaluate the amplitude of the relative error with

$$|\epsilon| \approx p(T+1, ak|x|) \tag{6.34}$$

One can note that this error is maximum at the side of the spatial domain at $x = x_{\max}$. We can tabulate the inverse function which express T vs. $ak|x|$ and $|\epsilon|$. The model (6.34) is thus equal to the relative error of the Taylor series of a single exponential. Hence, an heuristic extension to the three-dimensional case can be obtained by replacing akx with $ak\rho$ in (6.34). First, this heuristic model is validated in Fig. 6.6 through a comparison with the numerically-computed error for a distance $z = \lambda$ and three different expansion orders T and contour height a. Those values have been selected to highlight the large range of validity of the error model (6.34). Then, the numerically-computed relative error is shown in Fig. 6.7 for the same example as described for USFLT. The target error has been set to $\epsilon_{tar} = 10^{-2}$ and the expansion order $T = 7$ is selected with (6.34). One can see that the relative error is maximum at $x = y = L/2$ where it almost reaches 10^{-2}.

When $N = P$ is a large power of 2, the computational cost is dominated by the computation of the $T + 1$ FFT's in (6.32). The number of operations related to this step is evaluated with [47]

$$N_{op} = c_1 \, (T+1) \, (T/2+1) \, N \log_2 N \tag{6.35}$$

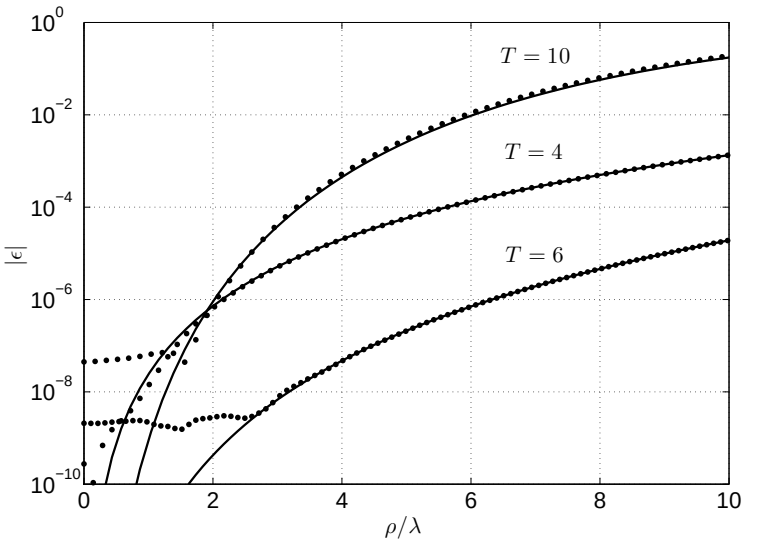

Figure 6.6: Model (solid) and exact value (dotted) of the CFFT error for $z = \lambda$, $(a, T) = \{(0.01, 4), (0.01, 6), (1, 10)\}$.

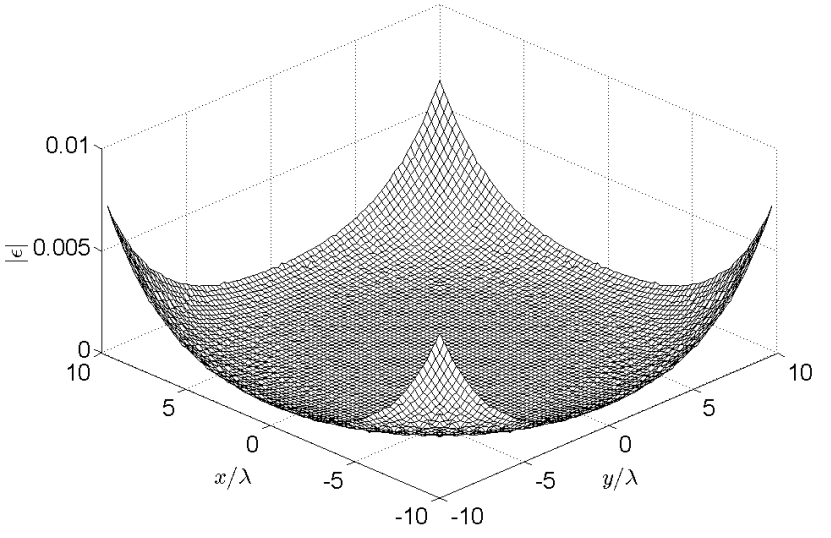

Figure 6.7: Green's function and relative error of CFFT for $z = 0.25\lambda$, $a = 0.03$, $L = 40\lambda$, $\epsilon_{tar} = 10^{-2}$, $T = 7$ and a parabolic contour.

6.4.3 Discussions

We will compare the reconstruction of the spatial-domain Green's function within an observation domain of length L at a fixed distance z/λ with the three fast methods, namely USFLT, CZT and CFFT. The number of operations required by each fast method is summarized in Table 6.1.

Method	N_{op}
Direct	PN
CZT	$3\,c1\;N\;\log_2 P$
CFFT	$c_1\;(T+1)\;(T/2+1)N\log_2 N$
USFLT	$4\;c_1 N\log_2 N+(2M+1)^2\;P$

Table 6.1: Number of operations of the fast methods.

First, it is important to clearly mention a property when evaluating numerically the plane-wave representation (6.1). It is well known [48], [61] that the truncation of the spectral integrals to the limit k_{mr} results in reconstructed scattered fields which are band-limited within the finite observation domain. Hence, their spatial-domain sampling can be performed at the Nyquist rate in order to avoid any aliasing error. If we assume that the bandwidth of the scattered field is roughly k_{mr}, i.e. the real part of the truncation limit, the Nyquist rate is given by

$$\Delta x = \frac{\pi}{k_{mr}} \tag{6.36}$$

Conversely, the spectral-domain Green's function $\tilde{G}$ is not a band-limited function since its Fourier transform, i.e. the spatial-domain Green's function $G(r)$, decays slowly at rate $1/r$ within the infinite observation plane. Hence, the Nyquist rate for the spectral discretization cannot be defined and does not exist. Particularly, the use of $\Delta k = \pi/L/2$ along with a low contour height ak was experimentally observed to produce high error levels ($\epsilon \approx 10^{-1}$) since $\tilde{G}$ becomes singular around k. If one wants to achieve

lower errors, the sampling step Δk must be determined with the sampling rules derived in the previous chapter.

In contrast to CFFT and USFLT, the CZT is a purely algebraic method dedicated to linear contours and only requires the computation of 3 FFT's. Its contour slope a can be chosen to minimize the number of IPW's and thus also its computational cost. In addition, it was demonstrated in Chapter 2 that linear contour deformations provide an efficient field representation for $z \gg \lambda$. Hence, the CZT seems to be the most suitable algorithm when the distance is much larger than the wavelength.

When the fields are evaluated at distances much lower than the wavelength, i.e. $z \ll \lambda$, the CFFT and USFLT algorithms are more relevant since they allow the use of a contour returning to the real axis. The CFFT is subject to the same restrictions as those of the FFT, i.e. (6.36) and $N = P$. As discussed earlier, selecting $\Delta k = \pi/L/2$ leads to a poor accuracy at the sides of the observation domain. The first way to overcome this potential issue is to evaluate G over an extended domain of size χL where the excess factor $\chi \geq 2$ is a power of 2, as done in [47], [61]. This comes at the price of computing larger FFTs. The other solution consists of increasing the contour height ak to get away from the free-space singularity. But, since the expansion order T increases with ak, this forces us to compute more FFTs. In comparison, the USFLT requires the computation of a single oversampled FFT of size $2N_x \times 2N_x$ which is not linked to the sampling step Δk. Hence, the USFLT is potentially faster than the CFFT if the cost of its convolution can be made negligible compared to that of the FFT. Hence, we have considered an example with an observation plate of growing width L for $z = 0.5\lambda$. The contour height ak has been selected according to the near field rules of Chapter 2 in order to minimize $(2M+1)^2P$. One can see in Fig. 6.8 that the theoretical number of operations of the convolution ($(2M+1)^2P$) is lower than that of the FFT ($4c_1 N \log_2 N$). Hence, time savings can be expected w.r.t. CFFT.

6.5 Extension to the vectorial problem

In this section, we will evaluate vector fields scattered by current distributions given on a source plate within an observation plate using the fast

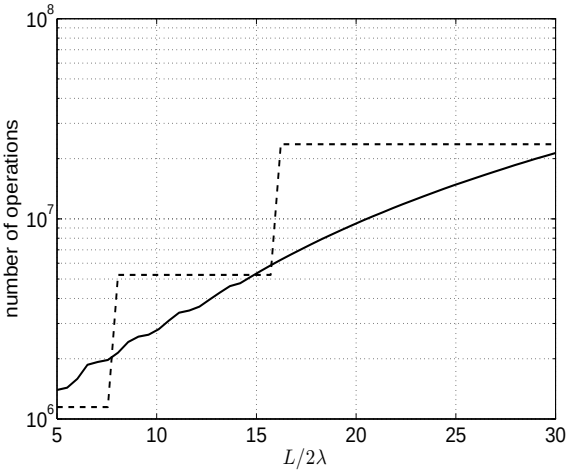

Figure 6.8: Optimal values of $(2M+1)^2P$ (solid) and of $4c_1N\log_2 N$ (dashed) for $\epsilon = 10^{-2}$, $k_{mr} = 2k$ and $z = 0.5\lambda$.

algorithms. This basic scenario can be encountered when computing the interactions between sub-domains in a Method-of-Moment analysis of planar structures, such as buildings [17], or the transmittance between aperture antennas [120].

6.5.1 Mathematical formulation

First, let us define three systems of coordinates (CS) which are illustrated in Fig. 6.9:

- $(\hat{\mathbf{x}}^s, \hat{\mathbf{y}}^s, \hat{\mathbf{z}}^s)$ is centred on the source plane with its z-axis oriented along the normal.
- $(\hat{\mathbf{x}}^o, \hat{\mathbf{y}}^o, \hat{\mathbf{z}}^o)$ is centred on the observation plane with its z-axis oriented along the normal.
- $(\hat{\mathbf{x}}, \hat{\mathbf{y}}, \hat{\mathbf{z}})$ is centred on the source plane with its z-axis oriented toward the center of the observation plane.

The first two CS are respectively used to compute the complex patterns and evaluate the scattered fields from their PWS on the observation plate. The

discretization of the spectral integral is performed in the third CS according to the methodology presented in the conclusion of Chapter 2.

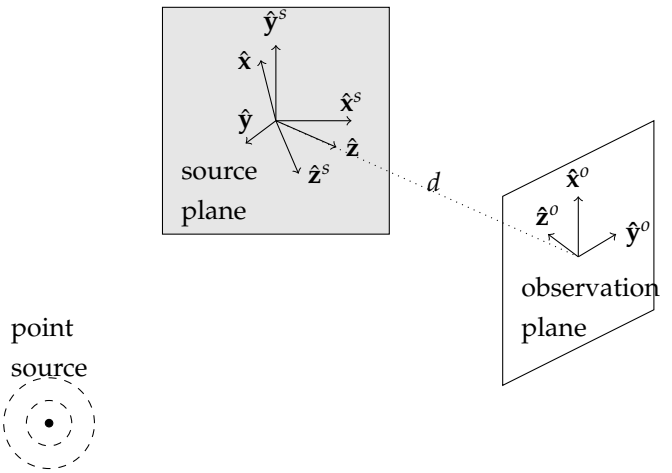

Figure 6.9: Geometry and local CS used for the computation of fields scattered from a source plate over a virtual observation plate when illuminated by a point source.

The fast transforms of Section 6.4 and Section 6.3 can be directly implemented to evaluate scattered vector fields after re-expressing the $\mathbf{k} \cdot \mathbf{r}$ exponent of the plane wave in the observation CS $(\hat{\mathbf{x}}^o, \hat{\mathbf{y}}^o, \hat{\mathbf{z}}^o)$.

$$e^{-j\mathbf{k}\cdot\mathbf{r}} = e^{-jk_{z,pq}d - jk^o_{x,pq}x^o - jk^o_{y,pq}y^o} \tag{6.37}$$

where d is the distance between the centers of the source and observation CS and the superscript o stands for variables expressed in the observation CS. Using a rotation matrix $\mathbf{R}^o$, defined in Appendix 3.6.3, to pass from $(\hat{\mathbf{x}}, \hat{\mathbf{y}}, \hat{\mathbf{z}})$ to $(\hat{\mathbf{x}}^o, \hat{\mathbf{y}}^o, \hat{\mathbf{z}}^o)$, we have $\mathbf{k}^o = \mathbf{R}^o \cdot \mathbf{k}$. Using the same notations as in Chapter 2, the electrical field is computed with

$$\begin{aligned} \mathbf{E}^d(\mathbf{r}_{mn}) &= \sum_p \sum_q w_{pq}\, \tilde{\mathbf{E}}(\mathbf{k}_{pq})\, e^{-jk_{z,pq}d}\, e^{-jk^o_{x,pq}x^o_m - jk^o_{y,pq}y^o_n} \\ &= USFLT\{w_{pq}\, \tilde{\mathbf{E}}(\mathbf{k}_{pq})\, e^{-jk_{z,pq}d}\} \end{aligned} \tag{6.38}$$

where w_{pq} is the spectral weight. The computation of the field PWS, expressed in terms of a complex Fourier transform of the current distribu-

tion over the source domain (2.18), can also be accelerated by rewriting the plane waves into the CS $(\hat{\mathbf{x}}^s, \hat{\mathbf{y}}^s, \hat{\mathbf{z}}^s)$ attached to the source plate,

$$\begin{aligned}\tilde{\mathbf{J}}(\mathbf{k}_{pq}) &= \Delta x^2 \sum_m \sum_n \mathbf{J}(\mathbf{r}_{mn})\, e^{jk^s_{x,pq}x^s_m + jk^s_{y,pq}y^s_n} \\ &= \Delta x^2\, USFLT^{-1}\{\mathbf{J}(\mathbf{r}_{mn})\}\end{aligned} \tag{6.39}$$

where the inverse transforms of the USFLT has been developed in Appendix 6.8.2 based on [23].

6.5.2 Arbitrarily oriented source and observation plates

The case of arbitrary oriented source and observation plates has not been addressed and is more difficult. Indeed, even though the plane waves are placed on a regular grid with a linear contour in $(\hat{\mathbf{x}}, \hat{\mathbf{y}}, \hat{\mathbf{z}})$, the corresponding spectral samples rotated in $(\hat{\mathbf{x}}^o, \hat{\mathbf{y}}^o, \hat{\mathbf{z}}^o)$ are generally non-uniformly spread over the complex plane. This concept is illustrated in Fig. 6.10. The USFLT is the only one of the three presented algorithms able to directly deal with spectral samples having irregularly-spaced real and imaginary parts.

If we assume that the CS $(\hat{\mathbf{x}}^o, \hat{\mathbf{y}}^o, \hat{\mathbf{z}}^o)$ attached to the observation plate is rotated with angles ϕ and θ w.r.t. to $(\hat{\mathbf{x}}, \hat{\mathbf{y}}, \hat{\mathbf{z}})$, we can expand the rotation matrix $\mathbf{R}^o$, defined in Appendix 3.6.3, in spherical coordinates to have

$$\begin{pmatrix} k^o_x \\ k^o_y \\ k^o_z \end{pmatrix} = \begin{pmatrix} \sin\theta\cos\phi & \cos\theta\cos\phi & -\sin\phi \\ \sin\theta\sin\phi & \cos\theta\sin\phi & \cos\phi \\ \cos\theta & -\sin\theta & 0 \end{pmatrix} \begin{pmatrix} k_x \\ k_y \\ k_z \end{pmatrix} \tag{6.40}$$

From there, one can deduce that the irregular pattern of k^o_x and k^o_y results from a rotation which sum up regularly-spaced samples k_x and k_y with a non-linear function $k_z = (k^2 - k_x^2 - k_y^2)^{1/2}$. As an extension of results [110] to three dimensions, we have proven in Appendix 6.8.3 that k^o_x and k^o_y satisfy the following inequalities for any rotation angles,

$$\begin{aligned}\frac{k^{o2}_{xr}}{||\mathbf{k}_r||^2} + \frac{k^{o2}_{xi}}{||\mathbf{k}_i||^2} &\leq 1 \\ \frac{k^{o2}_{yr}}{||\mathbf{k}_r||^2} + \frac{k^{o2}_{yi}}{||\mathbf{k}_i||^2} &\leq 1\end{aligned} \tag{6.41}$$

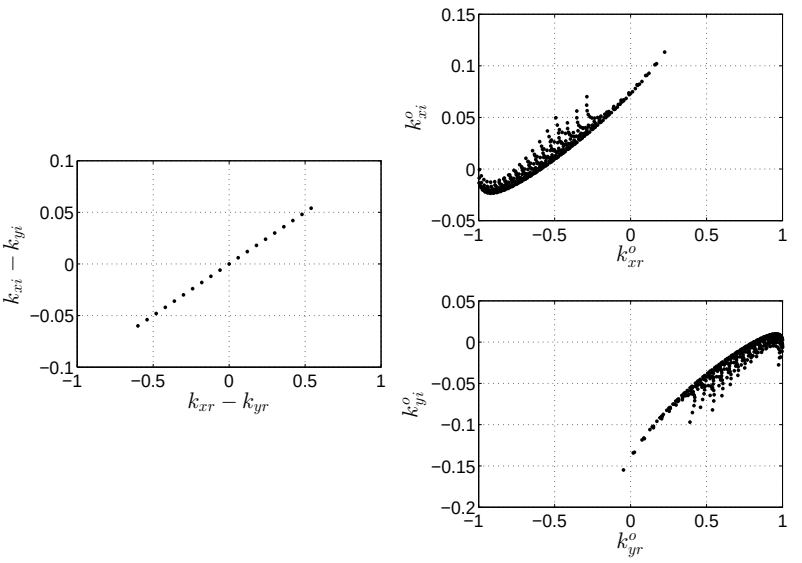

Figure 6.10: Illustration of the rotation of IPW samples due to the change of CS from $(\hat{\mathbf{x}}, \hat{\mathbf{y}}, \hat{\mathbf{z}})$ to $(\hat{\mathbf{x}}^o, \hat{\mathbf{y}}^o, \hat{\mathbf{z}}^o)$.

where the direction of propagation $\mathbf{k}_r = k_{xr}\hat{\mathbf{x}} + k_{yr}\hat{\mathbf{y}} + k_{zr}\hat{\mathbf{z}}$ and the direction of evanescence $\mathbf{k}_i = k_{xi}\hat{\mathbf{x}} + k_{yi}\hat{\mathbf{y}} + k_{zi}\hat{\mathbf{z}}$ are perpendicular to each other. The relations (6.41) could be used to parametrize the USFLT for interactions at arbitrary angles given a maximum value of k_{mr} and indicate that the boundary of the locus of (k^o_{xr}, k^o_{xi}) and of (k^o_{yr}, k^o_{yi}) is an ellipse of semi-axes $||\mathbf{k}_r||$ and $||\mathbf{k}_i||$.

6.5.3 Small-scale height variation

Let us now assume that the source plate contains electrically small features and becomes slightly indented. In this case, we can define the height profile $z^s = h^s(x^s, y^s)$ of the surface expressed in the CS $(\hat{\mathbf{x}}^s, \hat{\mathbf{y}}^s, \hat{\mathbf{z}}^s)$. One must taken into account this height variation when computing the complex patterns. Precisely, the exponential in (6.39) must be replaced by

$$e^{j\mathbf{k}\cdot\mathbf{r^s}} = e^{jk^s_x x^s + jk^s_y y^s + jk^s_z h^s(x^s, y^s)} \tag{6.42}$$

When the maximum height is small compared to the wavelength, i.e. $|h^s| \ll \lambda$, the factor $e^{jk_z^s h^s}$ can be efficiently approximated with a low-order Taylor series. This yields

$$e^{j\mathbf{k}\cdot\mathbf{r^s}} = e^{jk_x^s x^s + jk_y^s y^s} \sum_{t=0}^{T} \frac{(jk_z^s h^s(x^s,y^s))^t}{t!} \tag{6.43}$$

where T is the expansion order of the Taylor series. Then, we can insert (6.43) into (6.39) and swap the sums s.t. we have

$$\tilde{\mathbf{J}}(\mathbf{k}_{pq}) = \Delta x^2 \sum_{t=0}^{T} \frac{(jk_{z,pq}^s)^t}{t!} \sum_m \sum_n h^s(x_m^s, y_n^s)^t \, \mathbf{J}(\mathbf{r}_{mn}) \, e^{jk_{x,pq}^s x_m^s + jk_{y,pq}^s y_n^s} \tag{6.44}$$

It is clear from (6.44) that the complex pattern of the induced current on the indented surface can be still rapidly computed with

$$\tilde{\mathbf{J}}(\mathbf{k}_{pq}) = \Delta x^2 \sum_{t=0}^{T} \frac{(jk_{z,pq}^s)^t}{t!} \, USFLT^{-1}\{h^o(x_m^s, y_n^s)^t \, \mathbf{J}(\mathbf{r}_{mn})\} \tag{6.45}$$

Similarly, when the observation plate is not perfectly planar, the scattered field can be approximated with

$$\mathbf{E}^d(\mathbf{r}_{mn}) = \sum_{t=0}^{T} \frac{j^t h^o(x_m^o, y_n^o)^t}{t!} \sum_p \sum_q w_{pq} \, (k_{z,pq}^o)^t \, \tilde{\mathbf{E}}(\mathbf{k}_{pq}) \, e^{-jk_{z,pq}d} \, e^{-jk_{x,pq}^o x_m^o - jk_{y,pq}^o y_n^o} \tag{6.46}$$

and rapidly evaluated through

$$\mathbf{E}^d(\mathbf{r}_{mn}) = \sum_{t=0}^{T} \frac{j^t h^o(x_m^o, y_n^o)^t}{t!} \, USFLT\{w_{pq} \, (jk_{z,pq}^o)^t \, \tilde{\mathbf{E}}(\mathbf{k}_{pq}) \, e^{-jk_{z,pq}d}\} \tag{6.47}$$

It is important to recall that $|k_z h|$ should be much lower than 1 in order to keep the expansion order T low and thus this algorithm efficient.

6.6 Numerical results

In the following examples, a point source illuminates a source plate with a magnetic field $\mathbf{H}^i$, as sketched in Fig. 6.9. The current impressed on

the PEC plate is then approximated with physical optics (PO),

$$\mathbf{J}^{po}(\mathbf{r}) = 2\,\hat{\mathbf{n}} \times \mathbf{H}^{i}(\mathbf{r}) \tag{6.48}$$

A comparison will be carried out between back-scattered fields computed on the observation plate with the accelerated USLFT-based spectral method and with a spatial-domain integration of the radiation integral using a rectangle rule and N sample points. The mesh size is set to $\lambda/4$. This is typically chosen when computing multiple scattering interactions and is driven by the oscillation of radiated fields at period λ. It is important to mention that the highly oscillatory behaviour of the scattered fields will not be reflected though the following figures which only illustrate the field magnitude $(\mathbf{E}^s \cdot \mathbf{E}^{s\star})^{1/2}$. The relative error will be computed numerically through (3.29) in which $\mathbf{E}^d$ corresponds to the field reconstructed with the fast method. The magnitude of the error contains all relevant information. Indeed, a low error magnitude guarantees that both the real and the imaginary parts of the exact field value are reconstructed to the target accuracy. The simulations are carried out using a PC with 16 GB RAM and Processor Intel (R) Core(TM) i5-3570 CPU @ 3.4 GHz.

6.6.1 Example 1 : Parallel plates

First, we consider the case of parallel source and observation plates separated by a distance much larger than the wavelength $d \gg \lambda$. Under these conditions, one can infer that linear contours provide an efficient field representation and that the CS's can be chosen to coincide with $(\hat{\mathbf{x}}, \hat{\mathbf{y}}, \hat{\mathbf{z}})$. Hence, the CZT can be applied to accelerate (6.38) and (6.39). The inverse CZT is easily obtained by reversing the sign of the exponent of W and by interchanging P_x and N_x in (6.22). A comparison is made with a spatial-domain integration which benefits from the separability of the $k_x - k_y$ spectral integrals for linear contours, as discussed in Section 6.4.

The two examples, presented in Fig. 6.11, correspond to near fields ($d = 2\lambda$) and intermediate fields ($d = 10\lambda$) for plates of width $L = 10\lambda$ illuminated by a point source located at $\mathbf{r}_i = 5\lambda\hat{\mathbf{z}}^s$ and $\mathbf{r}_i = \lambda\hat{\mathbf{z}}^s$, respectively. One can infer from those figures that the relative errors are below the target accuracy $\epsilon_{tar} = 10^{-2}$. The computation times associated with

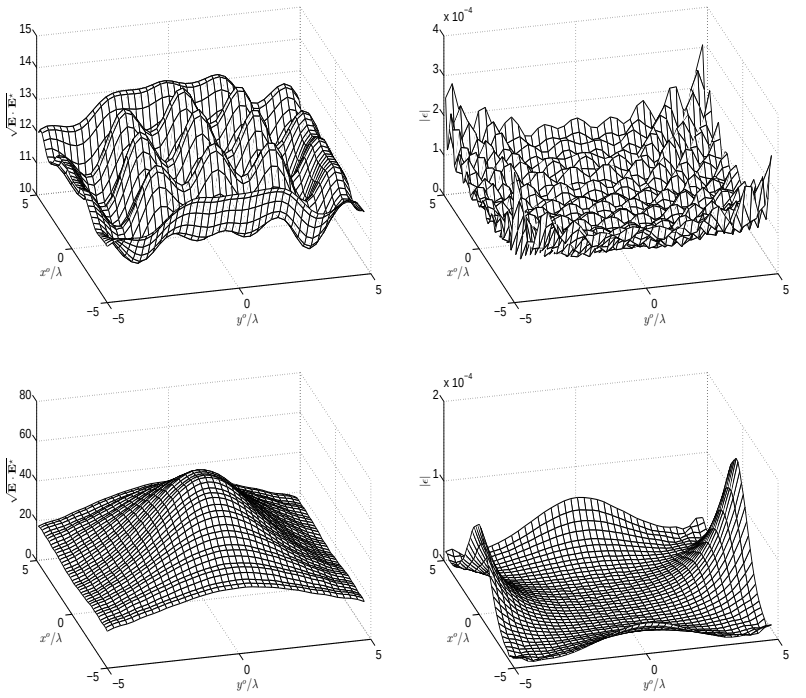

Figure 6.11: Magnitude of the scattered field (left) and relative error (right) using CZT for $\mathbf{r}_i = 5\lambda\hat{\mathbf{z}}^s$, $d = 10\lambda$, $L = 10$, $nk = 52$, $N = 40$ and $a = 0.2$ (top) and for $\mathbf{r}_i = \lambda\hat{\mathbf{z}}^s$, $d = 2\lambda$, $L = 10$, $nk = 56$, $N = 40$ and $a = 0.1$ (bottom).

the CZT and with the spatial-domain methods are, for both cases, roughly 0.06 and 0.7 seconds, respectively.

6.6.2 Example 2 : Tilted plates

First, we consider the scenario shown in Fig. 6.12 containing two tilted observation plates rotated perpendicularly w.r.t. the source plate. The length is set to $L = 20\lambda$ and the point source is located at $\mathbf{r}_i = 5\lambda\hat{\mathbf{z}}^s$.

As one can see in Fig. 6.13, the field evaluated with the fast method on the observation plates 1 and 2 are reconstructed down to the target accuracy $\epsilon = 10^{-2}$. For plate 1, the number of plane waves, the number of spatial samples and the window width are, respectively, $P = 46^2$, $N = 128^2$

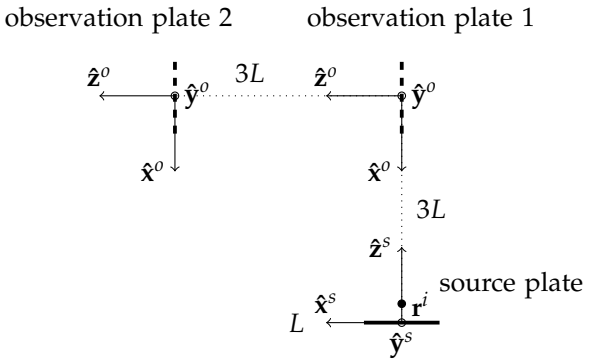

Figure 6.12: Scattering scenario: fields are computed from a source plate (solid) over perpendicular observation plates (dashed).

and $M = 6$. The computation times for the spatial-domain integration and for the fast USFLT-based method are 30 sec and 0.2 sec, respectively. For plate 2, the number of plane waves, the number of spatial samples and the window width are, respectively, $P = 36^2$, $N = 128^2$ and $M = 6$. The computation times are, respectively, 31 sec and 0.19 sec for the two methods.

In order to assess the performance of the USFLT approach, we progressively increase the parameter L. This means that the size of the source and observation plates as well as the relative distance between them grows linearly. The computation time has been decomposed into that required to compute the convolution and that to perform the FFT's of the USLFT method. In view of the results shown in Fig. (6.14), one can infer that the time spent performing the convolutions in the USFLT method is around 2 times that spent by the FFTs. Hence, we can conclude that this fast method exhibits a $N \log_2 N$ asymptotic computational complexity and that its computation time is almost to that of the Fastest Fourier Transform in the West (FFTW) [111], the FFT library used by Matlab [112].

6.6.3 Example 3 : Random rough plates

The geometry is the same as that of Example 2, sketched in Fig. 6.12, considering only the observation plate 1. In this example, the source and the observation plates are now Gaussian-distributed and exponentially-correlated random rough surfaces. Their rms value and correlation length

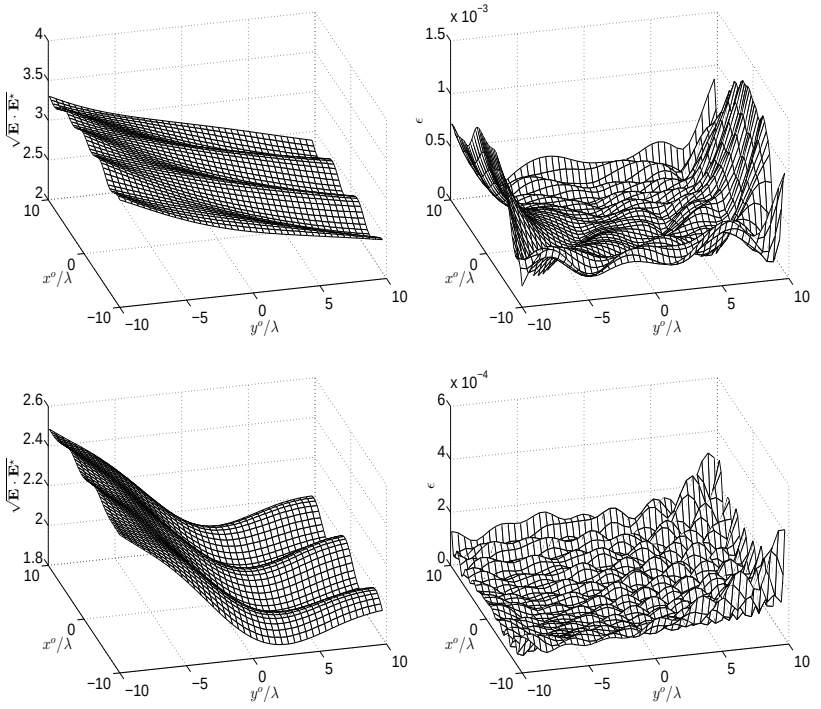

Figure 6.13: Magnitude of the scattered field (left) and relative error (right) using USFLT for the observation plate 1 (top) and 2 (bottom).

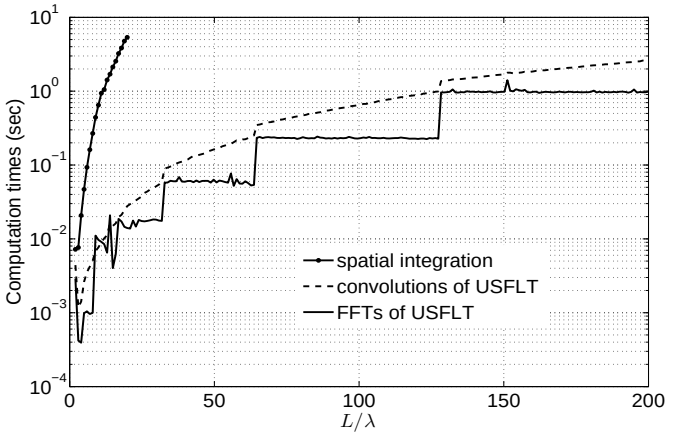

Figure 6.14: Computation times of the convolutions (dashed) and of the FFT's (dashed) required by the USFLT-based method and of the brute-force spatial domain integration (solid-dot) for the scenario in Fig. 6.12.

are set to $\lambda/10$ and 2λ, respectively, s.t. the induced current can be fairly approximated using the PO approximation [113], [114]. The height profiles are illustrated in Fig. 6.15. As shown in Fig. 6.18, a truncation order $T = 3$ of the Taylor series is sufficient to reconstruct the scattered field down to 2 digits of accuracy. This means that the complex patterns and the scattered fields are each computed rapidly with (6.45) and (6.47) using 4 USFLT's. One should also investigate other scattering models from rough surfaces, as presented in [115], [116], [117], which directly use the power spectral density (PSD) of the randomly-distributed height profile.

6.6.4 Example 4 : Radio propagation in a canyon

In this example, the geometry, sketched in Fig. 6.17, resemble a narrow urban street. A Tx transmitter first illuminates the bottom plate $plate1$. Then, we compute the electric field at Rx receivers, lying along the observation path (dashed), resulting from the double scattering interactions $Tx - plate1 - plate2 - Rx$ and $Tx - plate1 - plate3 - Rx$. The size of the plates is set to $L = 40\lambda$ s.t. they correspond to building facades of few meters wide at 1.8 GHz. The relative position of the source, the plates and the observation path are detailed in Fig. 6.17.

The computation of the field scattered on the observation plates $plate1$ and $plate2$ from the currents lying on $plate1$ is the most computationally intensive part and can be accelerated with the USFLT-based method. In Fig. 6.18, we have plotted the magnitude of the electric field resulting from the double interactions computed with USFLT (solid) and with the brute-force spatial-domain integration (dots). In the top sub-figure, the faces are considered flat. In the bottom sub-figure, we have included a roughness of rms height $\lambda/20$ and of correlation length 2λ. The Taylor series in (6.45) and in (6.47) is truncated to $T = 4$. In both cases, one can observe that the field is reconstructed accurately with the fast method. For a single Rx receiver, the computation time of the USFLT method is 0.4 sec for flat surfaces and 2.2 sec for rough surfaces. The brute force integration takes 13 min for both type of surfaces. By comparing the two sub-figures, one can note that the small-scale roughness seems to produce strong deviations in the magnitude of the electric field.

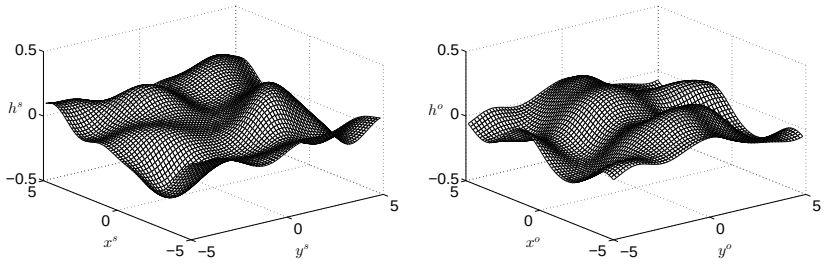

Figure 6.15: Height profiles $z^s = h^s(x^s, y^s)$ and $z^o = h^o(x^o, y^o)$ of the source (left) and the observation (left) rough surfaces.

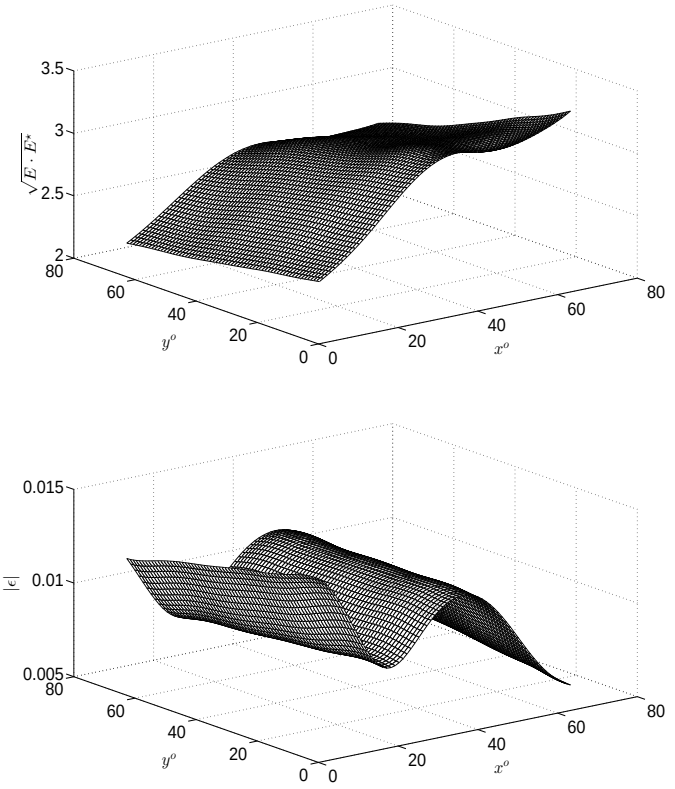

Figure 6.16: Magnitude of scattered field (top) and relative error (bottom) considering the scenario and the rough surfaces sketched in Fig.6.15 and in Fig. 6.15, respectively.

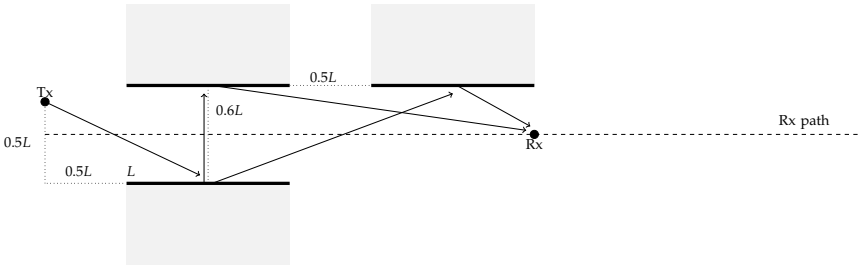

Figure 6.17: Double-scattering scenario in a narrow street for plates of size $L = 40\lambda$.

6.7 Conclusion

We have presented a fast algorithm based on the unequally-spaced fast Laplace transform (USFLT) [23] which allows us to combine a contour deformation technique and the FFT to accelerate, down to a $N \log N$ asymptotic complexity, the computation over an observation plate of fields scattered from current distributions lying on a source plate. Most importantly, we have demonstrated that the USFLT can also be used to accelerate the computation of radiation integrals between plates of arbitrary orientations and positions in intermediate- to far-field regions. Thanks to an error model derived in [23] and the sampling rules derived in Chapter 2, the parameters of the fast method are entirely determined with simple formulas which depend on the targeted error level and the critical dimensions of the geometry. Time savings of 1 and 2 orders of magnitude w.r.t. direct spectral-domain or spatial-domain integrations have been observed for plates of width 20λ when using a coarse mesh size of $\lambda/4$. At 1.8 GHz, one can simulate an entire building wall of few meters in one-tenth of a second. We have also proven that the source and observation plates do not need to be perfectly flat and can have a height profile which remains small compared to the wavelength. The fast method could also be easily extended to deal with penetrable surfaces by replacing the electric current with the equivalent magnetic and electric currents evaluated at the interface between the air and the dielectric material, as already presented in Chapter 3.

Two other existing fast techniques, namely the Contour-FFT (CFFT)

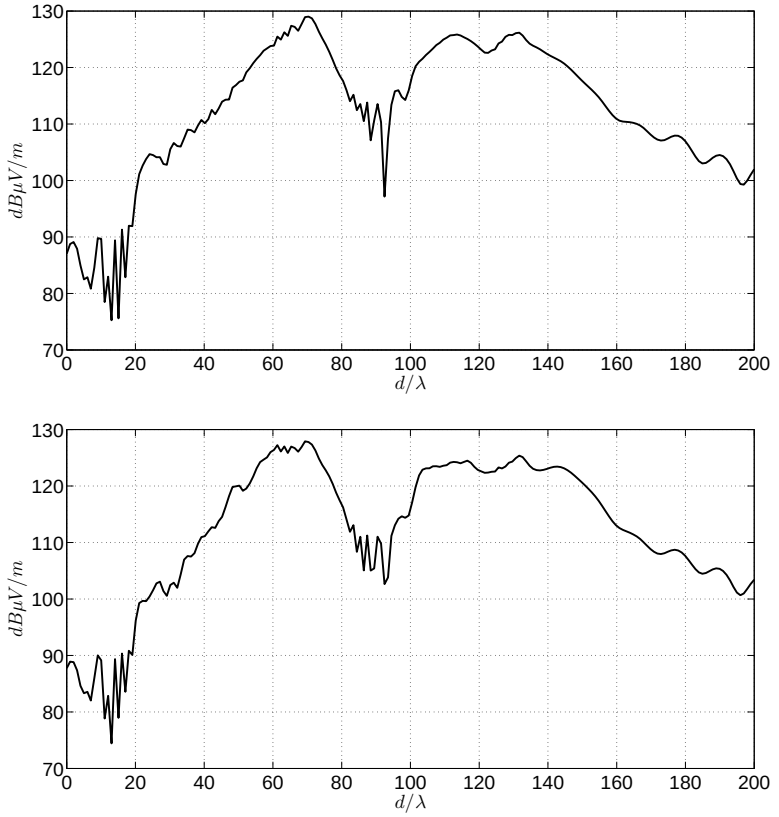

Figure 6.18: Magnitude of the electric field for the scenario shown in Fig. 6.17 when computed with the USFLT-based method (solid) and with the brute-force integration (dots) for flat (top) or rough (bottom) surfaces.

and the Chirp z-transform (CZT), have been presented and/or recalled along with their inverted error models and applied to the fast evaluation of scattered fields. It must be noted that those methods cannot deal with the case of tilted source and observation plates. Hence, a comparison with the USFLT has been carried out in the specific case when the observation domain is at a fixed distance z. When the distance is much larger than the wavelength $z \gg \lambda$, the CZT remains undoubtedly more efficient and simple than the USFLT. For smaller distances $z \ll \lambda$, the CFFT and USFLT are more relevant than CZT since they allow the use of a contour returning to the real axis. As opposed to the CFFT which requires the computation of

a series of FFT, the USFLT uses only one FFT. In addition, the constraints are relaxed since the number of spatial samples and the number of plane waves, i.e. the spectral samples, can be set different. Hence, an important factor speed-up w.r.t. the CFFT can be expected.

Typical applications are found in scattering problems involving electrically large (quasi-)planar structures standing in the near- to intermediate-field of each other. For instance, this is the case when simulating channels inside a city [17] or a building or when computing the transmittance between two aperture antennas [120]. In the context of the fast evaluation of matrix-vector products resulting from integral interactions between few sub-domains, the USFLT method could be used to compute the complex patterns or the scattered fields. In comparison, the Fast Multipole Method (FMM) requires the computation of a costly translation function which must be efficiently interpolated [105], [122] at high frequencies and the Adaptive Integral Method (AIM) utilizes three-dimensional FFTs [103]. Finally, the CZT and USFLT could be also used for the fast computation of the reaction integrals between parallel plates along with a Macro-Basis Functions approach [47] or with an iterative solver [61], as it was done for CFFT.

6.8 Appendices

6.8.1 Implementation of the classical FFT algorithm

Let us start from the discrete representation of the Green's function,

$$G(r_{mn}) = \frac{\Delta k^2}{4\pi^2} \sum_{p=-\frac{P_x}{2}}^{\frac{P_x}{2}-1} \sum_{q=-\frac{P_x}{2}}^{\frac{P_x}{2}-1} c_{pq}\, \tilde{G}(k_{\rho r,pq})\, e^{-j\Delta k\Delta x(pm+qn)} \tag{6.49}$$

Then, we can use the change of variables $p' = p + P_x/2$, $q' = q + P_x/2$, $n' = n + N_x/2$, $m' = m + N_x/2$ s.t. the sums start from 0,

$$G(r_{nm}) = \frac{\Delta k^2}{4\pi^2}\, W^{(N_x-n'-m')P_x/2} \sum_{p'=0}^{P_x-1} \sum_{q'=0}^{P_x-1} \tilde{G}(k_{\rho pq})\, W^{(-p'-q')N_x/2}\, W^{-p'n'-q'n'} \tag{6.50}$$

where $W = e^{j\Delta x \Delta k}$. Those sums respect the standardised form required to apply the FFT. A classical FFT also requires $P_x = N_x$ to be a power of 2 and $\Delta x \Delta k = 2\pi / N_x$. This leads to

$$\begin{aligned} \Delta x &= \frac{\pi}{k_{mr}} \\ L/2 &= \frac{\pi}{\Delta k} \end{aligned} \tag{6.51}$$

where $k_{mr} = P_x \Delta k / 2$ is the truncation limit and $L = N_x \Delta x$ is the maximum lateral half-extent of the observation domain. The relations (6.51) imply that L and Δx are automatically determined by the chosen values of Δk and k_{mr}. Finally, the number of basic operations performed when evaluating (6.50) with a FFT is given by $N_{op} \approx c_1 N \log_2 N$ with $c_1 \approx 5$ [119].

6.8.2 The inverse unequally-spaced fast Laplace transform

The inverse Fourier transform of the spatial Green's function is analytically given by

$$G(k_\rho) = \iint_{-\infty}^{\infty} G(r) e^{jk_x x + jk_y y} \, \mathrm{d}x \mathrm{d}y \tag{6.52}$$

Using a similar methodology as for the direct approach, it possible to demonstrate [23] that the inverse Fourier transform of the Green's function is equal to

$$\tilde{G}(k_\rho) = \frac{1}{4\pi^2} \iint_{-\infty}^{\infty} \tilde{F}(k'_x, k'_y) \, \tilde{\psi}(k_x - k'_x, k_y - k'_y) \, \mathrm{d}k'_x \mathrm{d}k'_y \tag{6.53}$$

with

$$\tilde{F}(k'_x, k'_y) = \iint_{-\infty}^{\infty} \frac{G(r)}{\psi(x,y)} \, e^{-jk'_x x - jk'_y y} \, \mathrm{d}x \mathrm{d}y \tag{6.54}$$

where the primed spectral coordinates k'_x and k'_y are real values. The discrete form can thus be written as

$$\begin{aligned} G(k_{\rho,pq}) &= \Delta x^2 \, USFLT^{-1}\{\tilde{G}(r)\} \\ &\triangleq \frac{\Delta x^2}{(\nu L)^2} \sum_u \sum_v \tilde{\psi}\left(k_{x,pq} - k'_{x,u}, k_{y,pq} - k'_{y,v}\right) \, \tilde{F}(k'_{x,u}, k'_{y,v}) \end{aligned} \tag{6.55}$$

where only $2M+1$ terms are kept in both sums, ν is the oversampling ratio and the FFT is performed over an oversampled $\nu N_x \times \nu N_x$ grid with

$$\tilde{F}\left(k'_{x,u}, k'_{y,v}\right) = FFT\{\frac{G(r_{mn})}{\psi(m\Delta x, n\Delta x)}\} \tag{6.56}$$

The parameters M and ν can still be selected with (6.17) and (6.16).

6.8.3 Locus of the rotated spectral variables

From (6.40), we can write

$$\begin{aligned} k^o_{xr} &= \sin\theta\cos\phi k_{xr} + \cos\theta\cos\phi k_{yr} - \sin\phi k_{zr} \\ k^o_{xi} &= \sin\theta\cos\phi k_{xi} + \cos\theta\cos\phi k_{yi} - \sin\phi k_{zi} \end{aligned} \tag{6.57}$$

Then, it is possible to isolate the following quantities through simple algebraic operations,

$$\begin{aligned} \cos\theta\cos\phi &= \frac{(k_{xi}k_{zr} - k_{xr}k_{zi})\sin\phi + k_{xi}k^o_{xr} - k_{xr}k^o_{xi}}{k_{xi}k_{yr} - k_{xr}k_{yi}} \\ \sin\theta\cos\phi &= \frac{(k_{yi}k_{zr} - k_{yr}k_{zi})\sin\phi + k_{yi}k^o_{xr} - k_{yr}k^o_{xi}}{k_{xr}k_{yi} - k_{xi}k_{yr}} \end{aligned} \tag{6.58}$$

Summing the square of those equations allows to get rid of θ,

$$\begin{aligned} &(k_{xr}k_{yi} - k_{xi}k_{yr})^2\cos^2\phi - ((k_{xi}k_{zr} - k_{xr}k_{zi})\sin\phi + k_{xi}k^o_{xr} - k_{xr}k^o_{xi})^2 \\ &- ((k_{yi}k_{zr} - k_{yr}k_{zi})\sin\phi + k_{yi}k^o_{xr} - k_{yr}k^o_{xi})^2 = 0 \end{aligned} \tag{6.59}$$

This equation defines a set of quadratic curves for each value of ϕ. The envelope of those curves is obtained by cancelling the derivative w.r.t. ϕ and by isolating $\sin\phi$. Then, this root can then be reinserted in (6.59). Knowing that $\mathbf{k}_r \cdot \mathbf{k}_i = 0$ with $\mathbf{k}_r = k_{xr}\hat{\mathbf{x}} + k_{yr}\hat{\mathbf{y}} + k_{zr}\hat{\mathbf{z}}$ and $\mathbf{k}_i = k_{xi}\hat{\mathbf{x}} + k_{yi}\hat{\mathbf{y}} + k_{zi}\hat{\mathbf{z}}$, we can easily show that the calculations lead to

$$\frac{k^{o2}_{xr}}{||\mathbf{k}_r||^2} + \frac{k^{o2}_{xi}}{||\mathbf{k}_i||^2} = 1$$

The same relation can be obtained for (k^o_{yr}, k^o_{yi}) with a similar development.

Conclusion

7

The guideline of this thesis was the development of a method based on the numerical evaluation of the radiation integral of Physical Optics for the simulation of urban radio propagation. Such deterministic tool can be used to accurately characterize radio channels. Even-though the computations become frequency- and excitation-dependent as compared to ray-tracers, we may expect more accurate simulation results since the truncation effect due to the finite dimension of scatterers is better represented with the surface radiation integral rather than by considering explicit edge or corner contributions. Compared to high-frequency ray representations, the numerical evaluation of the PO radiation integral is beneficial :

- It is self-contained since the edge, corner and higher-order asymptotic contributions are inherently taken into account by a single radiation integral.
- The scattered field is uniform, continuous and finite everywhere in space.
- Shadowing is inherently produced by summing the incident field and the field scattered behind a plate.
- The generalization to multiple scattering interactions is trivial.

However, it may seem less convenient for users :

- The simulations must be rerun when modifying the antenna pattern of the transmitter or the simulated frequency.

- The computation time is much higher and increases faster than quadratically with the frequency.
- The channel impulse response must be computed from the inverse Fourier transform of the transfer function simulated over a given frequency bandwidth.
- The power angular spectrum must be computed from the inverse Fourier transform of the fields over a virtual plate centred on a given observation point.

Nevertheless, we have shown that neglecting the corner- and edge-contributions within single or multiple scattering interactions, as done by many ray-tracers, can be strongly inaccurate and fails to provide the correct angular dependence and the $1/R$ decay of the scattered fields from distances above the size of the source domain.

Besides, we analysed the field error resulting from the PO approximation of the induced current. We have shown analytically for the PEC wedge and numerically for the PEC plate that the PO field is highly accurate within and around the regions of specular reflection. To further improve the field accuracy outside this region, one can add fringe-wave equivalent currents lying on the rim of the plate which have been developed in the framework of the Physical Theory of Diffraction.

Radio-coverage tools based on the computation of the PO radiation integrals were already developed in [20], [64]. However, the mentioned computation times are found already high for the simulation of a small two-dimensional problem in [20] or at low frequencies in [64]. At GHz frequencies, the building walls are few tens of wavelength wide and the numerical integration of highly oscillating currents will be unaffordable when computed in brute force. Hence, this thesis mainly focussed on the development of fast computational methods which intrinsically benefit from the geometrical representation of cities with electrically large planar facets.

In the proposed method, the shadowing results from a compensation between incident fields and scattered fields. In practice, this means that each pair of plates in the geometry can interact. This will be time-consuming in large urban environments. In order to decrease the computation costs, we can neglect the interactions between pair of plates which

do not lie nearby the region illuminated by GO reflections. To do so, the determination of the lit polygons has been accelerated using a three-step fast method based on a Binary Space Partitioning (BSP) representation of the geometry. This brings down the computational complexity for finding the lit surfaces from a given view-point from quadratic $O(N_f^2)$ to linear $O(N_f)$ with N_f the number of facets in the scene. It was shown numerically that the visibility computations up to 2 reflections are performed in matter of minutes even for a large urban environment.

Then, in order to accelerate the numerical computation of a single interaction, we have developed fast methods based on an inhomogeneous plane-wave (IPW) decomposition of the PO radiation integral.

The first challenge consisted of automatically controlling the error produced by the IPW decomposition down to a targeted level ϵ for large source and observation domains of arbitrary lateral extends ρ and relative distances z. Hence, we derived sampling rules for an IPW expansion based on a parametrizable linear contour which is well suited to scattering problems in which interacting groups are visible from each other within a limited angular sector. The resulting number of plane waves is around 4 times the degrees of freedom (DoF) of scattered fields [22]. We used those sampling rules throughout the whole manuscript. They could also help to accelerate the evaluation of intermediate fields in fast Method-of-Moments based on IPWs, such as FIPWA [27] or HIPWA [21], or in the context of the Spectral Theory of Diffraction [62].

Then, within the framework of the Spectral-domain Physical Optics (SPO), we proved that the plane-wave spectrum (PWS) of the Physical Optics (PO) field is given analytically considering a single incident IPW. This allowed us to directly express the scattered PWS in terms of the incident one and perform the calculations entirely in the spectral domain without any spatial mesh. The SPO thus benefits from the decreasing number of IPWs with the field of view between source and observation plates. However, the speed-up w.r.t. a brute-force spatial-domain integration decreases when the interacting plates are closer to each other. This method will not provide sufficient speed-ups to simulate a moderate size city at GHz frequencies.

We thus have presented another fast algorithm based on the unequally-spaced fast Laplace transform (USFLT) [23] which allows us to combine the simplicity of the IPW decomposition with the efficiency of an FFT to accelerate, down to a $N \log N$ asymptotic complexity, the computation of radiation integrals between arbitrarily orientated source and observation plates in intermediate- to far-field regions. Numerical results for plates of arbitrary orientations and positions in intermediate-field regions have shown important speed-up compared to both spectral-domain and spatial-domain integrations. Precisely, the computation time for a single interaction between two faces of length $L = 10m$ at $2GHz$ ($L = 50\lambda$) has been reduced to one-tenth of a second with the USFLT-based method. With this acceleration, one may expect the simulation at few GHz frequencies of urban radio propagation with the PO radiation integral to be carried out in matters of minutes.

In this thesis, we only analysed examples with plates separated by a distance higher than their half-width. Even if we have experimentally observed that the fast method still works until much smaller distances, it appears to break down at a certain near-field limit. This issue is critical for the fast computation of dihedral interactions. A trivial solution could first consist of taking the images of the current points on the first plate through the second plate.

Otherwise, we have also explain how we can extend the fast method to deal with plates having a small-scale height profile without much decreasing its efficiency. This could be help to model the effect of small features on the surface, e.g. brick walls or windows, or of the diffuse scattering using random roughness with PO or with Small Perturbation Method (SPM) [115]. In addition, one can easily deal with penetrable surfaces by using equivalent currents lying at the air-material interface. In this context, the fast USFLT-based simulation of a facet containing many features (wood, glass, brick) with a small height variation should be investigated.

In a broader framework, other typical applications of the USFLT-based method are found in scattering problems involving electrically large planar structures standing in the near- or far-field of each other. In particular, when evaluating matrix-vector products in integral equation solvers, the USFLT method could be used to compute the complex patterns or the scat-

tered fields with a single two-dimensional FFT. In comparison, the Fast Multipole Method (FMM) requires the computation of a costly translation function at high frequencies and the Adaptive Integral Method (AIM) utilizes three-dimensional FFTs [103]. Finally, it could also accelerate the computation of reaction integrals between parallel plates along with a Macro-Basis Functions approach [47] or with an iterative solver [61], as it was done for the CFFT [47].

List of Publications

Journal Papers

[J1] **Q. Gueuning**, C. Craeye, and C. Oestges, "**Sampling Rules for an Inhomogeneous Plane-wave Representation of Scattered Fields**", *IEEE Transactions on Antennas and Propagation*, in press.

[J2] Y. Miao, **Q. Gueuning**, and C. Oestges, "**Modeling the Phase Correlation of Effective Diffuse Scattering From Surfaces for Radio Propagation Prediction With Antennas at Refined Separation**", *IEEE Transactions on Antennas and Propagation*, vol. 66, no. 3, March 2018.

[J3] H. Bui-Van, J. Abraham, M. Arts, **Q. Gueuning**, C. Raucy, D. Gonzalez-Ovejero, E. de Lera Acedo, and C. Craeye, "**Fast and Accurate Simulation Technique for Large Irregular Arrays**", *IEEE Transactions on Antennas and Propagation*, vol. 66, no. 4, April 2018.

Conference Papers

[C1] **Q. Gueuning**, C. Craeye, and C. Oestges, "**Inhomogeneous plane wave spectrum based Physical Optics**", *International Conference on Electromagnetics in Advanced Applications (ICEAA)*, Turin, Italy, 2015.

[C2] **Q. Gueuning**, S. Hubert, C. Craeye, and C. Oestges,, "**Error model for Contour-FFT evaluation of the free-space on-plane Green's function**", *International Symposium on Electromagnetic Theory*, Espoo, Finland, 2016.

[C3] **Q. Gueuning**, C. Craeye, and C. Oestges, "**nequally-spaced fast Laplace transform for Green's function evaluation**", *International Symposium on Electromagnetic Theory*, Espoo, Finland, 2016.

[C4] **Q. Gueuning**, E. de Lera Acedo, E. Colin-Beltran, and C. Craeye, "**Mutual coupling analysis of large irregular arrays: From multipole to interpolatory methods**", *European Conference on Antennas and Propagation (EuCAP)*, Lisbon, Portugal, 2015.

[C5] **Q. Gueuning**, C. Craeye, and C. Oestges, "**A Stable Representation of the Transmittance Between Identical Circular Apertures**", *URSI Atlantic Radio Science Meeting (AT-RASC)*, Meloneras, Spain, June 2018.

Bibliography

[1] A. M. Coffman, and K. G. Odlyzko, *Internet Growth: Is There a Moore Law for Data Traffic*, Springer US, 2002, pp. 47-93.

[2] N. Khan, *Multi-Link Channel Modeling and Interference Characterization for Beyond 4G Networks*, Université Catholique de Louvain, 2014.

[3] The GSMA WRC Series, 'The GSMA WRC Series - getting ready for WRC-19', Nov. 2018, [Online]. Available: `https://www.gsma.com/spectrum/wrc-series`.

[4] European Conference of Postal and Telecommunications Administrations, 'Spectrum for wireless broadband - 5G', Nov. 2018, [Online]. Available: `https://www.cept.org/ecc/topics/spectrum-for-wireless-broadband-5g`

[5] A. De, T. K. Sarkar, and M. Salazar-Palma, "Antenna effects in a wireless communication scenario," *European Conference on Antennas and Propagation (EuCAP)*, Rome, Italy, April 2011.

[6] World Health organisation, 'Exposure limits for radio-frequency fields (public) Data by country', 2017. [Online]. Available: `apps.who.int`.

[7] World Health organisation, 'Exposure limits for radio-frequency fields (public) Data by country', 2017. [Online]. Available: `http://apps.who.int/gho/data`.

[8] Bruxelles environnement, 'Comparer les normes', May 2018, [Online]. Available: `https://environnement.brussels/thematiques/ondes-et-antennes/quelles-sont-les-normes/comparer-les-normes`.

[9] G.Hennaux, *Auxiliary Radiators for Human Exposure Reduction in Cellular Networks*, Université Catholique de Louvain, 2015.

[10] H. Husnain, "Parasitic Antenna Array for 4G and 5G Communication Base Stations to Implement Beamforming," to be submitted.

[11] C. Oestges, and B. Clerckx, *MIMO wireless communications: from real-world propagation to space-time code design*, Academic Press, 2010.

[12] Centre d'Informatique de la Région Bruxelloise, Available: `https://cirb.brussels/fr/nos-solutions/urbis-solutions/urbis-data`

[13] J. B. Keller, " Geometrical Theory of Diffraction," *Journal of Optical Society of America*, vol. 52, no. 2, pp. 116-130, 1962.

[14] R.G. Kouyoumjian and P.H. Pathak, " A Uniform Geometrical Theory of Diffraction for an Edge in a Perfectly Conducting Surface," *Proc. IEEE*, vol. 62, pp. 1448-1462, 1974.

[15] D. McNamara, C. Pistorius, and J. Malherbe, *Introduction to the Uniform Geometrical Theory of Diffraction*, Artech House, 1990.

[16] V. DegliEsposti, D. Guiducci, A. de Marsi, P. Azzi, and F. Fuschini, " An Advanced Field Prediction Model Including Diffuse Scattering," *IEEE Trans. Antennas Propag.*, vol. 52, no. 7, July 2004.

[17] I. Kavanagh, V. Pham-Xuan, M. Condon, and C. Brennan, " A method of moments based indoor propagation model, " *European Conference on Antennas and Propagation (EuCAP)*, Lisbon, Portugal, Aug. 2015.

[18] D. Trinh, V. Pham, S. Hussain, and C. Brennan, " Integral equation based path loss modelling for propagation in urban environments," *International Conference on Electromagnetics in Advanced Applications (ICEAA)*, Palm Beach, Netherlands Antilles, Aug. 2014.

[19] Y. Wang, S. Safavi-Naeini, and S. K. Chaudhrui, " A Hybrid Technique Based on Combining Ray Tracing and FDTD Methods for Site-Specific Modelling of Indoor Radio Wave Propagation, " *IEEE Trans. Antennas Propag.*, vol. 48, no. 5, pp. 743-754, May 2000.

[20] E.G. Papkelis, I. Psarros, I.C. Ouranos, C.G. Moschovitis, K.T. Karakatselos, E. Vagenas, H.T. Anastassiu, and P.V. Frangos, "A radio-coverage prediction model in wireless communication systems based on physical optics and the physical theory of diffraction," *IEEE Trans. Antennas Propag. Mag.*, vol. 49, no. 2, pp. 156-165, April 2007.

[21] E. Martini, C. Craeye, N. Ozdemir, and S. Maci, "Harmonics-based inhomogeneous plane-wave method (HIPWA)," *IEEE Trans. Antennas Propag.*, vol. 63, no. 5, pp. 2331-2336, May 2015.

[22] O. M. Bucci, and G. Franceschetti, "On the Degrees of Freedom of Scattered Fields," *IEEE Trans. Antennas Propag.*, vol. 37, no. 7, pp. 918-926, July 1989.

[23] F. Andersson, "Algorithms for Unequally Spaced Fast Laplace Transforms," *Applied Computational Harmonic Analysis*, vol. 35, pp. 419-432, 2013.

[24] P. L. Garcia-Muller and A. G. Roederer, "A Physical Optics Based Plane Wave Spectrum Approach to the Analysis of Finite Planar Antennas," *IEEE Trans. Antennas Propag.*, vol. 40, no. 8, pp. 906-911, Aug. 1992.

[25] W. B. Gordon, "Far-field approximations to the Kirchhoff-Helmholtz representations of scattered fields," *IEEE Trans. Antennas Propag.*, vol. 22, no. 4, pp. 590-592, July 1975.

[26] S. W. Lee, and R. Mittra, "Fourier transform of a polygonal shape function and its application to electromagnetism," *IEEE Trans. Antennas Propag.*, vol. 31, no. 1, pp. 99-103, Jan. 1983.

[27] B. Hu, W. C. Chew, and S. Velamparambil, "Fast inhomogeneous plane wave algorithm for the analysis of electromagnetic scattering," *Radio Sci.*, vol. 36, no. 6, pp. 1327-1340, 2001.

[28] L. J. Jiang and W. C. Chew, "Low-frequency fast inhomogeneous plane wave algorithm (LFFIPWA)," *Microw. Opt. Technol. Lett.*, vol. 40, no. 2, pp. 117-122, Jan. 2004.

[29] K. Alkhalifeh, G. Hislop, N. A. Nilufer, and C. Craeye, "Efficient MoM Simulation of 3D Antennas in the vicinity of the Ground," *IEEE Trans. Antennas Propag.*, vol. 64, no. 12, pp. 5335-5344, Dec. 2016.

[30] B. Hu, and W. C. Chew, "Fast IPW Algorithm for Scattering from Objects Above the Multilayered Medium," *IEEE Trans. Geosci. Remote Sens.*, vol. 39, no. 5, pp. 1028-1038, May 2001.

[31] M. Di Vico, F. Frezza, L. Pajewski, and G. Schettini, "Scattering by buried dielectric cylindrical structures," *Radio Sci.*, vol. 40, Aug. 2005, RS6S18.

[32] Q. Gueuning, C. Craeye, and C. Oestges, "Inhomogeneous plane wave spectrum based Physical Optics," *International Conference on Electromagnetics in Advanced Applications (ICEAA)*, 2015, Turin, Italy, 2015, pp. 1460-1463.

[33] R. Coifman, V. Rokhlin, and S. Wandzura, "The fast multipole method for the wave equation: A pedestrian prescription," *IEEE Antennas Propag. Mag.*, vol. 35, no.3, pp. 7-12, June 1993.

[34] J. E. Hansen, *Spherical Near-Field Antenna Measurements*, London, UK: Peter Peregrinus Ltd., 1988.

[35] D. Slepian, "Prolate spheroidal wave functions, Fourier analysis and uncertainty IV: extensions to many dimensions, generalized prolate spheroidal functions," *Bell Syst. Techn.*, vol. 43, no. 6, pp. 3009-3057, Nov. 1964.

[36] O. M. Bucci, and G. Franceschetti, "Optimal interpolation of radiated fields over a sphere," *IEEE Trans. Antennas Propag.*, vol. 39, no. 11, pp. 1633-1643, Nov. 1991.

[37] K. Tap, "Complex source point beam expansions for some electromagnetic radiation and scattering problems," Ph.D. dissertation, Dept. Elect. Comput. Eng., The Ohio State Univesity, Colombus, USA, 2007.

[38] J. M. Arnold, "Phase-space localization and discrete representation of wave fields," *J. Opt. Soc. Am. A*, vol. 12, no. 1, pp. 111-123, Jan. 1995.

[39] E. Michielssen, and W. C. Chew, "Fast steepest descent path algorithm for analyzing scattering from two-dimensional objects," *Radio Sci.*, vol. 31, no. 5, pp. 2326-1224, 1996.

[40] O. M. Bucci, and G. Franceschetti, "On the spatial bandwidth of scattered fields," *IEEE Trans. Antennas Propag.*, vol. 35, no. 12, pp. 1445-1455, Dec. 1987.

[41] J. A. Kong, Ed., *Theory of Electromagnetic Waves*, Hoboken, NJ, USA: Wiley, 1975.

[42] S. Ohnuki, and W. C. Chew, "Error analysis of the fast IPW algorithm for 2D free-space cases," *Microw. Opt. Technol. Lett.*, vol. 38, no. 4, pp. 300-304, Aug. 2003.

[43] D. M. Pozar, "Input impedance and mutual coupling of rectangular microstrip antennas," IEEE Trans. Antennas Propag., vol. 30, no. 6, pp. 1191-1196, Nov. 1982.

[44] K. Michalski and J. Mosig, "Multilayered media Green's functions in integral equation formulations," *IEEE Trans. Antennas Propag.*, vol. 45, no. 3, pp. 508-519, Mar. 1997.

[45] R. Borghi, F. Frezza, M. Santarsiero, C. Santini, and G. Schettini, "Numerical study of the reflection of cylindrical waves of arbitrary order by a generic planar interface," *J. Electromagn. Waves Appl.*, vol. 13, pp. 27-50, Jan. 1999.

[46] S. Lambot, E. Slob, and H. Vereecken, "Fast evaluation of zero-offset Green's fucntion for layered media with application to ground-penetrating radar," *Geophysical Research Letters*, vol. 34, 2007.

[47] S. N. Jha and C. Craeye, "Contour-FFT based spectral domain MBF analysis of large printed antenna arrays," *IEEE Trans. Antennas Propag.*, vol. 62, no. 11, pp. 5752-5764, Nov. 2014.

[48] H. Ostner, J. Detlefsen, and D. R. Jackson, "Radiation from One-dimensional Dielectric Leaky-Wave Antennas," *IEEE Trans. Propag. Antennas*, vol. 43, no. 4, pp.331-339, April 1995.

[49] R. B. Boix, F. Mesa, and F. Medina, "Application of Total Least Squares to the Derivation of Closed-Form Green's Functions for Planar Layered Media," *IEEE Trans. Microw. Theory Techn.*, vol.55, no.2, Feb. 2007.

[50] E. Martini, S. Karki, C. Craeye and, S. Maci, "Error analysis of the harmonics-based plane wave method," International Conference on Electromagnetics in Advanced Applications (ICEAA), Turin, 2015, Italy, 2015, pp. 1493-1495.

[51] W. C. Chew, *Waves and Fields in Inhomogeneous Media*, New York, USA: Van Nostrand Reinhold, 1990.

[52] C. Craeye,"A series representation for the intermediate-field transmittance between apertures," *International Symposium on Electromagnetic Theory*, Espoo, Finland, 2016, pp. 240-242.

[53] W. C. Chew, E. Michielssen, J. M. Song, and J. M. Jin, Eds., *Fast and Efficient Algorithms in Computational Electromagnetics*, Norwood, MA, USA: Artech House, Inc., 2001.

[54] J. A. Stratton, *Electromagnetic Theory*, New York, USA: McGraw-Hill Book Company, Inc., 1941.

[55] wikipedia.org, "Gauss circle problem," [Online]. Available: https://en.wikipedia.org/wiki/Gauss_circle_problem.

[56] S. Jiang-Sheng, G. Ben-Qing, "Critical distance of far field for basic radiation element," *International Symposium on Electromagnetic Compatibility*, Qingdao, China, 2007, pp. 375-377.

[57] Rosenheinrich W., *Tables of some indefinite integrals of bessel functions*, University of Applied Sciences Jena, Germany, http://www.eah-jena.de/rsh/Forschung/Stoer/besint.pdf, pp. 124

[58] Q. Gueuning, S. Hubert, C. Oestges, and C. Craeye, "Error model for Contour-FFT evaluation of the free-space on-plane Green's function," *Int. Symp. on Electromagn. Theory*, Espoo, Finland, 2016.

[59] S. Hubert, S. N. Jha, and C. Craeye, "Error analysis for the Contour-FFT based Green's function," *Electromagn. in Adv. Appl. (ICEAA), 2015, Int. Conf.*, Torino, Sept. 2015.

[60] wikipedia.org, "Lambert W function," [Online]. `https://en.wikipedia.org/wiki/Lambert_W_function`.

[61] S. Hubert, S. N. Jha, and C. Craeye, "Analysis of Large Non-regular Printed Scatterers Using the Contour-FFT," *IEEE Trans. Propag. Antennas*, Aug. 2018.

[62] R. Mittra, Y. Rahmat-Samii, and W. L. Ko, "Spectral theory of diffraction,"*Appl. Phys.*, vol. 10, 1976.

[63] K.C. Hill, *A UTD solution to the em scattering by the vertex of a perfectly conducting plane angular sector*, The Ohio State Univ., 1990.

[64] J.G. Meana, J.A. Martinze-Lorenzo, F. Las-Heras, and C. Rappaport, "Wave Scattering by Dielectric and Lossy Materials Using the Modified Equivalent Current Approximation (MECA)," *IEEE Trans. Antennas Propag.*, vol. 58, no. 11, pp. 3757-3761, Nov. 2010.

[65] C.A. Balanis, *Advanced Engineering Electromagnetics*. New York: Wiley, 1989.

[66] M. V. Vesnik, P. Y. Ufimtsev, "An asymptotic feature of corner waves scattered by polygonal plates," *Electromagnet.*, vol. 12, no. 3-4, pp. 265-272, 1992.

[67] wikipedia.org, "Heaviside step function," [Online]. `https://en.wikipedia.org/wiki/Heaviside_step_function`

[68] P. C. Clemmow and T. B. A. Senior, " A note on the generalized Fresnel integral," in *Proc. Cambridge Phil. Soc.*, vol. 49, 1953.

[69] F. Capolino and S. Maci, "Simplified closed-form expressions for computing the generalized Fresnel integral and their application to vertex diffraction," *Microw. Opt. Technol. Lett.*, vol. 9, no. 1, May 1995.

[70] wikipedia.org, "Point in polygon," [Online]. `https://en.wikipedia.org/wiki/Point_in_polygon`

[71] A. Ciarkowski and R. Mittra, "Plane-wave diffraction by a wedge - a spectral domain approach," *University of Illinois at Urbana-Champaign*, Nov. 1981.

[72] P.Y. Ufimtsev, *Fundamentals of the Physical Theory of Diffraction*, Hoboken, New Jersey, USA: John Wiley and Sons, Inc., 2007.

[73] K.C. Hill, *A UTD solution to the em scattering by the vertex of a perfectly conducting plane angular sector*, The Ohio State Univ., 1990.

[74] J.B. Keller, " Diffraction by a Convex Cylinder," *IRE Trans. Antennas Propag.*, vol. 4, no. 3, July 1956.

[75] P.H. Pathak, G. Carluccio, and M. Albani, " The Uniform Geometrical Theory of Diffraction and Some of Its Applications," *IEEE Antennas Propag. Mag.*, vol. 55, no. 4, Aug. 2013.

[76] M. Albani, F. Capolino, G. Carluccio, and S. Maci, " UTD Vertex Diffraction Coefficient for the Scattering by Perfectly Conducting Faceted Structures," *IEEE Trans. Antennas Propag.*, vol. 57, no. 12, Dec. 2009.

[77] F.A. Sikta, W.D. Burnside, T.T. Chu, and L. Peters, Jr., " First-order equivalent current and corner diffraction from flat plate structures," *IEEE Trans. Antennas Propag.*, vol. 31, no. 4, pp. 584-589, Jul. 1983.

[78] J.L. Volakis, "Diffraction by Impedance Structures and Higher Order Boundary Conditions: A Review," *IEEE-APS Topical Conf. on Antennas and Propag. in Wireless Communications (APWC)*, Cape Town, South Africa, Sept. 2012.

[79] A. Michaeli, "Equivalent Edge Currents for Arbitrary Aspects of Observation," *IEEE TAP*, vol. 32, no. 3, pp. 252-258, March 1984.

[80] K. M. Mitzner, "Incremental Length Diffraction Coefficients," 1974.

[81] A. Sommerfeld, *Mathematische Theorie der Diffraction*, Mathematische Annalen, Volume 16, 1896.

[82] J. Van Bladel, *Singular Electromagnetic Fields and Sources*, New York, USA: Oxford University Press, 1991, pp. 117-125.

[83] H.L. Bertoni, A.C. Green, and L.B. Felsen, "Shadowing an inhomogeneous plane wave by an edge," *J. Opt. Soc. Am.*, vol. 68, no. 7, pp. 983-988, July 1978.

[84] R.G. Kouyoumjian, T. Celandroni, G. Manara, and P. Nepa, "Inhomogeneous electromagnetic plane wave diffraction by a perfectly electric conducting wedge at oblique incidence," *Radio Sci.*, vol. 42, RS6S06, 2007.

[85] C. Gennarelli and L. Palumbo, "A uniform asymptotic expansion of a Typical Diffraction Integral with many Coalescing Simple Pole Singularities and a First-Order Saddle Point," *IEEE Trans. Antennas Propag.*, vol. 32, no. 10, pp. 1122-1124, Oct. 1984.

[86] Feko, `www.Feko.info`.

[87] IE3D, Mentor Graphics, `http://www.mentor.com`.

[88] K. Kim, S. Oh, "Geometric Optics-Based Propagation Prediction Model in Urban Street Canyon Environments," *IEEE Antennas Wireless Propag. Lett.*, vol. 15, pp. 1128-1131, Oct. 2016.

[89] W. Zhang, J. Lahteenmaki, P. Vainikainen, "A practical aspect of over-rooftop multiple-building forward diffraction from a low source," *IEEE Trans. Electromagn. Compat.*, vol. 41, pp. 115-119, May 1999.

[90] G. Carluccio, and M. Albani, "An Efficient Ray Tracing Algorithm for Multiple Straight Wedge Diffraction," *IEEE Trans. Antennas Propag.*, vol. 56, no. 11, pp. 3534-3542, Nov. 2008.

[91] E. Di Giampaolo and F. Bardati, "A projective approach to electromagnetic propagation in complex environments," *Progress In Electromagnetics Research B*, vol. 13, pp. 357-383, 2009.

[92] J.G. Meana, J.A. Martinez-Lorenzo, F. Las-Heras, and C. Rappaport, "DIRECT : a deterministic radio coverage tool," *IEEE Antennas Propag. Mag.*, vol. 53, no. 2, April 2011.

[93] G. Kubicke, C. Bourlier, M. Delahaye, C. Corbel, N. Pinel, and P. Pouliguen, "Bridging the gap between the Babinet principle and the Physical Optics approximation: Vectorial Problem," Radio Sci., vol. 48, no. 5, pp. 573-581, 2013.

[94] H. Fuchs, G. Abram, and E. Grant, "Near Real-Time Shaded Display of Rigid Objects," *Computer Graphics*, vol. 17, no. 3, pp. 65-69, July 1983.

[95] B. Naylor, "Binary Space Partitioning Trees - A Tutorial," *Conf. Proc. of SIGGRAPH 94*, Sept. 1994.

[96] B. Naylor, "Constructing Good Partitioning Trees," *Graphics Interface 93*, Canada, Toronto, pp. 181-191, May 1993.

[97] Thibault, W. C. and B. F. Naylor, "Set of operations on polyhedra using BSP trees," *Conf. Computer Graphics and Interactive Techniques, SIGGRAPH 87*, vol. 21, pp. 153-162, August 1987.

[98] I. J. W. Cooley and J. W. Tukey, "An algorithm for the Machine Calculation of Complex Fourier Series," *Mathematics of Computation*, vol. 19, no. 90, pp. 297-301, April 1965.

[99] K. Yang and A. E. Yilmaz, "FFT-Accelerated Analysis of Scattering From Complex Dielectrics Embedded in Uniaxial Layered Media," *IEEE Geoscience and Remote Sensing Letters*, vol. 10, no. 4, pp. 662-666, July 2013.

[100] M. Leutenegger, R. Rao, R. A. Leitgeb, and T. Lasser, "Fast focus field calculations," *Opt. Express*, vol. 14, no. 23, pp. 11277-11291, Nov. 2006.

[101] W. C. Chew, G. L. Wang, A. A. Aydiner, T. J. Cui, "Recent advances in nonlinear inverse scattering," *Int. Symp. Electrom. Theory (URSI 2004)*, pp. 697-699, May 2004.

[102] T. G. Stockham, "High-speed convolution and correlation," *1966 Spring Joint Computer Conf., AFIPS Proc.,*, vol. 28, Washington, D.C., Spartan, 1 966, pp. 229-233.

[103] E. Bleszynski, M. Bleszynski, and T. Jaroszewicz, "AIM: Adaptive integral method for solving large-scale electromagnetic scattering and radiation problems, " *Radio Sci.*, vol. 31, no. 5, pp. 1225-1251, Sept.-Oct. 1996.

[104] X. C. Nie, J. L. W. Li, and N. Yuan, "Precorrected-FFT algorithm for solving combined field integral equations in electromagnetic scattering," *Journal of Electromagnetic Waves and Applications*, vol. 16, no. 8, pp. 574-577, 2002.

[105] W. C. Chew, J. M. Jin, and E. Michielssen, *Fast and efficient algorithms in computational electromagnetics*, Artech House, Norwood, MA, USA, 2001.

[106] Y. L. Li, C. H. Liu, and S. J. Francke, "Adaptive Evaluation of the Sommerfeld-Type Integral Using the Chirp z-Transform," *IEEE Trans. Antennas Propag.*, vol. 39, pp. 1788-1791, Dec. 1991.

[107] Q. Gueuning, C. Craeye, and C. Oestges, "Unequally-spaced fast Laplace transform for Green's function evaluation," *Int. Symp. on Electromagn. Theory*, Espoo, Finland, 2016.

[108] wikipedia.org, "Taylor's theorem," [Online]. `https://en.wikipedia.org/wiki/Taylor's_theorem`

[109] L. R. Rabiner, R. W. Schafer, C. M. Rader, "The Chirp z-Transform," *IEEE Trans. Audio and Electroacoustics*, vol. 17, no. 2, pp. 86-92, June 1969.

[110] C. Craeye, N. Ozdemir, E. Martini, and S. Maci, "Complex patterns devoted to physical compression of MoM matrices," *2013 7th European Conference on Antennas and Propagation (EuCAP)*, Gothenburg, Sweden, 2013.

[111] Fastest Fourier Transform in the West (FFTW), `http://www.fftw.org`.

[112] MATLAB 2014a, The MathWorks, Natick, 2014.

[113] M. Ando, "Physical optics," in *Analysis Methods for Electromagnetic Wave Problems*, vol. 2, E. Yamashita, Eds. Norwood, MA, USA:Artech House, 1996, ch.4.

[114] Y. Miao, Q. Gueuning, and C. Oestges, "Modeling the Phase Correlation of Effective Diffuse Scattering From Surfaces for Radio Propagation Prediction with Antennas at Refined Separation," IEEE Trans. Antennas Propag., vol. 66, no. 3, March 2018.

[115] A. Ishimaru, *Wave Propagation and Scattering in Random Media*, Academic Press, USA, 1978.

[116] A. K. Fung, *Microwave scattering and emission models and their applications*, Boston, USA : Artech House, inc, 1994.

[117] J. Wright, " A new model for sea clutter, " *IEEE Trans. Antennas Propag.*, vol. 2, no. 2, pp. 217-223, March 1968.

[118] A. Dutt and V. Rokhlin, "Fast Fourier transforms for nonequispaced data," *SIAM J. Sci. Comput.*, vol. 14, no. 6, pp. 1368-1393, 1993.

[119] wikipedia.org, "Fast Fourier Transform," [Online]. `https://en.wikipedia.org/wiki/Fast_Fourier_Transform`

[120] C. Craeye, "On the Transmittance Between OAM Antenna," *IEEE Trans. Antennas Propag.*, vol. 64, no. 1, Jan. 2016.

[121] wikipedia.org, "Dipole antenna," [Online]. `https://en.wikipedia.org/wiki/Dipole_antenna#Hertzian_dipole`

[122] O. Ergul, and L. Gurel, "Optimal Interpolation of Translation Operator in Multilevel Fast Multipole Algorithm," *IEEE Trans. Antennas Propag.*, vol. 54, no. 12, pp. 3822-3826, Dec. 2006.